

RADIATIVE-CONVECTIVE MODEL FOR ONE-DIMENSIONAL LONGWAVE
CLEAR SKY ATMOSPHERE

A THESIS SUBMITTED TO
THE GRADUATE SCHOOL OF NATURAL AND APPLIED SCIENCES
OF
MIDDLE EAST TECHNICAL UNIVERSITY

BY

GÜZİDE AYDIN

IN PARTIAL FULFILLMENT OF THE REQUIREMENTS
FOR
THE DEGREE OF MASTER OF SCIENCE
IN
CHEMICAL ENGINEERING

SEPTEMBER 2008

Approval of the thesis:

**RADIATIVE-CONVECTIVE MODEL FOR ONE-DIMENSIONAL CLEAR
SKY ATMOSPHERE**

submitted by **GÜZİDE AYDIN** in partial fulfillment of the requirements for the degree of **Master of Science in Chemical Engineering Department, Middle East Technical University** by,

Prof. Dr. Canan Özgen
Dean, **Graduate School of Natural and Applied Sciences** _____

Prof. Dr. Gürkan Karakaş
Head of Department, **Chemical Engineering** _____

Prof. Dr. Nevin Selçuk
Supervisor, **Chemical Engineering Dept., METU** _____

Assist. Prof. Dr. Görkem Külah
Co-Supervisor, **Chemical Engineering Dept., METU** _____

Examining Committee Members:

Prof. Faruk Arıncı
Mechanical Engineering Dept., METU _____

Prof. Dr. Nevin Selçuk
Chemical Engineering Dept., METU _____

Assist. Prof. Dr. Görkem Külah
Chemical Engineering Dept., METU _____

Assist. Prof. Dr. Nimeti Döner
Mechanical Engineering Dept., DPU _____

Dr. Ahmet Bilge Uygur
Turkish Aerospace Industries, Inc. _____

Date: 05.09.2008

I hereby declare that all information in this document has been obtained and presented in accordance with academic rules and ethical conduct. I also declare that, as required by these rules and conduct, I have fully cited and referenced all material and results that are not original to this work.

Name, Last name : Güzide Aydın

Signature :

ABSTRACT

RADIATIVE-CONVECTIVE MODEL FOR ONE-DIMENSIONAL LONGWAVE CLEAR SKY ATMOSPHERE

Aydın, Güzide

M.Sc., Department of Chemical Engineering

Supervisor: Prof. Dr. Nevin Selçuk

Co-Supervisor : Assist. Prof. Dr. Görkem Külâh

September 2008, 144 pages

Climate models are the primary tools used for understanding past climate variations and for future projections. The atmospheric radiation is the key component of these models. Accurate modeling of atmosphere necessitates reliable evaluation of the medium radiative properties and accurate solution of the radiative transfer equation in conjunction with the time-dependent multi-dimensional governing equations of atmospheric models. Due to difficulty in solving the equations of atmospheric and radiation models simultaneously, radiation equations have been solved when input data such as concentration, temperature etc. were made available upon solution of equations of atmospheric models. Generally, time step of conservation equations are 10-30 minutes but radiative transfer equation is called only once every 1-3 hours. However, there is inaccuracy due to the fixed radiation fluxes over the intervening time steps. To overcome this problem, the equations of atmospheric and radiation models have to be solved simultaneously and the solution methods have to be compatible. For this purpose, a radiative-convective model with

radiation model based on method of lines (MOL) solution of discrete ordinate method (DOM) with wide band correlated-k (WBCK) was developed. To achieve this objective, a previously developed MOL solution of DOM with WBCK model was adapted to 1-D longwave clear sky atmosphere and its predictive accuracy and computational efficiency was examined on the test problem by using benchmark solution obtained from Line-by-line Radiative Transfer Model (LBLRTM). The radiation code was then coupled with radiative-convective model and the predictive accuracy of this model was examined for several coupling intervals. Comparisons reveal that as coupling interval increases, although the computation time of the model decreases, the predicted temperature profiles diverge from the one obtained when equations of radiative-convective model and the radiation model are solved simultaneously and percentage relative error in temperature increases an order of magnitude when coupling time between radiative-convective model and the radiation model increases from 2 to 10 hours. Therefore, it can be concluded that the equations of the radiation model have to be solved simultaneously with the equations of the climate model.

Overall evaluation of the performance of the radiation model used in this study points out that it provides accurate and computationally efficient solutions and can be used with confidence in conjunction with the climate models for simultaneous solution of governing equations with radiation transfer equation.

Keywords: Radiative-Convective Model, Atmospheric Radiation, Method of Lines, Discrete Ordinates Method, Nongray Media, Wide Band Correlated- k (WBCK) Model.

ÖZ

BİR BOYUTLU, UZUN DALGA, BULUTSUZ HAVA KOŞULU İÇİN IŞINIM-TAŞINIM MODELİ

Aydın, Güzide

Yüksek Lisans, Kimya Mühendisliği Bölümü

Tez Yöneticisi: Prof. Dr. Nevin Selçuk

Ortak Tez Yöneticisi: Yrd. Doç. Dr. Görkem Külah

Eylül 2008, 144 Sayfa

İklim modelleri, geçmiş iklim değişikliklerini ve geleceğe ait tahminlerde kullanılan birincil araçlardır. Atmosferik ışıınım bu modellerin ana ögesidir. Atmosferin doğru modellenmesi ortamın ışıınım özelliklerinin güvenilir değerlendirilmesini ve atmosferik modellerin zamana bağlı çok boyutlu problemi tanımlayan denklemlerle birlikte ışıınım ısı transfer denkleminin doğru çözülmesini gerektirmektedir. Atmosfer ve ışıınım modellerinin denklemlerinin eş zamanlı çözülmesindeki güçlük nedeniyle, ışıınım denklemi, atmosferik model denklemlerinin çözümleri konsantrasyon, sıcaklık gibi girdileri sağladığı zaman çözülür. Genellikle, korunum denklemlerinin zaman aralığı 10-30 dakikadır ancak ışıınım ısı transfer denklemini sadece 1-3 saatte bir çözülür. Lakin, ara dönemdeki zamanda ışıınım akılarının sabit tutulmasından dolayı hata olmaktadır. Bu problemin üstesinden gelinmesi için, atmosfer ve ışıınım model denklemlerinin eş zamanlı çözülmesi gerekmektedir. Bu amaçla, geniş bantlı bağdaşık-k ile belirli yönler yönteminin

izgiler metoduyla özümüne dayalı ışınm modeli ile ışınm-taşınm modeli geliştirilmiştir. Bunu sağlamak için, önceden geliştirilmiş olan geniş bantlı bağdaşık- k ile belirli yönler yönteminin çizgiler metoduyla çözüm modeli bir boyutlu, uzun dalga, bulutsuz hava koşuluna uyarlanmıştır ve modelin öngörme doğruluğu ve bilgisayar zamanı açısından verimi LBLRTM'in çözümleriyle karşılaştırılarak test problemi üzerinde değerlendirilmiştir. Daha sonra ışınm kodu ışınm-taşınm modeliyle birleştirilmiştir ve bu modelin öngörme doğruluğu çeşitli birleşme aralıkları için incelenmiştir. Karşılaştırmalar, birleştirme aralığı arttığı zaman, modelin hesaplama zamanı azalmasına rağmen, öngörülen sıcaklık profili ışınm-taşınm modelinin ve ışınm modelinin denklemlerinin eş zamanlı çözülmesinden elde edilenden saptığını; ve ışınm-taşınm modeli ile ışınm modelinin arasındaki birleştirme aralığı 2 saatten 10 saate çıkarıldığı zaman, sıcaklıktaki yüzde hataların bir büyüklük kertesine kadar arttığını göstermiştir. Bu nedenle, ışınm modelinin denklemleri iklim modellerinin denklemleriyle eş zamanlı çözülmesi gerektiği sonucuna varılabilir.

Bu çalışmada kullanılan ışınm kodunun değerlendirmesi sonucu bu kodun doğru ve bilgisayar zamanı açısından verimli çözümler sağladığı ve ışınm ısı transfer denklemiyle problemi tanımlayan denklemlerin eş zamanlı çözümü için iklim modelleriyle birlikte güvenle kullanılabilceği görülmüştür.

Anahtar kelimeler: Işınım-Taşınım Modeli, Atmosferik Işınım, Çizgiler Metodu, Belirli Yönler Yöntemi, Gri Olmayan Ortam, Geniş Bantlı Bağdaşık- k modeli.

To My Family and Aykut

ACKNOWLEDGEMENTS

I wish to express my deepest gratitude to my supervisor, Prof. Dr. Nevin Selçuk for her guidance and encouragement throughout this study.

I would like to show my appreciation to my co-supervisor, Assist. Prof. Dr. Görkem Külâh, for her precious discussions and comments during the progress of this thesis.

I would like to thank Nihan Çayan whose thesis and computer programmes provided basis for this study.

I thank to the research team members for their friendship and support during my study; Ahmet Bilge Uygur, Işıl Ayrancı, Zeynep Serinyel, Mehmet Moralı and İlker Soner.

I would like to thank Canan Gücüyener, Tuğçe İrfan Ersöz and Saltuk Pirgaloğlu for their encouragement and motivation during this study.

Special thanks go to my family, İsa, Fatma, Murat and Azize Aydın, for their great support, encouragement and unshakable faith in me.

Turkish Scientific and Technical Research Council (TÜBİTAK) is gratefully acknowledged for supporting this study by National Scholarship Programme for MSc Students (2210).

TABLE OF CONTENTS

ABSTRACT.....	iv
ÖZ.....	vi
ACKNOWLEDGEMENTS.....	ix
TABLE OF CONTENTS.....	x
LIST OF TABLES.....	xiii
LIST OF FIGURES.....	xvi
LIST OF SYMBOLS.....	xx
CHAPTERS	
1. INTRODUCTION	1
2. BACKGROUND	9
2.1 Earth's Atmosphere.....	9
2.1.1 The Early Atmosphere	9
2.1.2 The Atmosphere Today.....	11
2.1.3 Measurement Techniques of the Atmospheric Profile.....	12
2.1.4 Vertical Structure of the Atmosphere	16
2.1.4.1 Troposphere	17
2.1.4.2 Stratosphere.....	17
2.1.4.3 Mesosphere	17
2.1.4.4 Thermosphere	18
2.1.4.5 Exosphere.....	18
2.2 Climate	20
2.2.1 Climate System	20
2.2.2 Energy Budget of the Earth.....	22

2.2.3 Climate Forcings	24
2.2.3.1 External Forcings	24
2.2.3.2 Internal Forcings	25
2.2.3.2.1 Human-induced Changes	25
2.2.3.2.2 Natural Changes	26
2.2.4 Climate Feedbacks	29
2.2.5 Climate Records	30
2.2.5.1 Techniques for Reconstructing Past Climates	30
2.2.5.1.1 Longer-term Climate Change: Ice Age	32
2.2.5.1.2 Historical Climate Change	35
2.2.5.1.3 Contemporary Trends in Assessment of Global Temperature ...	37
2.2.5.1.3.1 Problems of the Calculation of Global Surface Temperature	38
2.2.5.1.3.2 The Reasons of the Global Surface Temperature Change	44
2.3 Climate Models	55
3. RADIATIVE-CONVECTIVE MODEL, RADIATION MODEL AND THEIR NUMERICAL SOLUTION TECHNIQUE	57
3.1 Radiative-Convective Model	57
3.2 Radiation Model	63
3.2.1 Radiative Transfer Equation (RTE)	63
3.2.2 Discrete Ordinates Method (DOM)	66
3.2.3 The Method of Lines (MOL) Solution of DOM	70
3.3 Numerical Solution Technique	71
3.3.1 The Method of Lines	71
3.3.2 Coupling Procedure for Radiative-Convective Model	73
3.3.2.1 Algorithm of Coupled Code	75
4. ESTIMATION OF RADIATIVE PROPERTIES	81
4.1 Gas Radiative Property Models	81
4.2 Wide Band Correlated-k (WBCK) Model	82
5. RESULTS AND DISCUSSION	87
5.1 LBLRTM	87

5.1.1 Effect of Carbon Dioxide, Water Vapor and Temperature Changes on the Fluxes in the Atmosphere and the Earth's Surface	88
5.2 MOL Solution of DOM with WBCK.....	93
5.2.1 Description of the Physical System	93
5.2.2 Effect of Spatial Discretization	96
5.2.3 Effect of Order of Approximation	104
5.2.4 Effect of Number of Gray Gases.....	105
5.3 Radiative-Convective Model	106
6. CONCLUSIONS.....	111
6.1 Suggestions for Future Work	112
REFERENCES	114
APPENDICES	
A. EXPONENTIAL WIDE BAND MODEL PARAMETERS.....	125
A.1 Calculation of Band Strength Parameter	125
A.2 Calculation of Line Overlap Parameter.....	127
A.3 Calculation of Band Width Parameter	127
B. INITIAL PARAMETERS FOR THE ODE SOLVER (ROWMAP) SUBROUTINE.....	129
C. POINT VALUES OF ALL PREDICTED QUANTITIES BY MOL OF SOLUTION DOM AND LBLRTM	131
D. GRID GENERATION	138
E. POINT VALUES OF PREDICTED TEMPERATURE PROFILE	141

LIST OF TABLES

TABLES

Table 2.1 Compositions of the earth's atmosphere.....	11
Table 2.2 Global carbon budget.....	54
Table 3.1 Total number of discrete directions specified by order of approximation	68
Table 3.2 Direction cosines and weights for one-dimensional systems	69
Table 3.3 Spatial differencing schemes	73
Table 4.1 Poles, p_i , and coefficients, $c_{i,j}$	84
Table 5.1 Comparison between the predicted net fluxes by the code and the findings of Clough and Iacono [7]	89
Table 5.2 Changes in the net fluxes (W/m^2) in the atmosphere and the earth's surface in midlatitude summer atmosphere due to doubling the CO_2	90
Table 5.3 Changes in net fluxes (W/m^2) in five different scenarios	92
Table 5.4 Maximum and average percentage relative errors in the net flux predictions of the present study with cpu times for different uniform grids	97
Table 5.5 Summary of the spacing between grid points.....	98
Table 5.6 Maximum and average percentage relative errors in the down flux predictions of the present study with their cpu times for different non- uniform grids.....	100
Table 5.7 The spacing of non-uniform grids developed by grid generation.....	101
Table 5.8 Maximum and average percentage relative errors in the flux predictions of the present study with their cpu times for different grid size weights (Δz)	104
Table 5.9 Maximum and average percentage relative errors in the flux predictions of the present study with their cpu times for different order of approximation	105

Table 5.10 Maximum and average percentage relative errors in the flux predictions of the present study with their cpu times for several numbers of gray gases	106
Table 5.11 Average percentage relative errors in the temperature predictions of the present study for two different coupling intervals.....	109
Table 5.12 Computational times for different coupling interval	110
Table A.1 Exponential wide band model correlation parameters for H ₂ O and CO ₂	126
Table B.1 Final time values for different print intervals	130
Table B.2 Initial parameters utilized for rowmap subroutine for radiation and radiative-convective codes.....	130
Table C.1 Flux predictions (in W/m ²) of the present study and LBLRTM for different number of grids with uniform spacing	131
Table C.2 Absolute % relative errors of the present study for different number of grids with uniform spacing	133
Table C.3 Flux predictions (in W/m ²) of the present study and LBLRTM for different number of non-uniform grids	134
Table C.4 Absolute % relative errors of the present study for different number of non-uniform grids	135
Table C.5 Flux predictions of the present study and LBLRTM with absolute percentage error for az = 0.25	135
Table C.6 Flux predictions of the present study and LBLRTM with absolute percentage error for az = 0.4	136
Table C.7 Flux predictions of the present study and LBLRTM with absolute percentage error for az = 0.45	136
Table C.8 Flux predictions of the present study and LBLRTM m with absolute percentage error for az = 0.5	137
Table E.1 Temperature predictions during 40 hours period at the surface for different coupling interval and simultaneous solution.....	142
Table E.2 Temperature predictions during 40 hours period at 4 km above the surface for different coupling interval and simultaneous solution	143

Table E.3 Temperature predictions during 40 hours period at the top of the atmosphere for different coupling interval and simultaneous solution.. 144

LIST OF FIGURES

FIGURES

Figure 2.1 At the beginning of the 20 th century there were large gaps in the global network for regularly observing and reporting surface temperature, but by the end of the century these were mostly filled, except for the inhospitable polar regions.....	13
Figure 2.2 Monitoring the Earth's weather and building up the best possible picture of the climate involve a wide range of different observation systems, on land, at sea, in the air and from space	14
Figure 2.3 Layers of atmosphere.....	16
Figure 2.4 Atmospheric pressure variation with altitude.....	19
Figure 2.5 Average temperature profile of the atmosphere	20
Figure 2.6 Schematic diagram of major components of the climate system. Feedbacks between various components play an important role in climate variations.....	21
Figure 2.7 The Earth's energy budget adapted from [92].....	23
Figure 2.8 Schematic diagram showing the variations of the three orbital components: obliquity (axial tilt), orbital eccentricity and precession of the perihelion	25
Figure 2.9 An ENSO event showing three stages in ocean-atmosphere coupling: (a) standard condition; (b) warm phase El Niño; (c) cold phase La Niña.....	28
Figure 2.10 Global-mean monthly temperature for the period 1980-1999, showing the effects of El Niño (EN) and La Niña (LN). The upper graph shows the complete global-mean temperature record as context.....	29
Figure 2.11 Ice core records of (a) CO ₂ levels and (b) temperature from Antarctica (Vostok) over the last 400,000 years (i.e. four glacial-interglacial cycles)	33

Figure 2.12 Possible combined effect of the Milankovitch orbital cycles on ice age temperatures	34
Figure 2.13 Ten-year mean annual temperature departures (from 1880-1979 means) based on historical documents from East China (above) and North China (below).....	37
Figure 2.14 Annual anomalies ($^{\circ}\text{C}$) of global average SST (blue curve), NMAT (green curve) and land-surface air temperature (red curve), relative to their 1961 to 1990 means. The smooth curves show decadal variations. Inset shows the smoothed differences between the land-surface air temperature and SST anomalies.....	38
Figure 2.15 Global radiosonde balloon temperature (light line) and global satellite MSU temperature (dark line) with 6-month smoothing. Both sets of data are graphed as deviations from their respective means for 1979 to 1996	41
Figure 2.16 Observed surface and upper-air temperature anomalies ($^{\circ}\text{C}$). (A) Tropospheric T_2 (channel 2), (B) Lower tropospheric T_{2LT} , from UAH, RSS and VG2 MSU satellite analyses and UKMO HadAT2 and NOAA RATPAC radiosonde observations; and (C) Surface records from NOAA, NASA/GISS and UKMO/CRU (HadCRUT2v). All time series are monthly mean anomalies relative to the period 1979 to 1997 smoothed with a seven month running mean filter. Major volcanic eruptions are indicated by vertical blue dashed lines.....	42
Figure 2.17 Temperature change (with respect to present mean temperature) over the last six centuries by Mann et al. [106] (thin line) and as recalculated by McIntyre and McKittrick (thick line) [105]	43
Figure 2.18 Possible routes for a solar influence on climate	44
Figure 2.19 Time evolution over the 20th century of the eleven-year running averages of magnetic indices based on modulus of the geomagnetic field at the Eskdalemuir and Sitka observatories (ESK and SIT) compared to solar irradiance ($S(t)$) and global mean temperature (T_{globe}).	45
Figure 2.20 Variation of the sunspot cycle length (left-hand scale) determined as the	

	difference between the actual smoothed sunspot extremum and the previous one. The cycle length is plotted at the central time of the actual cycle (+). The unsmoothed last values of the time series have been indicated with different symbol (*) which represents the Northern Hemisphere temperature anomalies.	47
Figure 2.21	An update of the original solar curve in Figure 2.20 with points 1–4 calculated applying correct arithmetic to the observed and predicted data.	48
Figure 2.22	Composite figure showing four satellite cloud data sets and normalized cosmic rays fluxes from Climax (thick curve). Triangles are the Nimbus-7 data, squares are the ISCCP-C2 data, diamonds are the DMSP data, and crosses are the ISCCP-D2 data. The panel displays the data smoothed using a 12 months running mean, The Nimbus-7 and the DMSP data are total cloud cover for the Southern Hemisphere over oceans, and the ISCCP data have been derived from the geostationary satellites over oceans with the tropics excluded.	50
Figure 2.23	Squares denote ISCCP data and the blue solid curve shows galactic cosmic ray intensities as measured at Climax, Colorado, and smoothed as in Kristjánsson and Kristiansen [122]. The update consists in adding new ISCCP data as available from http://isccp.giss.nasa.gov/climanal1.html 2001	51
Figure 2.24	Annual changes in global mean CO ₂ concentration (grey bars) and their five-year means from two different measurement networks (red and lower black stepped lines).....	53
Figure 3.1	Schematic representation of the system under consideration.....	58
Figure 3.2	Vertical profiles of mixing ratio of selected species at equinox.....	60
Figure 3.3	Concentration of H ₂ O profiles for midlatitude summer atmosphere	60
Figure 3.4	Coordinate system for one-dimensional plane parallel system	64
Figure 3.5	Orders of approximation.....	67
Figure 3.6	Coupling procedure	74
Figure 3.7	Algorithm of the radiative-convective model.....	79
Figure 4.1	Discretization of representative re-ordered band.....	85

Figure 5.1 Water vapor concentration profile for midlatitude summer atmosphere..	94
Figure 5.2 Temperature profile for mid latitude summer atmosphere.....	95
Figure 5.3 Pressure profile for mid latitude summer atmosphere.....	95
Figure 5.4 Comparison between the net flux predictions of the present study and LBLRTM result for different number of grids with uniform spacing	97
Figure 5.5 Comparison between the downwelling flux predictions of the present study and predictions of LBLRTM for different non-uniform grids	99
Figure 5.6 Comparison between the upwelling flux predictions of the present study and predictions of LBLRTM for different non-uniform grids.....	99
Figure 5.7 Comparison between the net flux predictions of the present study and predictions of LBLRTM for different non-uniform grids.....	100
Figure 5.8 Comparison between the downwelling flux predictions of the present study and predictions of LBLRTM for different grid size weights (az)	102
Figure 5.9 Comparison between the upwelling flux predictions of the present study and predictions of LBLRTM for different grid size weights (az).....	103
Figure 5.10 Comparison between the net flux predictions of the present study and predictions of LBLRTM for different grid size weights (az).....	103
Figure 5.11 Comparison between the change in surface temperature for different coupling interval and simultaneous solution.....	107
Figure 5.12 Comparison between the change in temperature at 4 km above the surface for different coupling interval and simultaneous solution.....	107
Figure 5.13 Comparison between the change in temperature at top of the atmosphere for different coupling interval and simultaneous solution	108
Figure D.1 Schematic representation of 8 points.....	139

LIST OF SYMBOLS

a	gray gas weights, [-]
az	grid size weight
C_{abs}	absorption cross section, [mol/m ²]
\tilde{C}_{abs}	supplemental absorption cross-section, [mol/m ²]
C_D	drag coefficient, [-]
C_p	specific heat, [kJ/kgK]
C_{ij}	coefficients, [-]
$div \mathbf{q}$	source term, [kW/m ³]
E	eccentricity of the orbit, [-]
E_1	exponential integral of order 1, [-]
F	blackbody fractional function, [-]
g	acceleration due to gravity
I	radiative intensity, [W/m ² sr]
IF	longwave radiative heat flux, [W/m ²]
k_t	time constant, [(m/s) ⁻¹]
K_H	thermal diffusivity, [m ² /s]

L	distance between parallel plates, [m]; latent heat of evaporation, [kJ/kg]
LH	latent heat, [W/m ²]
m	discrete direction, [-]
MW	molecular weight, [g/gmol]
\mathbf{n}	unit normal vector, [-]
N	molar density, [mol/m ³]
P	pressure, [atm]
P^{sat}	saturation pressure of water vapor
p_i	poles, [-]
q	humidity, [ppm]
q^*	saturation humidity, [ppm]
q	radiative heat flux, [kW/m ²]
q^+	incident radiative heat flux, [W/m ²]
q^-	leaving radiative heat flux, [W/m ²]
q_{net}	net radiative heat flux, [kW/m ²]
Q_c	convective flux, [W/m ²]
\mathbf{r}	position vector, [-]
R	gas constant, [Latm/molK]
RH	relative humidity, [ppm]

s	distance, [m]
S	solar heat flux, [W/m ²]
SH	sensible heat, [W/m ²]
t	time, [s]; pseudo-time variable, [s]
T	temperature, [K]
V	surface wind, [m/s]
w_m	quadrature weight for ordinate m , [-]
z	co-ordinate axis, [-]
Z	thickness

Greek Symbols

α	band strength parameter, [cm ⁻¹ /(g/m ²)]
β	line overlap parameter, [-]
ϕ	azimuthal angle, [rad]
η	wave number, [cm ⁻¹]
κ	eddy diffusion coefficient, [cm ² /s]; gray gas absorption coefficients, [m ⁻¹]
μ	direction cosines, [-]
θ	polar angle, [rad]
ρ	density, [kg/m ³]

σ	Stefan-Boltzmann constant, $=5.67 \times 10^{-8}$ [W/m ² K ⁴]
ω	band strength parameter, [cm ⁻¹]
ξ	direction cosines [-], re-ordered wave number, [cm ⁻¹]
ζ	direction cosines, [-]
ζ	direction cosine (μ, ζ, ξ), [-]
Γ	adiabatic temperature gradient, [1/K]
Ω	direction of radiation intensity, [-]
$d\Omega$	solid angle, [-]
Ω_m	ordinate direction, [-]
ϵ	error tolerance, [-]

Superscripts and Subscripts

b	black body
g	gas
j	gray gas
M	ocean mixed layer
s	boundary layer
t	print time
w	bottom surface
η	spectral variable
'	incident

Abbreviations

AFGL	air force geophysical laboratories
AR4	fourth assessment report of IPCC
BC	before Christ
BP	before present
CFC	chlorofluorocarbon
HCFC	hydrochlorofluorocarbon
DOM	discrete ordinates method
DOS+ISW	discrete ordinates scheme with infinitely small weight
DSS012	two-point upwind differencing scheme
DSS014	three-point upwind differencing scheme
EBM	energy balance model
ENSO	el niño southern oscillation
EOS	earth observing system
EWBM	exponential wide band model
GCM	general circulation model
GCR	galactic cosmic ray
IPPC	Intergovernmental Panel on Climate Change
LBL	line-by-line
LBLRTM	line-by-line radiative transfer model

MOL	method of lines
NOAA	national oceanic and atmospheric administration
ODE	ordinary differential equation
OLR	outgoing longwave radiation
PDE	partial differential equation
RTE	radiative transfer equation
TAR	third assessment report of IPCC
TSI	total solar irradiance
WBCK	wide band correlated- k
WMO	world meteorological organization
WSGG	weighted sum of gray gases

CHAPTER 1

INTRODUCTION

The question of global climate change has been a major item on the media and the political agenda for several years now. How the climate has varied since the ice age is of importance in understanding today's behavior of the climate. In order to understand the climate change, the components of the climate system and their interaction in between must be investigated. According to the reports prepared by the Intergovernmental Panel on Climate Change (IPCC) [1], the global temperature has increased by approximately 0.76°C over the last century and this increase is attributed to increased concentration of greenhouse gases (carbon dioxide, methane, etc.) in the atmosphere. However, researchers have been debating whether this is true or not. Climate models have been and being developed to understand the past climate variations and to enable future projections [2].

Atmospheric radiation model is the key component of climate models. Therefore, atmospheric radiation models were developed in isolation from the climate models. The simplest radiation models are based on the assumption of 1-D clear sky atmosphere containing absorbing-emitting medium for which radiative transfer equation (RTE) is solved analytically. Therefore, many investigators have used 1-D clear sky model to determine the effect of carbon dioxide, water vapor and temperature on the fluxes in the atmosphere and the surface of the earth.

To understand anthropogenically generated increases of the atmospheric carbon dioxide concentration on the atmosphere, investigators applied longwave clear-sky radiation models to investigate effect of doubling of CO_2 concentration without any change in the profiles of temperature and water vapor concentration throughout the atmosphere on the net flux for midlatitude summer atmosphere. Table 1.1 shows the range of investigation, gases considered in the model range of the

wavenumber, database, method used for property estimation and solution method in the literature. These studies have shown that the atmosphere is warmed when concentration of the carbon dioxide is doubled, although their models and input parameters are not exactly same.

Brindley and Harries [3] have investigated the impact of changes in the atmospheric compositions on the outgoing long wave radiation by using GENL2 line-by-line radiative transfer code and concluded that the percentage increases in column water vapor required to produce the same spectrally integrated forcing as that given by a doubling of CO₂ are 12 and 25 % for tropical and subarctic winter cases respectively.

Buehler et al. [4] have used tropical and subarctic winter scenarios to visualize the impact of large scale changes of humidity, carbon dioxide, and temperature on outgoing longwave radiation. For this purpose modified version of standard atmosphere given by McClathey et al. [5] were generated. The modifications were: (i) water vapor mixing ratio increased by 20 % throughout the column, (ii) water vapor mixing ratio decreased by 20 % throughout the column, (iii) carbon dioxide mixing ratio increased by 10 % throughout the column (double-CO₂), (iv) temperature increased by 1 K throughout the column keeping absolute humidity fixed, and (v) temperature increased by 1 K throughout the column keeping relative humidity fixed. The rationale for this set of modifications was to compare the sensitivity of outgoing longwave radiation showing the net flux at the top of the atmosphere (OLR) to humidity changes to the sensitivity to carbon dioxide and temperature changes. It was found that in the tropical case 20% humidity increase has a larger impact on OLR than the CO₂ doubling; in the subarctic winter case the CO₂ doubling has slightly larger impact. However, OLR is also strongly sensitive to changes in temperature because of the positive temperature dependence of the Planck function. For the tropical case a 1 K temperature increment throughout the atmosphere produces roughly the same effect on OLR as a 20 % humidity decrease.

Table 1.1 Conditions of the studies about the effect of doubling carbon dioxide concentration in midlatitude summer

	Mlawer et al. [6]	Clough and Iacono [7]	Feigelson et al. [8]	Morcrette [9]	Ridgway et al. [10]
Range of investigation (mbar)	1000 → 0.1	1000 → 0.1	1000 → 0	1000 → 0	1000 → 0.1
Gases considered in the model	H ₂ O, CO ₂ , O ₃ , CH ₄ , N ₂ O	H ₂ O, CO ₂ , O ₃	H ₂ O, CO ₂ , O ₃	H ₂ O, CO ₂ , O ₃	H ₂ O, CO ₂ , O ₃
Range of the wave number (cm⁻¹)	10-3000	10-3000	0-2600	0-2620	0-3000
Database	HITRAN 92 [11]	HITRAN 92 [11]	1980 AFGL* catalog [12]	1980 AFGL catalog [12]	1980 AFGL catalog [12]
Method used for property estimation	Correlated-k methods	Line-by-line	Line-by-line	Narrow band	Line-by-line and Broad band
Solution Method of RTE	Analytical solution	Analytical solution	Analytical solution	Analytical solution	Analytical solution

* AFGL: Air Force Geophysical Laboratories

For the subarctic winter case the +1 K temperature effect is even roughly twice the -20 % humidity effect. The OLR sensitivity to a 1 K temperature increase under fixed relative humidity is much smaller than to a pure temperature increase due to water vapor feedback.

In reality, the atmospheric radiation model in planetary atmosphere is used to evaluate radiative energy balance of the earth-atmosphere containing atmospheric gases, clouds and aerosols, etc. For atmospheric radiation model consisting of atmospheric gases, clouds and aerosols, RTE can not be solved analytically due to absorbing-emitting scattering medium. Therefore, RTE in the model is solved by using numerical methods. Moreover, in the atmospheric model containing clouds one- and multi-dimensional radiative transfer equation can be used to evaluate cloud-radiation interactions. Spherical harmonic method has been used to solve one- or multi-dimensional radiative transfer model in planetary atmospheres [13, 14]. Evans [15] developed the spherical harmonics discrete ordinate method, in which spherical harmonics are employed for computing the source function including the scattering integral and discrete ordinate method is used to integrate RTE spatially, and applied this model to multi-dimensional media [15, 16]. Monte Carlo Method has been utilized to study radiative transfer model in multi-dimensional atmosphere [17-19]. This method has a reputation as being rather slow for results with good accuracy [15]. Maruyama and his co-workers [20] have developed a radiation element method by the ray emission model, REM², and have investigated this method in different atmospheric radiative problems for one- and three-dimensional geometry [20-25]. Discrete Ordinate Method (DOM) is the most widely used method for the solution of RTE due to its accuracy and computational economy [26]. It is also considered as the best for representing the streaming of radiation [15]. DOM has been used to solve the radiative transfer equation for homogenous and nonhomogeneous 1-D atmosphere [27-38]. In addition to usage of discrete ordinate method in 1-D atmosphere, this method has been used in multi-dimensional atmospheric models (i.e. [39, 40]). Li et al. [41] have developed a new discrete ordinate algorithm based on the discrete ordinate scheme with an infinitely small weight (DOS+ISW) for computing the radiative transfer in 1-D atmosphere and found that DOS+ISW needs usually higher order discrete ordinate quadrature sets to achieve the same precision

as that of DOM.

However, the components of atmospheric model in climate models are transient multi-dimensional conservation equations except radiation transfer equation which is an integro-differential equation. Due to difficulty in solving the equations of atmospheric and radiation models simultaneously, radiation equations have been solved when input data such as concentration, temperature etc. were made available upon solution of equations of atmospheric models. Generally, time step of conservation equations are 10-30 minutes but RTE is called only once every 1-3 hours [42]. There is inaccuracy due to the fixed radiation fluxes over the intervening time steps.

Only a limited number of studies were carried out to investigate the effect of coupling interval of radiation field on the accuracy of the climate model. Morcrette [43] has compared the use of coupling interval of 3 hours with 20 minutes by using 10 days and four month seasonal observation data. It was found that in 10 day forecast, temperature errors display a stronger dependence on the temporal representation and the difference increases with height, particularly in the tropical areas where interactions among convection, clouds and radiation dominate; and the anomaly correlation of geopotential shows little sensitivity to more complete representation of the cloud-radiation interaction. It was concluded that in four month seasonal simulations, the small errors seen in 10 day forecast build up and a better temporal resolution of the radiation produces a colder stratosphere through cloud-radiation-convection interactions [43]. Venema and his coworkers [44] have studied two cases. In the first one, coupling interval was taken as 1 hour. In the second one, the coupling interval was taken as 5 minutes. In this study, a correlation for net fluxes obtained from regression analysis of three months atmospheric data (July to Sep. 2004) was used instead of the solution of RTE. If the difference between the fluxes obtained by the correlation and the ones calculated upon solution of RTE was large, δ -two stream method for the solution of RTE was deployed. The results found from coupling every hour and every 5 minutes are compared with those found from coupling every 2.5 minutes. Comparisons reveal that root mean square error in the net solar flux at the surface decrease from 77 W/m^2 to 43 W/m^2 and the error in the infrared net flux at the surface reduce from 15 W/m^2 to 9.1 W/m^2 as coupling interval

decreases from 1h to 5 minutes [44]. The root mean square for solar net radiative flux was still high even when 5 minutes coupling interval is used. Therefore, it can be concluded that instead of using correlation, radiative fluxes should be calculated with solution of radiative transfer equations.

Consequently, accurate and efficient solution technique for climate models requires compatibility between radiative transfer equation and partial differential equations (PDEs) governing other transport processes. Moreover, compatibility necessitates representation of the equations in the same form and use of the same numerical solution technique. Conservation equations are in the form of PDEs and the equation modeling radiation field can be represented by a PDE with the use of discrete ordinate method. Conservation equations can be solved accurately with a high computational efficiency using Method of lines (MOL) solution. To be compatible equation modeling radiation field should be solved with the same solution technique which is Method of Lines solution of Discrete Ordinate Method (MOL solution of DOM). MOL solution of DOM has been used for several test problems to test its accuracy. It was found to produce good agreement with exact solutions, Monte Carlo, zone method solutions and measurements [26, 45-53].

Accuracy of the radiation model is very sensitive to the radiation property estimation model utilized. Line-by-line (LBL) method (i.e. [7, 10, 54]) , which is a direct evaluation of the contribution of the individual lines of atmospheric absorption bands, is the most accurate of all. However, direct application of LBL calculations is unsuitable in numerical atmospheric models due to large computation times and at present, these calculations are most useful as benchmarks for testing and improving approximate techniques [8]. The significant computational burden required by LBL model has necessitated the use of band models which are designed to approximate the nongray gas behavior over wavenumber intervals within which the radiative properties are assumed to be constant [53]. Band models are categorized as narrow band [55-57] and wide band [58-62]. Disadvantage of these models is that they provide gas transmissivities or absorptivities instead of absorption coefficients, which are required for the solution of RTE and therefore there has been an increasing effort for the development of gas spectral radiative property estimation models which yield absorption coefficients and so they become suitable for incorporation into any

RTE solution technique [53]. k-distribution method [63, 64] assumes that the transmission within a relatively broad spectral interval depends on the k-values rather than the spectral ordering of k-values and this method has been demonstrated to be more accurate than band models but, more importantly, it allows for the treatment of multiple scattering by aerosol and cloud particles [65]. Moreover, numerical procedures have been employed to calculate the total band k-distribution functions [61, 65-69]. However, like other band-model methods, the k-distribution approach is developed for homogenous path and therefore, for nonhomogenous atmosphere, the one-parameter scaling approximation must be used, which can lead to large deviations from results computed from the LBL [70]. The correlated k-distribution method is an extension of the k-distribution to nonhomogeneous paths first proposed by Lacis et al. [71] and this model has been utilized in modeling of atmospheric radiation [70, 72, 73]. This model neglects the variation of blackbody intensity over a band and therefore enables the replacement of spectral integration over wavenumber within band by a quadrature over the absorption coefficient [53]. Correlated-k model has been extended to wide bands for combustion system, yielding wide band correlated-k (WBCK) [74-77]. In the WBCK model, the wave number spectrum is re-ordered to yield a smooth function of the absorption coefficient around the band centers within the wide band, so that for a certain wave number interval, a set of mean values of the absorption coefficient can be introduced [78]. For the re-ordered wave number, Denison and Fiveland [76] developed a closed form function. Implementation of this function to WBCK model was demonstrated on solution of RTE by DOM [78]. MOL solution of DOM was utilized to treatment of one-dimensional parallel plane and two-dimensional axisymmetric cylindrical non-grey media for combustion system by using WBCK as radiative property estimation model and its results were found to be in agreement with LBL results. Moreover, WBCK is computationally efficient [53, 79, 80] and its correlation parameters are suitable to atmospheric conditions.

Therefore, the first objective of the present study has been to investigate the effect of carbon dioxide, water vapor and temperature on the radiative fluxes in the atmosphere and earth's surface. To achieve this objective, Line-by-line Radiative Transfer Model (LBLRTM) developed by Clough et al. [81] based on analytical

solution of RTE with LBL was utilized for 1-D longwave clear sky atmosphere. The second objective of the present study has been to develop a radiative-convective model with radiation model based on MOL solution of DOM with WBCK for determining the effect of coupling interval on the accuracy of the radiative-convective model. To achieve this objective, MOL solution of DOM with WBCK developed by Çayan and Selçuk [79, 80] was adapted to 1-D longwave clear sky atmosphere and its predictive accuracy and computational efficiency was examined on the test problem by using benchmark solution obtained from LBLRTM. The radiation code was then coupled with radiative-convective model and the predictive accuracy of this model was examined for several coupling intervals.

CHAPTER 2

BACKGROUND

In this section, various issues associated with Earth's atmosphere and climate are briefly overviewed to understand climate change phenomenon.

2.1 Earth's Atmosphere

The Earth is the third planet from the Sun and the fifth in the solar system in terms of size and mass. Its single most outstanding feature is that its near-surface environments are the only places in the universe known to harbour life [82].

It is widely accepted by both geologists and astronomers that the Earth is roughly 4.6 billion years old. This age has been obtained from the isotopic analysis of many meteorites as well as of soil and rock samples from the Moon by such dating methods as rubidium–strontium and uranium–lead. Moreover, The Earth and meteorites have had similar lead-isotope histories, and so it is concluded that they condensed or accreted as solid bodies from a primeval cloud of interstellar gas and dust—the so-called solar nebula from which the entire solar system is thought to have formed—at about the same time. Particles in the solar nebula condensed to form solid grains, and with increasing electrostatic and gravitational influences they eventually clumped together into fragments or chunks of rock. One of these planetesimals developed into the Earth [83].

2.1.1 The Early Atmosphere

Earth's very earliest atmosphere probably was swept into space by a solar wind, a vast stream of particles emitted by the Sun. As Earth slowly cooled, a more enduring atmosphere formed. The molten surface solidified into a crust, and gases that had been dissolved in the molten rock were gradually released, a process called

outgassing. Outgassing continues today from hundreds of active volcanoes worldwide. Thus, geologists hypothesize that Earth's original atmosphere was made up of gases similar to those released in volcanic emission today: water vapor, carbon dioxide, nitrogen, and several trace gases [84].

As the planet continued to cool, the water vapor condensed to form clouds and great rains commenced. At first, the water vapor evaporated in the hot air before reaching the ground, or quickly boiled away upon contacting the surface. This accelerated the cooling of Earth's crust. When the surface cooled below water's boiling point (100 °C or 212 °F), torrential rains slowly filled low areas, forming the oceans. This reduced not only water vapor in the air but also the amount of carbon dioxide, for it became dissolved in the water [84]. In addition, much of the carbon became locked up in sedimentary rocks [85]. In fact, carbon dioxide must have been a good a deal more abundant than it is now. If these carbon-containing sediments are converted back into carbon dioxide and distributed between ocean and atmosphere in the ratio 60:1 that prevails today, the carbon dioxide content of the atmosphere should have been more than a 100 times greater than today [86]. Therefore, the chemically inactive gas nitrogen gradually came to dominate the Earth's atmospheric composition [85].

Oxygen was a later arrival, only reaching 10 percent of present concentrations about 1 billion years ago, probably mainly as a result of the sun's energy splitting water vapor molecules into their constituent elements. The hydrogen, being light, could escape more easily to space, leaving oxygen in small concentrations behind. Due to the thinness of the oxygen layer, ultraviolet radiation could penetrate down to the surface, inhibiting the development of life forms, unless they were shielded by a considerable depth of ocean. Only slowly did photosynthesis raise the concentration of oxygen to present levels by about 300 million years ago, by which time terrestrial life forms were established [85]. The Precambrian rock record suggest that much of the first free oxygen did not remain free because it combined with (oxidized) other substances dissolved in water, especially iron. Iron has tremendous affinity for oxygen, and the two elements combine to form iron oxide (rust) at any opportunity. Then once, the available iron satisfied its need for oxygen, substantial quantities of oxygen accumulated in the atmosphere. By the beginning of

the Paleozoic era, about 4 billion years into Earth's existing, the fossil record reveals abundant ocean-dwelling organisms that require oxygen to live. Hence, the composition of Earth's atmosphere has evolved together with its life forms, from an oxygenless envelope to today's oxygen-rich environment [84].

2.1.2 The Atmosphere Today

Consequently, present atmosphere contains mostly the nitrogen and oxygen, although its compositions vary from time to time and place to place. According to NASA updated data [87], the composition of the dry air by volume can be seen in Table 2.1. NASA obtained data from the Earth Observing System (EOS) which is a coordinated series of polar-orbiting and low inclination satellites for long-term global observations of the land surface, biosphere, solid Earth, atmosphere, and oceans [88].

Table 2.1 Compositions of the Earth's atmosphere [87]

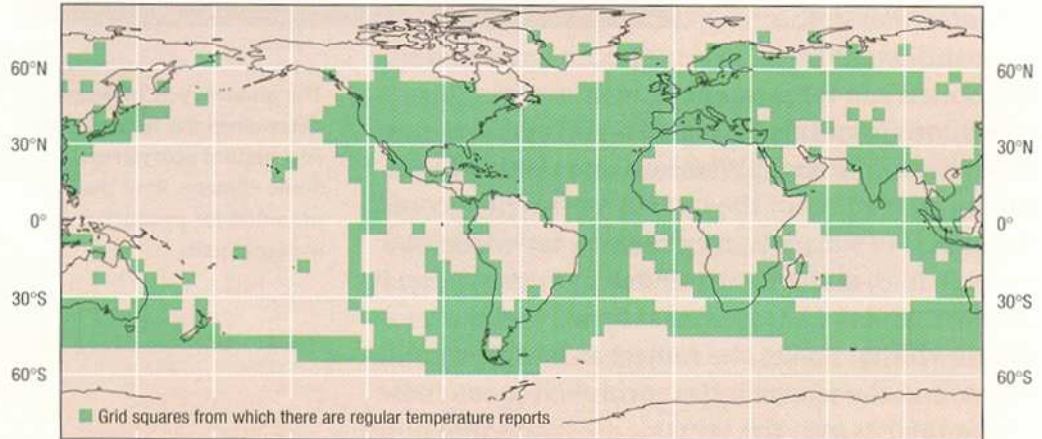
Major Gases		
<i>Gas</i>	<i>Formula</i>	<i>% by volume</i>
Nitrogen	N ₂	78.084
Oxygen	O ₂	20.946
Minor Gases		
<i>Gas</i>	<i>Formula</i>	<i>ppm</i>
Argon	Ar	9340
Carbon Dioxide	CO ₂	380
Neon	Ne	18.18
Helium	He	5.24
Methane	CH ₄	1.7
Krypton	Kr	1.14
Hydrogen	H ₂	0.55
Water	H ₂ O	0-10000

2.1.3 Measurement Techniques of the Atmospheric Profile

The basis for modern weather and climate networks was laid during the later part of 19th century as governments realized that mapping weather systems could provide valuable public information, especially for rural decisions and safety of shipping. The observations systematically carried out at fixed times of the day, were recorded in field books that were regularly forwarded to headquarters for the compilation of climate statistics. As can be seen in Figure 2.1, at the beginning of the 20th century there were quite extensive meteorological observing networks covering the lands of both hemispheres, although with significant gaps and by the end of the 20th century, these were mostly filled. The weather networks that evolved have had an emphasis on rapid collection of essential elements for forecasting, particularly, temperature, pressure, humidity, wind speed and direction, and precipitation. A wide range of different observation systems, on land, at sea, in the air and from space can be seen in Figure 2.2 [89].

At sea the challenge of building up a complete climatic picture was more demanding. Nevertheless, from the middle of 19th century in many parts of the world, arrangements were made to obtain systematic records from ships. The collection of these data and their analysis provided guidance to mariners on a range of conditions at sea. Information gathered included air and sea surface temperature, air pressure, wind speed and direction, wave height, the extent of sea ice and visibility. All of these were used initially to assist navigation and improve safety, but have since proven invaluable for research into the climate system. New technologies have made more observations possible and so the nature of the measurement systems has evolved over time. However, it was not until the 1950s & 1960s that some national weather services started to record these data in compute-compare forms [89].

Greater than 50% coverage for temperature observations, 1891 through 1910



Greater than 50% coverage for temperature observations, 1970 through 1999

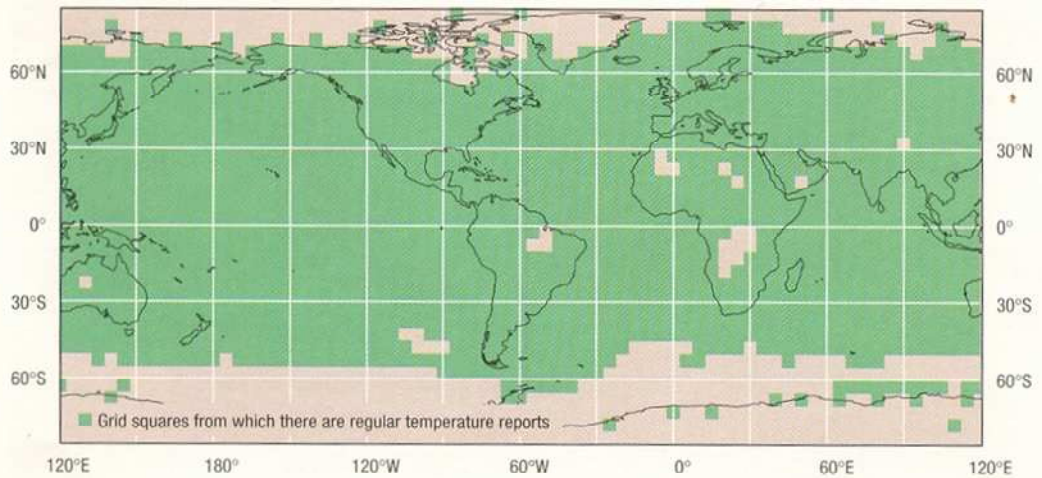


Figure 2.1 At the beginning of the 20th century there were large gaps in the global network for regularly observing and reporting surface temperature, but by the end of the century these were mostly filled, except for the inhospitable polar regions [89]

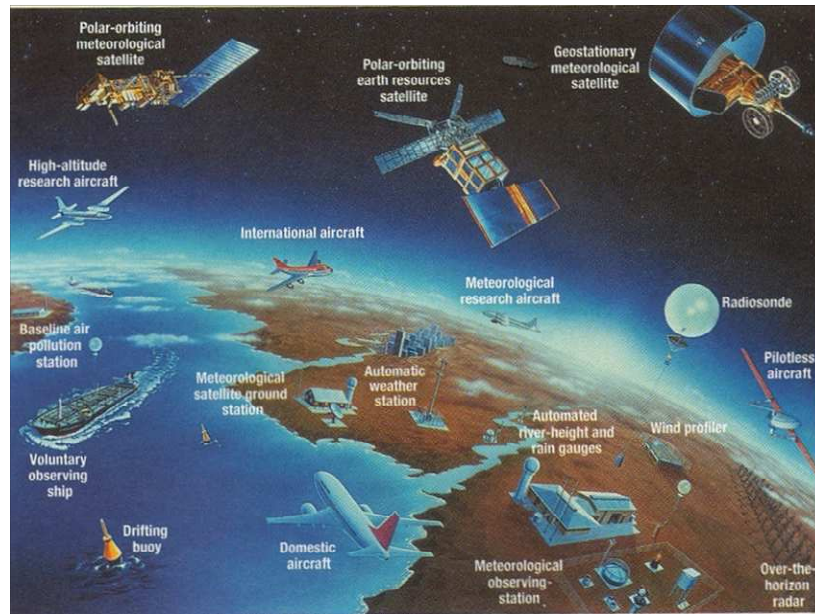


Figure 2.2 Monitoring the Earth's weather and building up the best possible picture of the climate involve a wide range of different observation systems, on land, at sea, in the air and from space [89]

Upper air observations were much more difficult to make. Although manned balloon flights were carried out occasionally, these proved dangerous and occasionally fatal. Kites became a favored alternative. Tethered kites were routinely used to carry an instrument package aloft by the end of 19th century. But the height these could reach was only about 3 km and observations could only be made in good weather conditions with relatively light winds [85]. During the 1920s aircrafts were used to measure conditions in the lower atmosphere [89]. These could reach higher altitudes, but again could be grounded in poor weather. Their data also could only be analyzed some hours after they had been made [85]. During World War II, as aircraft were flying higher, pilots discovered exceptionally strong winds at 6 to 7 km altitudes. These first encounters with the jet stream and the realization that it was linked with large-scale atmospheric circulation patterns controlling many features of the weather, was an eye-opener to meteorologists. Its implications for safe air travel

created an urgent demand for routine observations of conditions aloft. This accelerated the development of new technologies to measure the upper atmosphere and regular balloon-borne measurements (radiosonde) became a part of meteorology [89]. The radiosonde is a small expendable set of instruments hung from a helium or hydrogen filled balloon. Sensors for temperature transmit pressure and temperature continuously back to a base station as the balloon rises. A radar reflector attached to the balloon enables the ground station to track the height and rate of ascent of the balloon and also the wind direction and speed at various heights. A profile through the atmosphere is provided until the reduction in air pressure results in the balloon expanding to bursting point, or atmospheric conditions cause the ground station to lose contact. Some balloons reach 40 km before bursting and parachute allows a gentle descent to occur [85].

Since 1960s, meteorological observations of the atmosphere have increasingly been carried out from orbital platforms. Some of these satellites are located in geostationary orbits 36,000 km above the surface. As they orbit at the same rate the earth turns, they are therefore capable of imaging the same area below them on continuing basis. Others are polar orbiters which image different areas on their pole-to-pole journey as the earth rotates beneath them. Most of these platforms involve passive systems whereby electromagnetic radiation being emitted or reflected from the atmosphere or surface is measured in specific wavebands, particularly in visible and infrared wavelengths. Gases in the atmosphere selectively absorb both incoming and outgoing radiation at particular wavelengths and by measuring how much radiation are occurring at a particular wavelength, temperature and atmospheric composition may be inferred. A second form of sensing depends on active generation of electromagnetic energy at specific wavelengths. By measuring the return flow of pulses of generated energy, the satellite can also enable atmospheric composition to be inferred. Passive sensing is particularly useful for cloud analysis due to the high reflectivity of clouds [85]. Now, satellites measure a whole host of different features of climate system, including the temperature throughout the depth of the atmosphere and of the surface of the land and the oceans [89].

2.1.4 Vertical Structure of the Atmosphere

The atmosphere is vertically divided into five layers on the basis of temperature, chemical composition, movement and density as illustrated in Figure 2.3. Each of the layers are bounded by "pauses" where the maximum changes in thermal characteristics, chemical composition, movement and density occur [90].

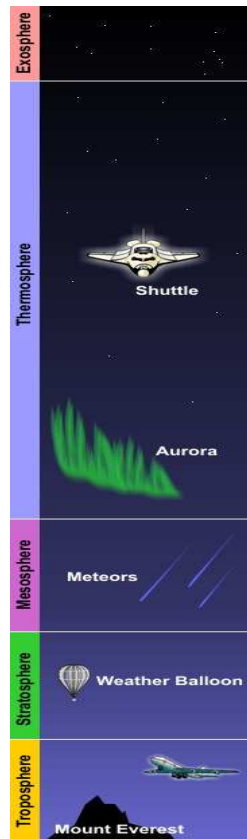


Figure 2.3 Layers of atmosphere [90]

2.1.4.1 Troposphere

The troposphere begins at the Earth's surface and extends up to 4-12 miles (6-20 km) high. The height of the troposphere varies from the equator to the poles. At the equator it is around 11-12 miles (18-20 km) high, at 50°N and 50°S, 5½ miles (~9 km) and at the poles just under 4 miles (~6 km) high [90]. About 75% of the mass of the atmosphere and almost all the water vapor and aerosols are contained in this layer [85]. Almost all weather occurs in this layer. As the gases in this layer decrease with height, the air becomes thinner [90]. Therefore, the temperature in the troposphere also decreases with an increase in altitude and the temperature falls by an average of 6.5°C/km [84]. The temperature decreases in the troposphere is called the environmental lapse rate. In troposphere, the temperature drops from 62°F (17°C) to -60°F (-51°C) [90].

The transition boundary between the troposphere and the layer above is called the tropopause. Both the tropopause and the troposphere are known as the lower atmosphere [90].

2.1.4.2 Stratosphere

The Stratosphere extends from the tropopause up to 31 miles above the Earth's surface. This layer holds 19 percent of the atmosphere's gases, but very little water vapor. Temperature increases with height as radiation is increasingly absorbed by oxygen molecules which lead to the formation of ozone. In stratosphere, the temperature rises from -76°F (-60°C) to 5°F (-15°C). The transition boundary which separates the stratosphere from the mesosphere is called the stratopause. The regions of the stratosphere and the mesosphere, along with the stratopause and mesopause, are called the middle atmosphere by scientists [90].

2.1.4.3 Mesosphere

The mesosphere extends from the stratopause to about 53 miles (85 km) above the earth. The gases, including the oxygen molecules, continue to become thinner and thinner with height. As such, the effect of the warming by ultraviolet radiation also becomes less and less leading to a decrease in temperature with height. However, the gases in the mesosphere are thick enough to slow down the meteorites

hurtling into the atmosphere, where they burn up, leaving fiery trails in the night sky. In mesosphere, the temperature drops from 5°F (-15°C) to -184°F (-120°C). The transition boundary which separates the mesosphere from the thermosphere is called the mesopause [90].

2.1.4.4 Thermosphere

Thermosphere extends from the mesopause to 430 miles (690 km) above the earth. This layer is known as the upper atmosphere. The gases of the thermosphere are increasingly thinner than in the mesosphere. Only the higher energy ultraviolet and x-ray radiation from the sun is absorbed. But, because of this absorption, the temperature increases with height and can reach as high as 3600 °F (2000°C) near the top of this layer [90]. However, such temperatures are not comparable to those experienced near Earth's surface. Temperature is defined in terms of the average speed at which molecules move. Because the gases of the thermosphere are moving at very high speeds, the temperature is very high. But the gases are so sparse that, collectively, they possess only an insignificant quantity of heat. For this reason, the temperature of a satellite orbiting Earth in the thermosphere is determined chiefly by the amount of solar radiation it absorbs and not by the high temperature of the almost nonexistent surrounding air. If an astronaut inside were to expose his or her hand, it would not feel hot [84].

2.1.4.5 Exosphere

Exosphere is the outermost layer of the atmosphere and extends from the thermopause to 6,200 miles (10,000 km) above the earth. In this layer, atoms and molecules escape into space and satellites orbit the Earth. The transition boundary which separates the exosphere from the thermosphere below it is called the thermopause [90].

In the atmosphere, temperature and pressure vary vertically as a function of height. As can be seen in Figure 2.4, pressure decreases rapidly near Earth's surface and more gradually at greater heights. The average sea level pressure is slightly more than 1000 millibars. At 3 km high in the atmosphere, the air column above is 3 km shorter than the surface. Air pressure is thus reduced considerably to about 700 mbar

that height. At 10 km elevation, it is less than 300 mbar [85]. In Figure 2.5, the temperature as function of altitude is decreasing linearly in troposphere from 17 °C at the surface to -51 °C and then increasing in stratosphere to -3 °C. It decreases again in mesosphere to -90 °C and rises in thermosphere up to 2000 °C [90].

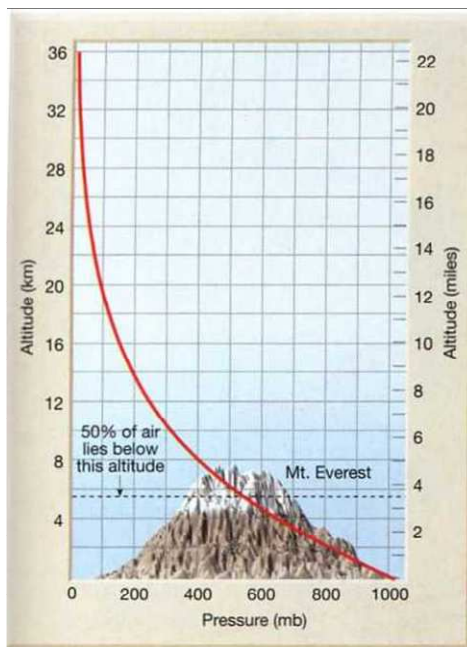


Figure 2.4 Atmospheric pressure variation with altitude [84]

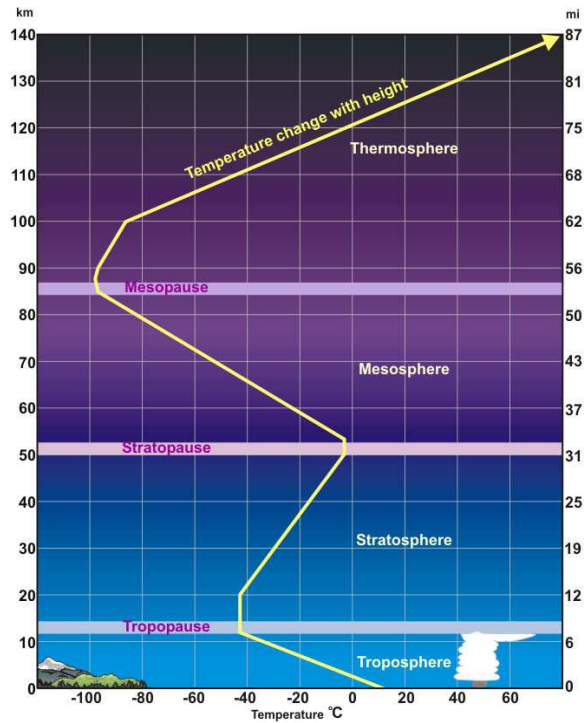


Figure 2.5 Average temperature profile of the atmosphere [90]

2.2 Climate

Climate derived from the Greek word “*klima*” is *defined as the average weather in terms of the mean and variability of relevant quantities over a period of time ranging from months to thousands or millions of years*. The classical period is 30 years, as defined by the World Meteorological Organization (WMO) [85].

2.2.1 Climate System

Climate is the end product of a multitude of interactions between several different subsystems - the atmosphere, oceans, biosphere, land surface and cryosphere - which collectively make up the climate system. As can be seen in Figure 2.6, each subsystem is coupled in some way to the others such that changes in one system may give rise to changes elsewhere [91].

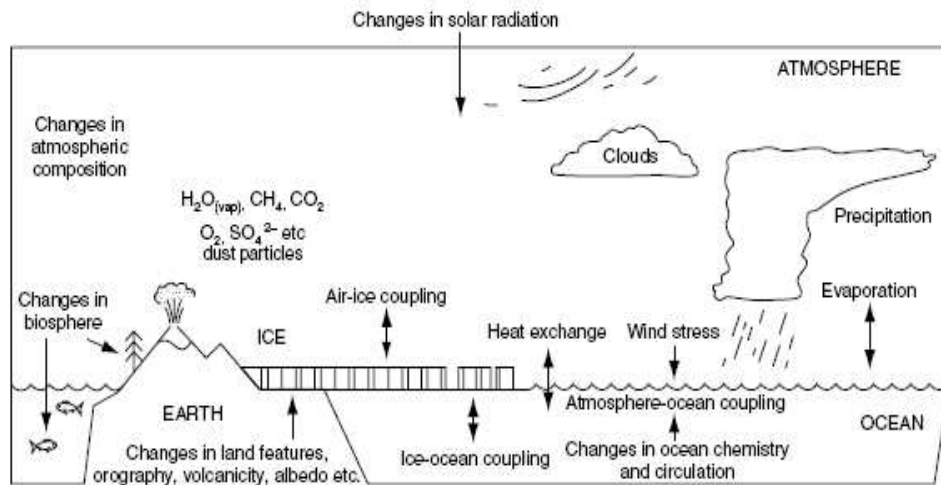


Figure 2.6 Schematic diagram of major components of the climate system. Feedbacks between various components play an important role in climate variations [91]

Of the five principle subsystem, the atmosphere is the most variable. It has relatively low heat capacity and responds to external influences most rapidly. It is coupled to other components of the climate system through energy exchanges at the surface as well as through chemical interactions that may affect atmospheric components [91]. The water bodies of the world, or hydrosphere, store and relocate the sun's energy and respond also to changes in the composition in the atmosphere [85]. Surface layers of the ocean respond to external influences on a timescale of months to years, whereas changes in the deep oceans are much slower; it may take centuries for significant changes to occur at depth. Because water has a much higher heat capacity than air, the ocean store very large quantities of energy, and act as a buffer against large seasonal changes of temperature [91].

The oceans play a critical role in the chemical balance of the atmospheric system, particularly with respect to atmospheric carbon dioxide levels. Because the

oceans contain very large quantities of CO₂ in solution, even a small change in the oceanic CO₂ balance may have profound consequences for the radiation balance of the atmosphere and hence climate. The role of the oceans in global CO₂ exchanges is of particular importance, not only for an understanding of past climatic variations but also for insight into future CO₂ trends in the atmosphere [91].

The cryosphere, ice bodies of the world, respond very slowly to external changes, on the timescale of decades to centuries. They influence the reflectivity of the surface to solar radiation and also the operation of deep ocean circulations. Land surface, lithosphere, interacts with other components of the climate system on all timescales [91]. It moves to rearrange place over long timescales and provides mechanisms, such as volcanoes, which affect the composition of the atmosphere [85]. The final component of the climate system is the biosphere, consisting of plants and animals in the world, though vegetation cover and type are mainly of significance for climate. Vegetation affects the albedo, roughness and evapotranspiration (the combined loss of water from the soil and surface to the atmosphere by evaporation and plant transpiration), characteristics of a surface and also changes the atmospheric composition through the removal of carbon dioxide and the production of aerosols and oxygen [91].

2.2.2 Energy Budget of the Earth

To understand how the Earth's climate system functions, it is needed to know how the sun's energy drives the whole system. At the most fundamental level these processes are all about how much solar energy is absorbed by the Earth and how this energy is re-radiated at longer wavelengths to space in the form of infrared terrestrial radiation. Over time the Earth's climate system remains largely stable because the energy received is equal to that lost [89].

The sun emits radiation as if its surface temperature were about 5700 °C. However, the intensity of its radiant heat decreases with distance and so the Earth is bathed in an average solar influx of 1370 watts per square meter. As the Earth is spherical, each square meter receives on average one fourth of this, or, about 342 W/m² [89]. As can be seen in Figure 2.7, this amount can be simplified to represent as 100 units of energy.

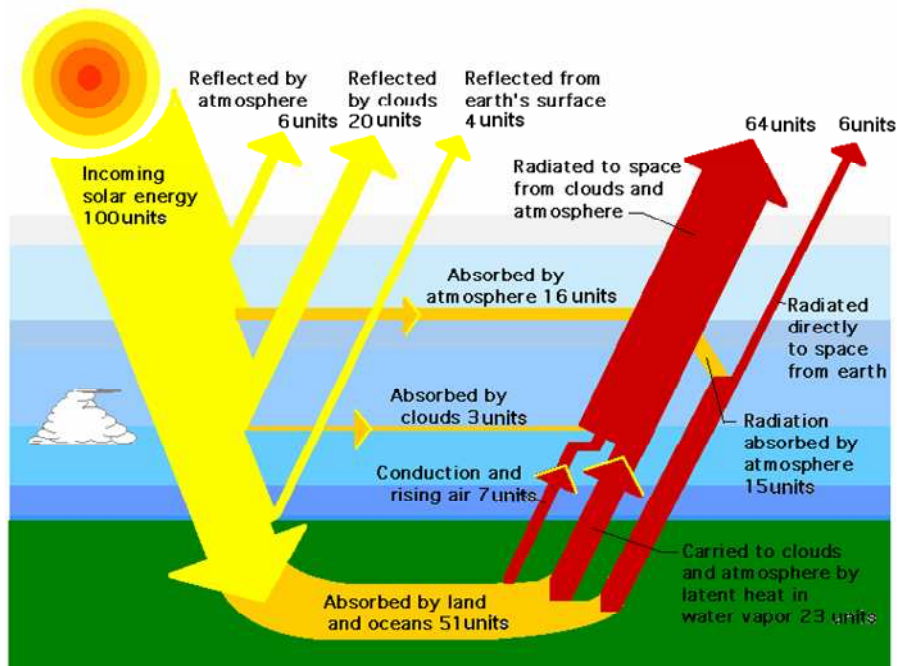


Figure 2.7 The Earth's energy budget adapted from [92]

6 units of this amount are scattered upward by the molecules and particulates in the atmosphere, 20 units of this amount are reflected by clouds and 4 units of this amount are reflected by Earth's surface. In total, 30 units of the incoming solar energy reflected and scattered by earth-atmosphere system play no role in the warming the earth. However, the remaining energy, 70 units of the solar energy, are absorbed by clouds and other atmospheric constituents (19 units) and particularly by surface, including land and oceans, (51 units) and are converted into heat which warms the earth-atmosphere system [85]. Energy is re-radiated from the Earth's surface at longer wavelength [91]. 6 units are directly lost to space through the atmospheric window in the region of 8-14 μm . 15 units are absorbed by the atmosphere, clouds and atmospheric gases such as water vapor and carbon dioxide. Although solar and thermal radiations dominate energy balance of earth-atmosphere system, conduction and convection are also important. 7 units are transferred from

the surface by conduction and convection and 23 units carried to clouds and atmosphere by latent heat in water vapor. 64 units are radiated to space from clouds and atmosphere [85].

2.2.3 Climate Forcings

The climate system is a dynamic system in transient balance. A climate forcing is a change imposed on the planetary energy balance that causes a change in global temperature. Forcing imposed on the climate system can be considered in two separate categories: external forcing and internal forcing [42].

2.2.3.1 External Forcings

External forcings are caused by variations in agents outside the climate system such as Milankovitch variations, solar radiation fluctuations. Milankovitch theory is an attempt to relate climatic variations to a change in parameters of Earth's orbit around the Sun. The orbit of Earth is an ellipse around the Sun. The Earth's orbit becomes more eccentric (elliptical) and then more circular in a pseudo-cyclic way, completing the cycle in about 110 000 years. The mean annual incident flux varies as a function of eccentricity of the orbit, E . There is a smaller incident annual flux for a larger value of eccentricity of the orbit. The current value of E is 0.017. In the last 5 million years, it has varied from 0.000483 to 0.060791, resulting in changes in the incident flux of +0.014 % to -0.170 % from the current value [42].

The obliquity or the tilt of Earth's axis rotation is the angle between the Earth's axis and the plane of the elliptic. Changes in the obliquity affect seasonal variations. If the obliquity is large, seasonal variations are greater, resulting in warmer summers and colder winters. Obliquity ranges from about 22° to 24.5° and current value is 23.5° . The point of the Earth's elliptical orbit closest to sun, perihelion, moves into space due to gravitational interaction with other planets so that the ellipse is moved around in space. This orbit precession may cause a progressive change in the time equinoxes. These changes affect its temporal and spatial distribution. The variations in these orbital components can be seen in Figure 2.8 [42].

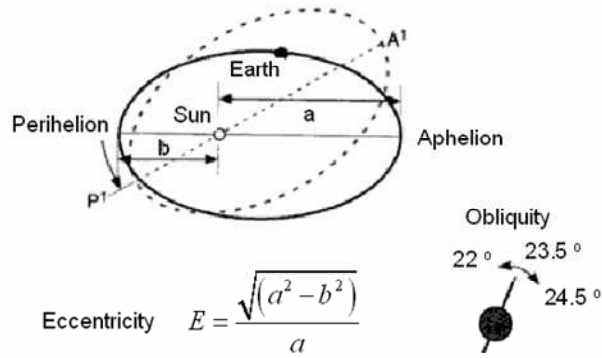


Figure 2.8 Schematic diagram showing the variations of the three orbital components: obliquity (axial tilt), orbital eccentricity and precession of the perihelion [42]

Variations in the climate during historical times have been linked with the sunspot cycle, which is a second possible cause of solar-produced climatic change. This cycle occurs with a 22 year periodicity: the ‘Hale’ double sunspot cycle. The overall amplitude of the cycles seems to increase slowly and then fall rapidly with a period of 80-100 years and also there appears to be a quasi-cyclic fluctuation of the order of 180 years [42].

2.2.3.2 Internal Forcings

Internal forcing, such as that due to volcanic eruptions, ice-sheet changes, CO₂ increases and deforestation, are variation in components of the climate system. Internal forcings are caused by two major groups of changes: human-induced changes and natural changes [42].

2.2.3.2.1 Human-induced Changes

Today’s climate concern centre on the possible impacts of human activities such as the emission of greenhouse gases and aerosol, changes in land-use and depletion of stratospheric ozone. After the industrial revolution, concentration of a number of greenhouse gases such as carbon dioxide, methane and nitrous oxide

increased. Apart from the water vapor, carbon dioxide is the major component of the natural greenhouse effect [42]. The greenhouse gases absorb outgoing long wave radiation. This is trapped and reradiated back to the Earth's surface [85].

The emission of aerosols is also believed to affect the climate. The influence of volcanic aerosol on climate has long been recognized, but the influence of tropospheric aerosols associated with industrial pollution has only recently been, to some extent, quantified. Solid sulphate particles result from the oxidation of sulphur dioxide emitted when fossil fuels are burned. Other industrial processes also contribute droplets and particulate material to the troposphere. These aerosols are localized and have two effects on the climate system. The direct effect of most aerosols is to reflect some solar radiation back into space and so act to cool the affected area, although some particulates, such as soot, are dark in color and have the opposite effect, causing local warming. There is also an important indirect effect of tropospheric aerosols. They act as additional cloud condensation nuclei and cause more, smaller, drops to form in clouds, increasing the reflectivity of the clouds, further cooling the planet [42].

The depletion of stratospheric ozone is a result of chlorofluorocarbons (CFCs) and hydrochlorofluorocarbons (HCFCs) emitted from human activities. Since CFCs are practically inert in the lower atmosphere, a portion of these gases gradually makes its way to the ozone layer, where sun-light separates the chemicals into their constituent atoms. The chlorine atoms released this way, through a complicated series of reactions, have the net effect of removing some of the ozone. Because ozone filters out most of the ultraviolet radiation from the Sun, decrease in its concentration permits more of these harmful wavelengths to reach Earth's surface [84].

Humans also change the character of Earth's surface by desertification, re- and deforestation, urbanization and river, lake and dam engineering [42].

2.2.3.2.2 Natural Changes

Volcanoes influence climate system by projecting large quantities of particulate matter (dust, ash, condensed water droplets) and gases (water vapor, carbon dioxide and sulphur dioxide) into the atmosphere [42]. Some gases and the

heavier particles only reaching levels below 10 km have a short residence time in the atmosphere [85] and are quickly removed by gravitational fall-out or rain-out [42]. However, gases, which are light, especially sulphur dioxide, can linger for much longer if they are injected to heights beyond the troposphere, into lower stratosphere. Recall that unlike the troposphere, the stratosphere becomes warmer with height. This means it is quite stable and material injected into it is not subject to rapid dispersion. The sulphur dioxide emissions from a large explosive event react with water vapor in the presence of sunlight to form tiny reflective sulphate droplets and particles which can remain suspended in the atmosphere for lengthy periods [85]. The residence time is in the order of a year for aerosol of radii 2-5 μm whereas it is 12 years for smaller aerosols of radii 0.5-1.0 μm . These aerosols increase the albedo of the atmosphere and reduce the amount of solar radiation that reaches the surface [42].

The ocean is one of the main constituents of the climate system. Therefore, any changes in the ocean directly affect the climate system. The El Niño Southern Oscillation (ENSO) phenomenon is one of the best-defined modes of so-called internal climate variability. It has an oceanic - El Niño and La Niña – and an atmospheric – the Southern Oscillation – component [93].

An ENSO event is a large-scale ocean-atmosphere system in the Pacific that switches mode periodically from a warm phase El Niño episode to a cold phase La Niña episode. Under ‘normal’ conditions in the Pacific, cold water, high pressure and low rainfall are found in the central and eastern regions, while warm water, low pressure and wet conditions prevail in the western regions as illustrated in Figure 2.9 (a). El Niño events change the ‘normal’ condition and are recognized by the development of anomalously warm water over the central and eastern Pacific (seen in Figure 2.9 (b)). During an El Niño, warm water and low pressure over the central and eastern part of the Pacific Basin bring wet conditions to countries like Tahiti, Peru, and Ecuador, while cool water and high pressure over the western part of the basin encourage low rainfall in Australia and Indonesia. A La Niña is the converse of an El Niño with very cold water, strong high pressure and very dry conditions in the eastern Pacific and very warm water, severe low pressure and very wet conditions in the western Pacific (seen in Figure 2.9 (c)). ENSO events involving the switch from

El Niño to La Niña conditions alter not only local and regional climate (droughts, intense rainfall) but also climate patterns at the global scale [85]. The change in tropical temperatures is sufficient to affect global-mean temperature, creating a rise and fall of a couple of tenths of a degree Celsius every few years (can be seen in Figure 2.10) [93].

Evidence shows that ENSO events have become more intense and more frequent in the last 30 years or so, and it is probable that such a trend will continue in the future. It is difficult to separate out the individual effects of El Niño events and those attributed to global warming since many of their impacts are similar (i.e. global heating, greater storminess) [85].

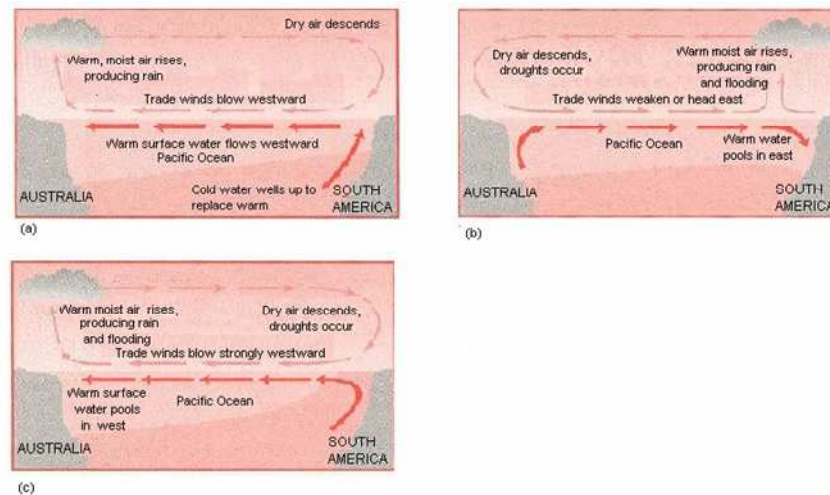


Figure 2.9 An ENSO event showing three stages in ocean-atmosphere coupling: (a) standard condition; (b) warm phase El Niño; (c) cold phase La Niña [85]

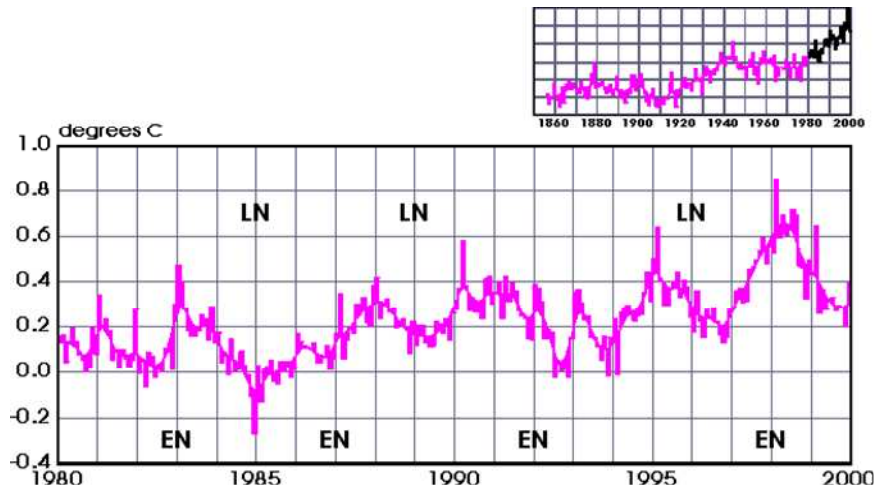


Figure 2.10 Global-mean monthly temperature for the period 1980-1999, showing the effects of El Niño (EN) and La Niña (LN). At the global scale, the effects of the Pinatubo eruption masked the warming induced by the 1991/92 El Niño event, although the regional impacts of that El Niño event did occur. The upper graph shows the complete global-mean temperature record as context [93]

2.2.4 Climate Feedbacks

Interactions within the climate system often involve complex and non linear relationships. Changes in one subsystem may involve compensatory changes throughout the entire climate system. These changes may amplify the initial disturbance or dampen it. Interactions that tend to amplify the disturbance are termed positive feedback mechanisms or processes; they operate in such a way that the system is increasingly destabilized. Interactions that tend to dampen the initial disturbance are termed negative feedback mechanisms [91]. Among the most significant of feedbacks are the ice albedo, water vapor and cloud feedback effects [85].

The ice-albedo effect is a positive feedback which occurs because ice/snow coverage changes enhance themselves [85]. For example, if some external or internal perturbation acts to decrease the global surface temperature, additional areas of snow and ice are likely to be formed. Since the albedos of snow and ice are high due to

their brightness and color, they reflect almost all the solar radiation incident upon them. This results in a decrease in the temperature. A further increase in snow and ice results from this decreased temperature and the process continues. At higher temperatures, the areas of snow and ice are likely to be reduced, thus reducing the albedo and leading to further enhancement of temperatures [42].

Positive feedback also occurs when water vapor changes in the atmosphere occur. For example, a warming which produces more evaporation produces more water in the atmosphere. But water vapor is a highly effective greenhouse gas which traps outgoing longwave radiation [85]. The dominant greenhouse gas in the Earth's atmosphere is water vapor, although carbon dioxide and trace gases, such as methane and chlorofluorocarbons are becoming increasingly important. The additional greenhouse effect of the extra water vapor enhances the temperature increase. Similarly, if temperature falls, there will be less water vapor in the atmosphere and the greenhouse effect is reduced [42].

Cloud feedback is more complex and exhibits both positive and negative characteristics [85]. Clouds are both highly reflective (thus contributing to the albedo) and composed of water and water vapor (thus contributing to the greenhouse effect, because of their control of the longwave radiation). Generally, the albedo effect dominates over the greenhouse effect for low and middle level clouds and so that increased cloudiness results in an overall cooling. On the other hand, cirrus clouds which are fairly transparent at visible wavelengths have a smaller impact upon the albedo so that their overall effect is to warm the system by enhancing the greenhouse effect [42].

2.2.5 Climate Records

2.2.5.1 Techniques for Reconstructing Past Climates

There are two major techniques that are used to reconstruct former climates. These include the use of meteorological instruments (thermometer, barometer etc.) that measure the weather relatively *directly* and the application of methods that estimate the weather or climate *indirectly*, i.e. using documentary sources or environmental sources (tree rings, ice cores, sea and lake sediments etc.) [85].

The most satisfactory means of comparing past with the present climate is by

using instrument exposed under standard conditions. However, problems with the quality of the early instruments and with the manner in which they were deployed often rendered their results unreliable [85].

Long before instrumentation was available, individuals made written comments about the weather in diaries and journals [85]. These data are particularly important as they deal with short term climatic fluctuations during the most recent past. It should be noted that the use of historical documents to reconstruct past climates is intimately linked with the debate over the extent to which climate and climatic fluctuations have played role in human history. The historical climatologist is often faced with the difficulty of ascertaining exactly what qualitative description from the past are equivalent to in terms of modern-day observations. For example, it is not always clear what the terms ‘drought’, ‘frost’, or ‘frozen over’ mean or how the qualifying terms like ‘extreme’ frost can be interpreted. An approach to solving this problem has been to use content analysis to assess in quantitative terms and as rigorously as possible, climatic information in the historical source. Historical sources rarely give a complete picture of former climatic conditions. Commonly, they are discontinuous observations and are very biased towards the recording of extreme events. As with all proxy data, historical observations need to be calibrated in some way in order to make comparison with recent data possible. This is commonly done by utilizing early instrumental data that may overlap with the proxy record to develop an equation relating the two data sets [91].

The climatic conditions can also be inferred from measurements of natural phenomena. However, without an ability to date the material concerned, it is impossible to construct a chronology or calibrate a record [85]. Dating methods fall in to four basic categories: (i) radioisotopic methods, which are based on the rate of atomic disintegration in a sample or its surrounding environment; (ii) paleomagnetic (correlation) methods, which rely on past reversals of the Earth’s magnetic field and their effects on a sample; (iii) organic and inorganic chemical methods, which are based on time-dependent chemical changes in the sample, or chemical characteristics of a sample; and (iv) biological method, which are based on the growth of an organism to date the substrate on which it is found [91]. Natural proxies for climate also exist whereby past climates can be inferred from tree ring thicknesses, pollen

deposits, beetle remains or the oxygen in ice or the sediments. The oxygen isotopic composition from ice cores or shells in oceanic sediments shows strong correlations with global temperature and has enabled the temperature changes of the past two million years to be reconstructed [85].

2.2.5.1.1 Longer-term Climate Change: Ice Age

Much of the knowledge about how the climate can change has been built on the study of the huge changes that occurred during the last ice ages. Although those may seem remote events, they are important messages for the present [89].

Ocean and ice core records show that from 2.5 million years ago till about 10,000 years ago, the earth has been in an ice age. In this period, the temperature changes of up to a maximum of 16°C between alternating hot and cold periods within the ice age event have been recorded. Figure 2.11 shows the temperature and carbon dioxide concentration fluctuations over Antarctica during the last 400,000 years over the Earth history. As can be seen in this figure, there are four main glacial cycles of the Earth cooling (ice advance) and warming (warm interglacial (between glacial) retreats). Each glacial cycle, lasting about 100,000 years, is asymmetrical in the shape with a long period of cooling followed by a much shorter warming event. During the last glacial maximum which occurred about 18,000 years ago, the average surface temperature of the planet fell by about 8°C compared with today and large ice sheets spread out from the poles over both hemispheres, but especially over the northern hemisphere where there is a greater landmass extent. These glacial cycles can be explained by two broad categories of factors; (i) external forcing factors such as changes in the amount/distribution of sunlight falling on the Earth; and (ii) internal forcing factors such as ocean currents, CO₂ levels, ice extent, that are part of the natural climate system [85].

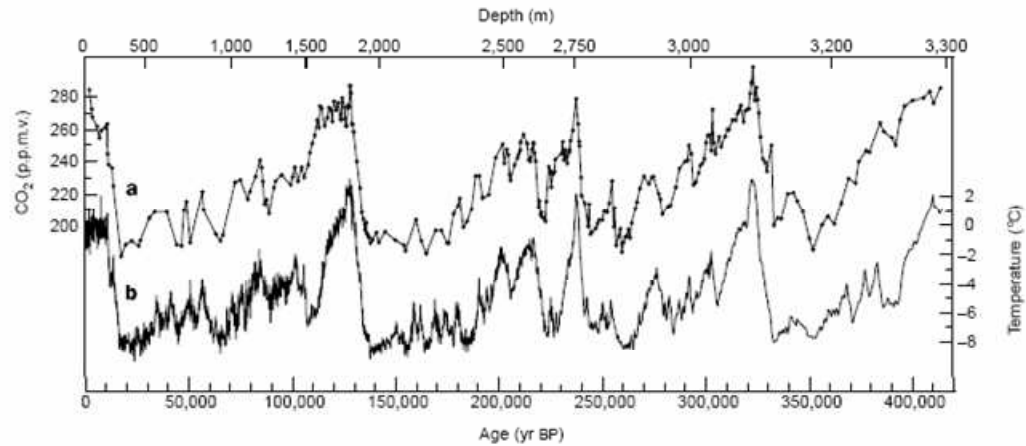


Figure 2.11 Ice core records of (a) CO₂ levels and (b) temperature from Antarctica (Vostok) over the last 400,000 years (i.e. four glacial-interglacial cycles). (Source: Adapted from Petit et al. [94]).

External variations in the amount of sunlight received by the Earth can result directly from changes in the sun's radiation output or more indirectly from changes in the orbital characteristics of the Earth in relation to the sun. Milankovitch theory involving Earth orbital variation around the sun can explain about 60 % of temperature variations during an ice age. The effect of Earth orbital variation (eccentricity with 100,000 year cycle, obliquity (axial tilt) with 41,000 year cycle and precession with 23,000 year cycle) on the temperature is illustrated in Figure 2.12. As can be seen from the figure, the three factors act positively to increase or decrease the amount of insolation to produce a warm or cold phase. However, Milankovitch theory can not explain the existence or the detailed temperature variations of an ice age and has been subject to criticism for these reasons. It is believed that there were certain environmental prerequisites before ice age began. These include (i) continental drift resulting in landmass effects and limited warm ocean circulation across both polar regions, (ii) tectonic activity (tectonic uplift) causing more extensive highland zones with colder climates, and (iii) enhanced geochemical weathering resulting in low global atmospheric CO₂ concentrations [85].

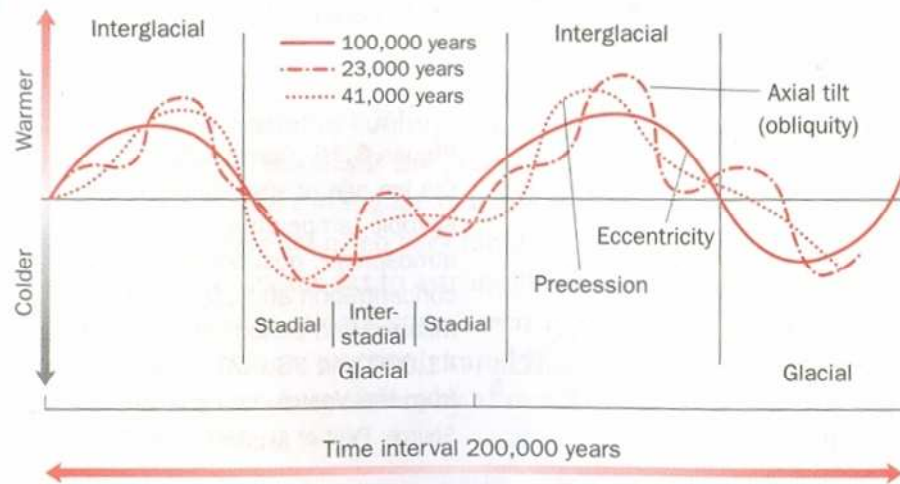


Figure 2.12 Possible combined effect of the Milankovitch orbital cycles on ice age temperatures [85]

Tectonic uplift episodes can change the climate by: (i) raising regions above the regional snowline/glaciation limit allowing glaciation to be initiated; (ii) modifying global and regional atmospheric circulation patterns; and (iii) increasing the rates of chemical (and physical) weathering in the elevated areas encouraging the sequestration of CO_2 from the atmosphere [85].

Atmospheric carbon dioxide concentrations can be determined by various geochemical processes such as the physical and chemical weathering of rocks that are rich in silicate minerals, outgassing of CO_2 and other gases from volcanic activity, and biological productivity involving the burial of organic plant and animal remains in sediments. Chemical weathering processes help to reduce CO_2 levels in the atmosphere. Rain removes CO_2 from the air as dilute carbonic acid. At the surface, this acid combines with silicate minerals to convert the CO_2 to bicarbonate. These bicarbonates are then dissolved in water and carried to the oceans where they are incorporated into shells of living creatures. Carbon dioxide is returned to the atmosphere by tectonic activity. Great temperatures and pressures deep in the Earth's moving crust compress, buckle and melt the sedimentary layers, releasing CO_2 . The

CO₂ outgassed back to the atmosphere at mid-ocean ridges and volcanoes. Normally, during warmer wetter geological periods more chemical weathering occurs, with more CO₂ being lost from the atmosphere to the sedimentary rocks. This loss of CO₂ has a regulatory cooling effect on the Earth-atmosphere system. During cooler geological periods, less chemical weathering produces a net return of CO₂ to the air, thus raising global temperatures. The strong correlation between levels of atmospheric CO₂ and ambient temperatures during the last four main glacier cycles can be also seen in Figure 2.11. However, there is still uncertainty about precise cause and effect mechanisms of this relationship. It is still not clear which event comes first: do ambient temperatures change first to be followed and reinforced by altered CO₂ concentrations, or do CO₂ levels change first, helping to drive the temperature [85].

The terrestrial biosphere stores more carbon during interglacial periods than during glacial periods. Therefore, the terrestrial biosphere is unlikely to be the source or cause of differences in atmospheric CO₂ between glacial and interglacial periods. The cause must lie therefore in the ocean. Two main hypotheses are used to explain glacial-interglacial variations in the atmospheric CO₂. These are (i) dissolution and outgassing of CO₂ in the ocean, (ii) nutrient enrichment of marine ecosystems in high latitudes [85].

2.2.5.1.2 Historical Climate Change

Historical documentary records are invaluable sources of proxy data but are notably important owing to dealing with short-term climatic fluctuations during the most recent years. The sources of the historical paleoclimatic information are ancient inscriptions, annals, chronicles, governmental records, private estate records, maritime and commercial records, personal papers and scientific or protoscientific writings. Bradley [91] quote Bell [95] and Henfling and Pflaumbaum [96] that the longest records come from Egypt, where stone inscriptions relating to the Nile flood levels are available from about 5000 years B.P. indicating higher rainfall amounts from East African summer monsoons at that time. The documents described the climate fluctuation related with in terms of drought, frost, frozen so that is difficult to compare qualitative description from the past with present observations. To perform

the statistical analyses on the documentary data, numerical values are given the range of the descriptive terms that were used in the document such as “severe frost”, “devastating frost” and “mild frost” [91].

The regional synthesis of paleoclimatic conditions for East Asia and Europe can be made from historical data by the large number of studies. In East Asia, the documentary data from China, Korea and Japan are important sources of information about past weather events. In China, the data has been obtained from the lower Yangtze River basin and regions to north. Temperature anomalies evaluated from historical data in East China and North China are illustrated in Figure 2.13. The coldest period in the last 600 years were in mid- to late seventeenth century and in the early to mid-nineteenth century. The temperature reached the highest level of the last 500 years in the period 1920-1940 [91].

Evidence for significant changes in the climate of Europe over the last few centuries is abundant. In Europe, the climate information is based on the writings from Romans times. In the last millennium BC, climates in the eastern Mediterranean is estimated colder and moister than today. By the first century, the climate warmed but after AD 400 it slowly returns to cooler conditions in much of Europe. From AD 900 to 1200, warmer condition was occurred in northern Europe which is known as the Medieval Warm Period. The climatic condition was cold from around 1510-1850 in the northern hemisphere, although the starting point of this period is not clear by the scientists. This time interval is known as Little Ice Age. The main factors causing climate change are explosive volcanic eruption and solar variability until 1850 [91].

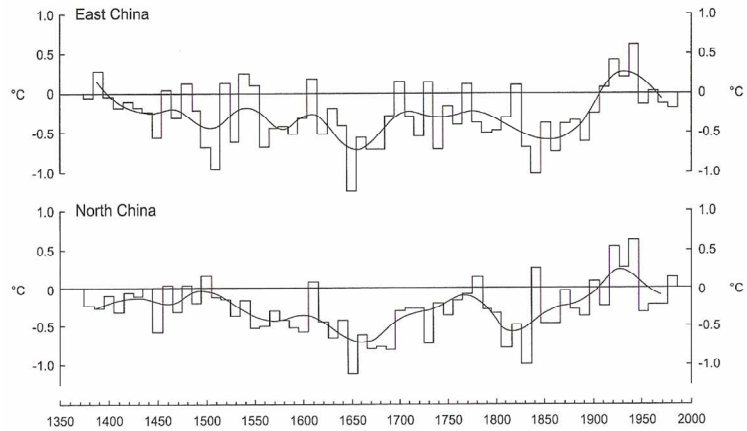


Figure 2.13 Ten-year mean annual temperature departures (from 1880-1979 means) based on historical documents from East China (above) and North China (below) [91]

2.2.5.1.3 Contemporary Trends in Assessment of Global Temperature

According to last IPCC report (AR4) [1], the linear warming trend over the last 50 years (0.13°C [0.10°C to 0.16°C] per decade) is nearly twice that for the last 100 years. The total global temperature increase from 1850–1899 to 2001–2005 is 0.76°C [0.57°C to 0.95°C]. In IPCC reports, the global mean temperature is defined as the global surface temperature which is an estimate of the global mean surface air temperature. However, for changes over time, only anomalies, as departures from the area-weighted global average of the sea surface temperature and land surface air temperature, are used. The sea surface temperature is the temperature of the subsurface bulk temperature in the top few meters of the ocean, measured by ships, buoys and drifters. From ships, measurements of water samples in buckets were mostly switched in the 1940s to samples from engine intake water. Satellite measurements of skin temperature (uppermost layer; a fraction of a millimeter thick) in the infrared or the top centimeter or so in the microwave are also used, but must be adjusted to be compatible with the bulk temperature. The surface air temperature is measured in well-ventilated screens over land at 1.5 m above the ground [1]. Figure

2.14 shows the global sea surface temperature, global marine air temperature and land surface temperature change from the 1850s by using meteorological instrumentals. As can be seen from the figure, global sea surface temperature and land surface temperature have been increasing since 1860 and also land surface temperature change is higher than the sea temperature over the last ten years. However, researches debate about the accuracy of calculations of the global surface temperature and also the reasons of the global surface temperature change.

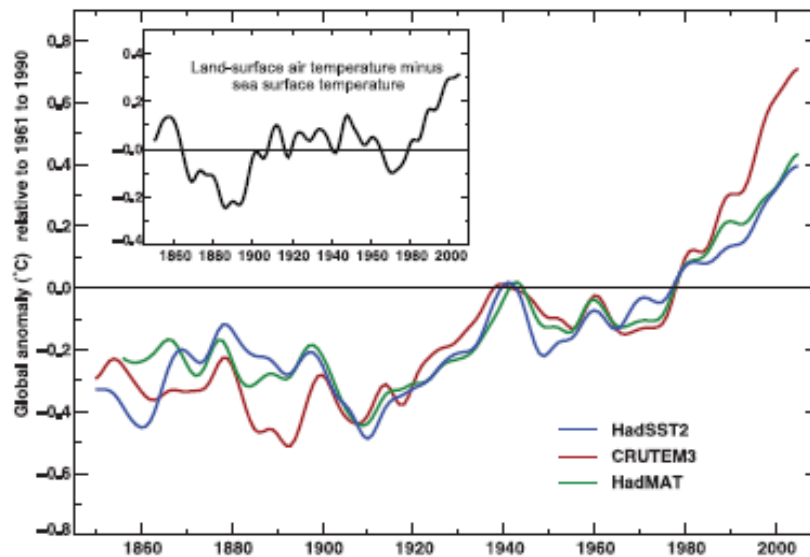


Figure 2.14 Annual anomalies ($^{\circ}\text{C}$) of global average SST (blue curve), NMAT (green curve) and land-surface air temperature (red curve), relative to their 1961 to 1990 means. The smooth curves show decadal variations. Inset shows the smoothed differences between the land-surface air temperature and SST anomalies [1]

2.2.5.1.3.1 Problems of the Calculation of Global Surface Temperature

Essex et al. [97] stated that physical, mathematical and observational grounds are employed to show that there is no physically meaningful global temperature for

the Earth in the context of the issue of global warming. While that statistic is nothing more than an average over temperatures, it is regarded as the temperature, as if an average over temperatures is actually a temperature itself, and as if the out-of-equilibrium climate system has only one temperature. But an average of temperature data sampled from a non-equilibrium field is not a temperature. Moreover, it hardly needs stating that the Earth does not have just one temperature. It is not in global thermodynamic equilibrium-neither within itself nor with its surroundings. Also temperature is an intensive variable. Intensive variables are independent of system size and represent a quality of the system. In this case combining two systems will not yield an overall intensive quantity equal to the sum of its components. For example two identical subsystems do not have a total temperature or pressure twice those of its components. A sum over intensive variables carries no physical meaning. Dividing meaningless totals by the number of components cannot reverse this outcome. In special circumstances averaging might approximate the equilibrium temperature after mixing, but this is irrelevant to the analysis of an out-of-equilibrium case like Earth's climate [97].

When it is considered that the global surface temperature can be calculated, there are some problems such as instrumental error, uncertainties, urbanization effect and analysis error.

The observed data include instrumental errors. Freitas [98] stated that The IPCC temperature record for the globe is based on thermometers on the ground, usually on the land and in growing urban areas; a system which is not accurate enough to detect changes as small as 0.1°C . Since 1979 temperature measurements of lower troposphere have been made by satellite and the accuracy of the radiometer measurements is 0.1°C which is considerably better than the accuracy of thermometer measurements made on the surface of the Earth [98]. Moreover, Lindzen [99] said that the determination of the globally averaged temperature of the Earth's surface is difficult task. It is commonly known that temperature can vary markedly over short distances; urban areas are frequently warmer than the countryside; water surfaces differ in the temperature from adjacent land surfaces; temperatures vary in the course of a day, and certainly day to day; and seasonal changes are large. Moreover, there is what is called "natural" climate variability from

year to year; because it is expected to occur even in the absence of external causes. It is not clear that network of surface-temperature measurements is adequate to completely eliminate these sources of uncertainty. However, such averages as we are able to form actually show remarkable constancy from year to year. Estimated changes over the last 150 years are less than 1°C. We can not be at all sure that these small changes are not, in significant measure, due to inadequate and/or improper sampling [99].

The other problem of calculation of global surface temperature is urbanization. Until recently, measurements of global air temperature change were based entirely on measurements taken on the ground. Modification of the surface by human activity can have a significant effect on climate near the ground. The best-document example is the ‘urban heat island’ effect, in which data from urban stations can be influenced by localized warming due to asphalt and concrete replacing grass and trees. This can account for an urban area being as much as 14°C warmer than its rural surroundings [98]. Moreover, Khandekar et al. [100] stated that for large cities, the urban heat island effect has been shown to be as high as 10°C (temperature difference between the city center and remote suburban location) in the studies by Oke [101] and others. However, in IPCC report, it is stated that urban heat island effects are real but local, and have a negligible influence (less than 0.006°C per decade over land and zero over the oceans) on these values [1]. And also, Khandekar et al. [100] stated that several recent studies have taken a closer look at the land-use change impact on mean temperature calculations and these and other studies strongly suggest the impact to be significantly more than the value 0.06°C per hundred years used by IPCC TAR [2]. Therefore, it can be said that the impact of urbanization and land-use change on the mean temperature calculation appears considerably more significant than that which has been assumed to date [100].

There are some analysis errors of calculation of global surface temperature. The example of the analysis error can be seen in the temperature anomaly at the lower troposphere. Figure 2.15 shows the global tropospheric temperatures measured from weather balloon and orbiting satellite between 1979 and 1996. As can be seen from the figure, the trends are slightly downward since 1979 [102]. However, Räisänen [103] said that new sources of error have been found from satellite and

radiosonde records used to estimate the temperature trends in the lower troposphere [104]. It now appears likely that the free troposphere has been warming at approximately the same rate as the surface since 1979, where as radiosonde records suggest a slightly larger warming in the lower troposphere than at the surface since 1958 [103]. In IPCC report [1], it is explained that new analyses of balloon-borne and satellite measurements of lower- and mid-tropospheric temperature show warming rates that are similar to those of the surface temperature record (Figure 2.16) and are consistent within their respective uncertainties, largely reconciling a discrepancy noted in the TAR [2].

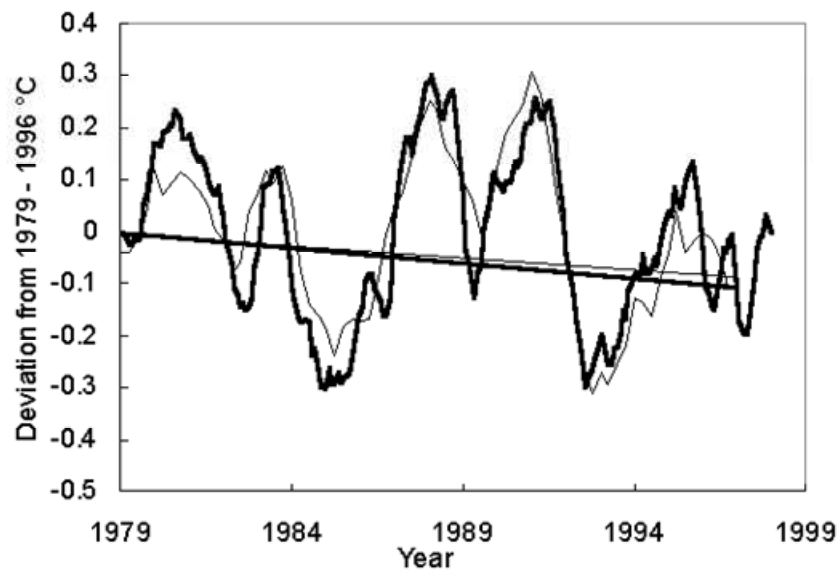


Figure 2.15 Global radiosonde balloon temperature (measurements of global lower tropospheric temperature at 63 stations between latitudes 90 N and 90 S) (light line) and global satellite MSU temperature (dark line) with 6-month smoothing. Both sets of data are graphed as deviations from their respective means for 1979 to 1996. The 1979 to 1996 slopes of the trend lines are minus 0.060°C per decade for balloon and minus 0.045°C for satellite [102]

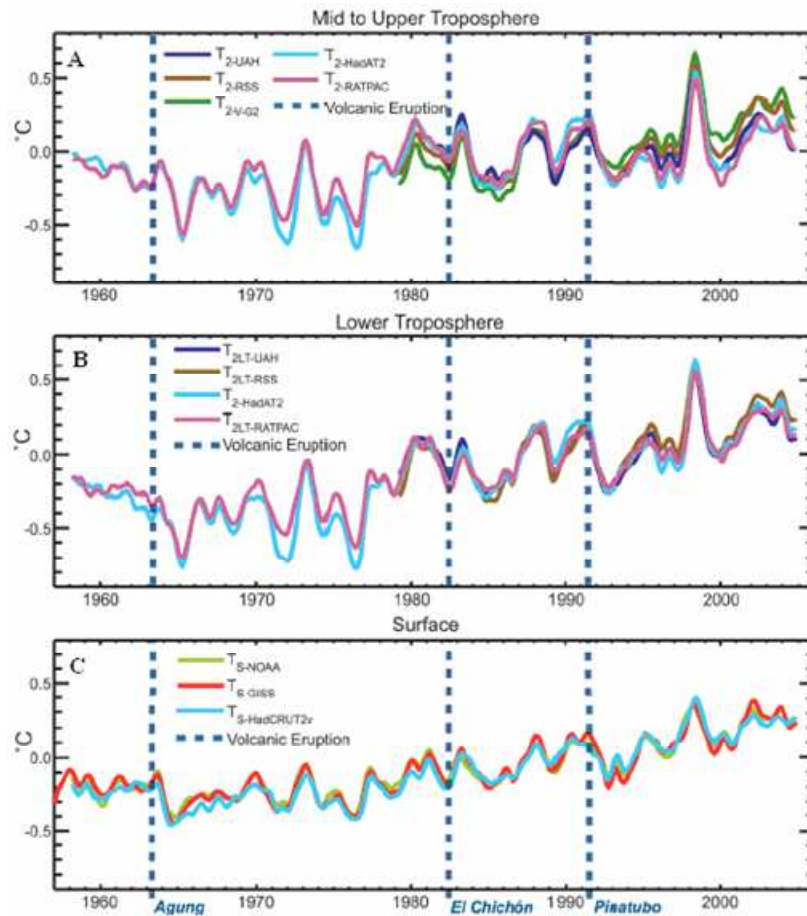


Figure 2.16 Observed surface and upper-air temperature anomalies ($^{\circ}\text{C}$). (A) Tropospheric T_2 (channel 2), (B) Lower tropospheric T_{2LT} , from UAH, RSS and VG2 MSU satellite analyses and UKMO HadAT2 and NOAA RATPAC radiosonde observations; and (C) Surface records from NOAA, NASA/GISS and UKMO/CRU (HadCRUT2v). All time series are monthly mean anomalies relative to the period 1979 to 1997 smoothed with a seven month running mean filter. Major volcanic eruptions are indicated by vertical blue dashed lines. T_{2LT} : lower troposphere , T_2 : MSU channel 2, T_{2-UHA} : MSU channels 2 conducted by the University of Alabama in Huntsville, T_{2-RSS} : MSU channels 2 conducted by Analyses of and by Remote Sensing Systems, T_{2-V-G2} : MSU channels 2, **HadAT2**: HadAT2 (Hadley Centre Atmospheric Temperature Data Set Version 2, **RATPAC**: Radiosonde Atmospheric Temperature Products for Assessing Climate; RATPAC, **NOAA**: National Oceanic and Atmospheric Administration, **NASA/GISS**: National Aeronautics and Space Administration's (NASA) Goddard Institute for Space Studies (GISS), **UKMO/CRU (HadCRUT2v)**: Climatic Research Unit CRU with the United Kingdom Meteorological Office (UKMO) Hadley Centre in the UK [1]

Another study of the analysis error of calculation of global temperature is about the proxies' data analysis. McIntyre and McKittrick [105] showed that the data set of proxies of past climate used in Mann et al. [106] for the estimation of temperatures from 1400 to 1980 contains collation errors, unjustifiable truncation or extrapolation of source data, obsolete data, geographical location errors, incorrect calculation of principal components and other quality control defects. They [105] detailed these errors and defects and then applied Mann et al. [106] methodology to the construction of a northern hemisphere average temperature index for the 1400-1980 period, using corrected and updated source data. The temperature profile obtained by two studies can be seen in Figure 2.17. The major finding was that the values in the early 15th century exceed any values in the 20th century [105]. In IPCC report, this was reported to be due to the fact that McIntyre and McKittrick [105] reported that they were unable to replicate the results of Mann et al.. Wahl and Ammann [107] showed that this was a consequence of differences in the way McIntyre and McKittrick [105] had implemented the method of Mann et al. [106] and that the original reconstruction could be closely duplicated using the original proxy data [1].

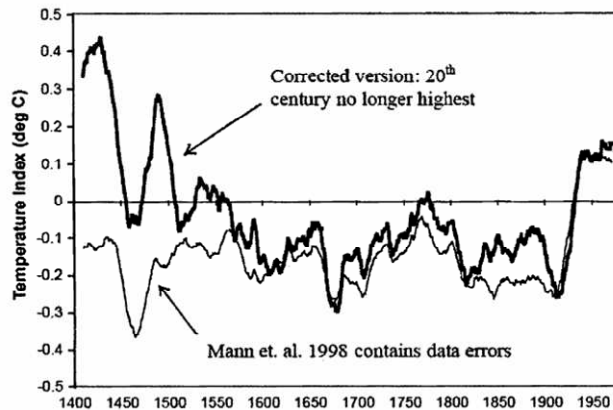


Figure 2.17 Temperature change (with respect to present mean temperature) over the last six centuries by Mann et al. [106] (thin line) and as recalculated by McIntyre and McKittrick (thick line) [105]

2.2.5.1.3.2 The Reasons of the Global Surface Temperature Change

Earth's temperature does not change monotonically. It rises and falls in highly irregular cycles and the amplitude of changes is highly variable [100]. Researches debate about the reasons of the global surface temperature change. Generally, some scientists have explained that this variation can be due to solar activity, changes in the equator-to-pole temperature difference or the increasing atmospheric carbon dioxide concentration.

Solar Activity

The sun is the source of the energy that causes the motion of the atmosphere and thereby controls weather and climate. Any change in the energy from the sun received at the surface of Earth will therefore affect the climate [108]. The effect of the sun on the Earth system can be seen in Figure 2.18.

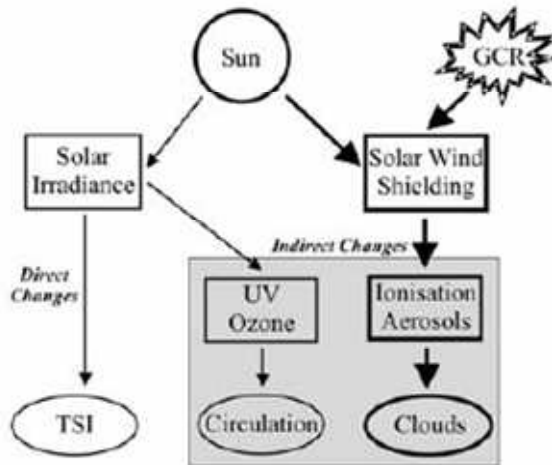


Figure 2.18 Possible routes for a solar influence on climate. TSI: Total solar irradiance and GRC: Galactic cosmic ray [109]

The variation in the total solar (wavelength-integrated) irradiance (TSI) directly produces a terrestrial temperature response regionally or globally, or both, on time scales of years to centuries [110]. Stott et al. [111] stated that satellite measurement of solar irradiance have only been made since 1978 and show a clear 11-year cycle with variations in total irradiance of approximately $\sim 0.1\%$. Currently this is believed to be too small to significantly influence observed surface temperatures directly, although this may have been larger back in time [112]. Figure 2.19 shows the relation between solar irradiance, geomagnetic field and global temperature change. As can be seen from the figure, between 1900 and 1980, the tendency of solar irradiance and geomagnetic field at the Eskdalemuir (ESK) and Sitka (SIT) observatories are the same as the global temperature change, but since 1980s, solar irradiance and geomagnetic field drop where as global mean temperature arises [113].

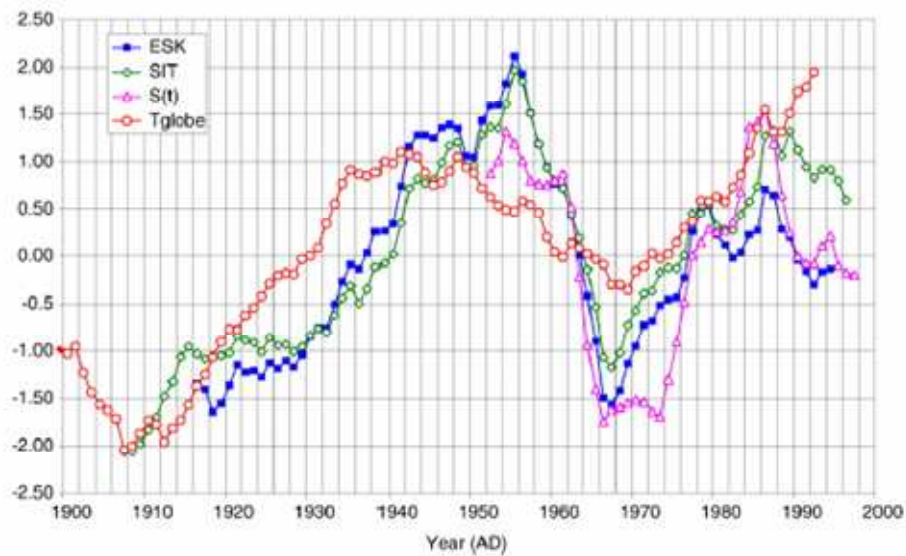


Figure 2.19 Time evolution over the 20th century of the eleven-year running averages of magnetic indices based on modulus of the geomagnetic field at the Eskdalemuir and Sitka observatories (ESK and SIT) compared to solar irradiance (S(t)) and global mean temperature (T_{globe}) [113]

Variations in solar activity can be used to understand the effect of sun on the Earth's climate. Solar activity can not be characterized by a simple number. Different solar activity parameters (i.e. solar cycle) show different solar cycle variations and different long term trends. Therefore it is not surprising that studies dealing with different climate and solar activity parameters do not always agree [108]. Friis-Christensen [114] compared the length of the solar cycle with the Northern Hemisphere land air temperature anomalies. The length of the sunspot cycle is known to vary with solar activity so that high activity implies short solar cycles whereas long solar cycles are characteristic for low activity levels of the sun [114]. The relationship between the length of the solar cycles and the temperature anomaly can be seen in Figure 2.20. As can be seen from the figure, the variation of the solar cycle length closely matches the long-term variations of the Northern Hemisphere land air temperature during the period from 1860 to 1990 [114]. Moreover, Khilyuk and Chilingars [115] claimed that the greater the solar activity, the greater the sun's radiation and, consequently the Earth's surface absorbs more radiation from the sun; and this leads to an increase in the surface temperature and a consequent warming of the atmosphere by convection, water vapor condensation, and radiation.

Laut [116], however, claimed that the strong relationship between solar activity and climate displayed in Figure 2.20 were obtained by incorrect handling of the physical data and illustrated that the last 4 points in the smoothed solar cycle curve in Figure 2.20 ha not been filtered like the first 20 points from the curve. His revised calculations demonstrated that the last 4 points is a flat curve (Figure 2.21) not a curve with increasing tendency as shown in Figure 2.20.

A change in solar ultraviolet irradiance indirectly affects on the Earth's atmosphere (seen in Figure 2.19). This part of the solar irradiance spectrum is mostly absorbed in the Earth's stratosphere, resulting in stratospheric heating which influence temperature and circulation of the stratosphere. Hence, variations of the mean tropospheric temperature must include stratosphere–troposphere interaction. A detailed mechanism effectively transferring stratospheric heating into the troposphere is yet not clear [109, 117]. The UV region of the solar radiation spectrum is observed to vary by up to 10 %, although satellite measurements of total solar radiation over the past 20 years have revealed that the total radiative output of the sun varies by 0.1

% over a solar cycle (approx. 11 years) [112].

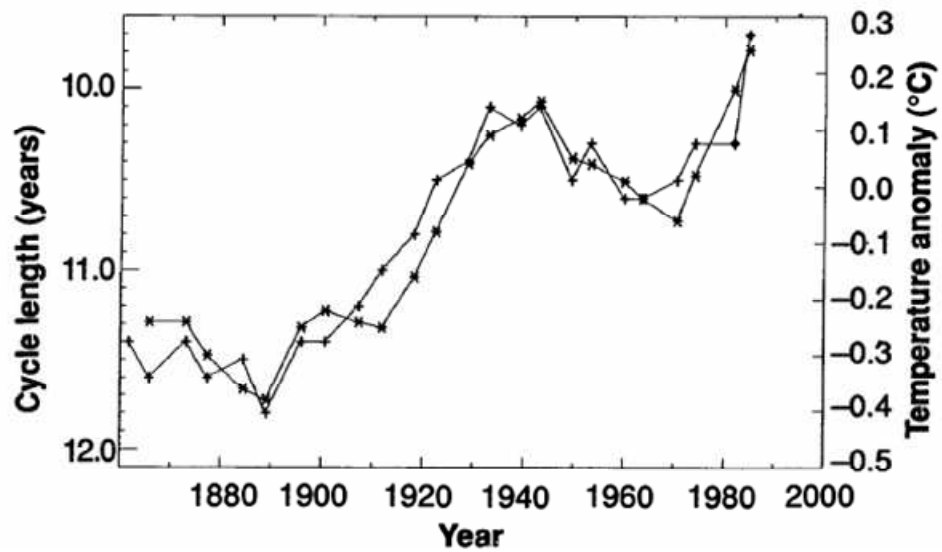


Figure 2.20 Variation of the sunspot cycle length (left-hand scale) determined as the difference between the actual smoothed sunspot extremum and the previous one. The cycle length is plotted at the central time of the actual cycle (+). The unsmoothed last values of the time series have been indicated with different symbol (*) which represents the Northern Hemisphere temperature anomalies [114]

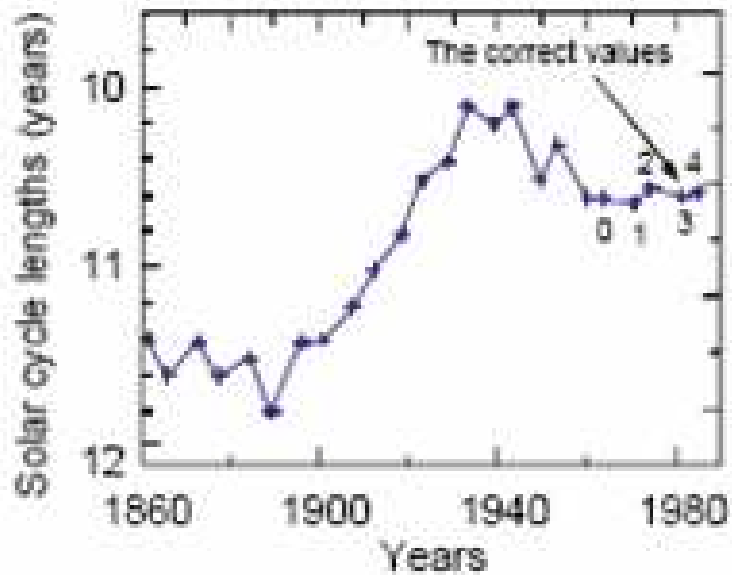


Figure 2.21 An update of the original solar curve in Figure 2.20 with points 1–4 calculated applying correct arithmetic to the observed and predicted data used by Thejll and Lassen [118], [116]

Another indirect effect of the Sun on the Earth’s climate is the solar wind shielding Galactic Cosmic Rays (GCR) which is illustrated in Figure 2.19 [109]. Solar wind is known as energetic particles emitted by the solar surface [112]. Although the energy in the solar wind is negligible compared to the energy in the ultraviolet and visible spectral bands, the relative variations are considerable. Mazzarella [119] investigated the long term geomagnetic forcing of global air temperature through the turbulence of the solar wind, the Earth’s rotation and atmospheric circulation. He concluded that if the solar corpuscular activity behaves in the same way in the future as it has in the past, its 60-year cycle might suggest a forecast estimate for a gradual cooling of the Earth’s atmosphere up to around 2030 [119].

One of the effects of the varying solar wind is the modulation of the galactic cosmic ray flux [108]. Cosmic rays consist mainly of protons (90 %) and of alpha-

particles (9 %) plus a smaller amount of heavier elements [120]. The cosmic ray intensity shows the well-known inverse relationship to the sunspot cycle. This is caused by the interplanetary medium which has a larger shielding effect on the cosmic rays during high solar activity [120]. The cloud formation is related to the variation of the cosmic ray fluxes [109, 120]. However, there is at present no detailed understanding of microphysical mechanism of this relationship [120]. As solar activity decreases, incoming cosmic rays to the Earth increases and this leads to increase ionization of the troposphere and alters its physical properties so that it affects cloud formation [117]. Cloud properties are potentially important for Earth's radiation budget, but sign and magnitude will be determined by cloud types affected [112]. An increase of clouds at low altitude clouds will result in cooling, whereas an increase of high altitude clouds will warm the planet.

In order to understand the relation between the cloud formation and cosmic rays, satellite data taken during different periods of time and normalized cosmic rays fluxes were plotted against time [120]. As can be seen in Figure 2.22, the variation of cloud data is the same as the change in the cosmic flux from 1980 to 1995. Moreover, Svensmark [121] compared the cloud data with variations in GCR flux and the 10.7 cm radio flux from the sun and found that Earth's cloud cover underwent a modulation more closely in phase with the galactic cosmic ray flux than with other solar activity parameters from 1980 to 1995. However, some scientists are against this correlation as illustrated in Figure 2.23 [116]. This figure is a corrected and updated version of Figure 2.22. The correction consists in removing the irrelevant DMSP data, and the update consists in adding data for total cloud cover presented on <http://isccp.giss.nasa.gov/climanal1.html> (ISCCP D2 data for period 1983-1999, smoothed applying a bandwidth similar to Figure 2.22) together with galactic cosmic ray intensity as observed at station Climax in Colorado. It shows that the two parameters agree fairly well from 1985 to 1989 but disagree strongly thereafter [116].

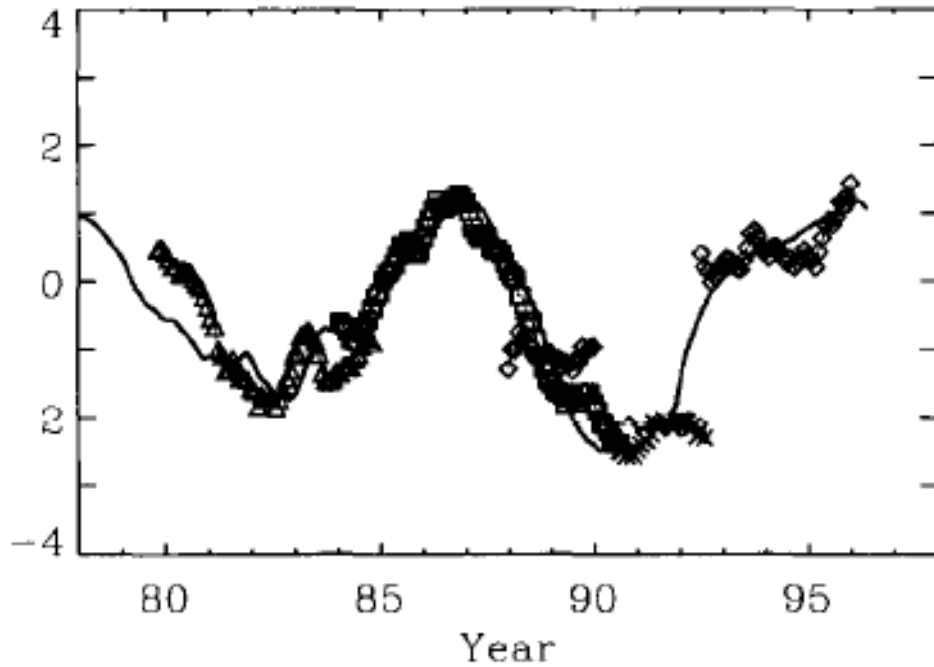


Figure 2.22 Composite figure showing four satellite cloud data sets and normalized cosmic rays fluxes from Climax (thick curve). Triangles are the Nimbus-7 data, squares are the ISCCP-C2 data, diamonds are the DMSP data, and crosses are the ISCCP-D2 data. The panel displays the data smoothed using a 12 months running mean, The Nimbus-7 and the DMSP data are total cloud cover for the Southern Hemisphere over oceans, and the ISCCP data have been derived from the geostationary satellites over oceans with the tropics excluded [121]

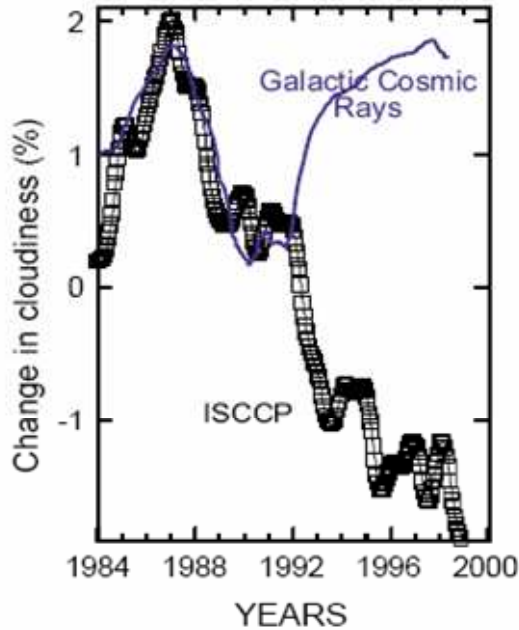


Figure 2.23 Squares denote ISCCP data and the blue solid curve shows galactic cosmic ray intensities as measured at Climax, Colorado, and smoothed as in Kristjánsson and Kristiansen [122]. The update consists in adding new ISCCP data as available from <http://isccp.giss.nasa.gov/climanal1.html> [116]

Changes in the Equator-To-Pole Temperature Difference

Major climate changes in the past have been characterized by large changes in the equator-to-pole temperature difference (ranging from about 19°C to 60°C; the present annually averaged value is about 40°C), and relatively constant equatorial temperatures (with about 2°C of the present). Changes in the mean temperature of the Earth appear to have been a by-product of these changes rather than cause. The cause(s) for the near constancy of equatorial temperatures constitutes an additional major question. The stability of equatorial temperature is particularly remarkable when one considers that the changes in heat flux out of the tropics implicit in the changes in equator-to-pole temperature difference are likely to have been far larger than any proposed external radiative forcing. Indeed, given the stability of the tropics, it is hard to see how gross external radiative forcing, which

does not affect meridional heat fluxes in any evident way, can substantially alter the mean temperature of the Earth [52].

Increasing Atmospheric Carbon Dioxide Concentration

Some scientists believe that the global temperature anomaly in the last centuries is caused by increasing the concentration of greenhouse gases, mainly carbon dioxide, in the atmosphere. Because more CO₂ in the atmosphere will trap more outgoing longwave radiation and thus the Earth's surface will eventually become warmer [100]. The carbon dioxide annual change is illustrated in Figure 2.24 and according to figure; over last 100 years the concentration of carbon dioxide rises and falls in large cycles over the years but its overall trend rises. The five-year means smooth out short-term perturbations associated with strong ENSO events in 1972, 1982, 1987 and 1997. Uncertainties in the five-year means are indicated by the difference between the red and lower black lines and are of order 0.15 ppm. The concentration of atmospheric CO₂ has increased from a pre-industrial value of about 280 ppm to 379 ppm in 2005. Emissions of CO₂ from fossil fuel use and from the effects of land use change on plant and soil carbon are the primary sources of increased atmospheric CO₂. Table 2.2 shows the global carbon budget and in the table, by convention, positive values are CO₂ fluxes (GtC yr⁻¹) into the atmosphere and negative values represent uptake from the atmosphere (i.e., 'CO₂ sinks'). Fossil CO₂ emissions for 2004 and 2005 are based on interim estimates. Due to the limited number of available studies, for the net land-to-atmosphere flux and its components, uncertainty ranges are given as 65 % confidence intervals and do not include interannual variability. NA indicates that data are not available [1].

The reason behind the increase in the atmospheric carbon dioxide levels was considered to be due to change in the solubility of CO₂ in the oceans with temperature [115]. When the temperature increases due to solar activity, the solubility of the carbon dioxide in the ocean water decreases, and, as per the Henry Law, part of the carbon dioxide of the ocean water is transferred into the atmosphere to restore a disturbed dynamic equilibrium between the carbon dioxide contents of the ocean water and the atmosphere. Contemporary oceanic water contains 50–60 times more carbon dioxide than atmospheric air. Because of the inverse dependence

of the CO₂ solubility in the ocean water on temperature, the increase in temperature will cause an increase in the atmospheric CO₂ concentration [115].

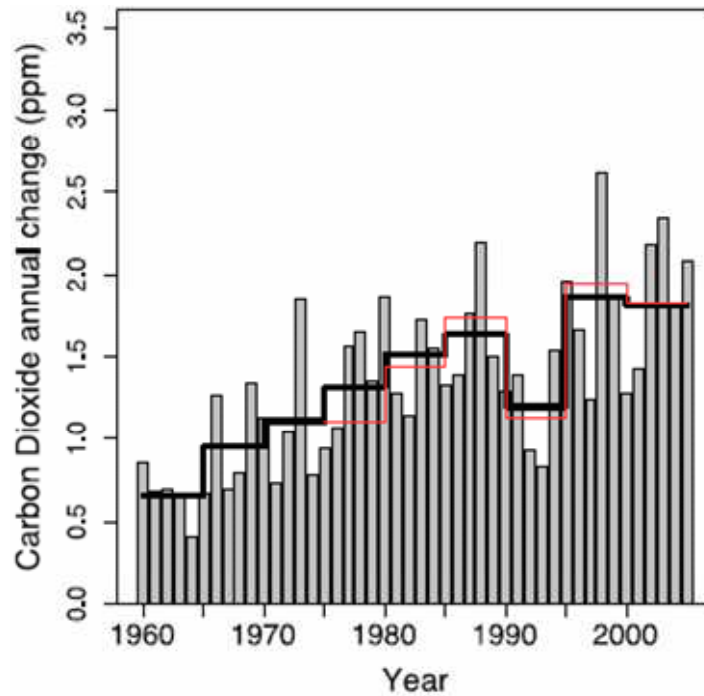


Figure 2.24 Annual changes in global mean CO₂ concentration (grey bars) and their five-year means from two different measurement networks (red and lower black stepped lines). The five-year means smooth out short-term perturbations associated with strong ENSO events in 1972, 1982, 1987 and 1997. Uncertainties in the five-year means are indicated by the difference between the red and lower black lines and are of order 0.15 ppm [1]

Table 2.2 Global carbon budget [1]

	1980s (GtC yr ⁻¹)	1990s (GtCyr ⁻¹)	2000-2005 (GtC yr ⁻¹)
Atmospheric increase	3.3± 0.1	3.2± 0.1	4.1±0.1
Fossil carbon dioxide emissions*	5.4± 0.3	6.4± 0.4	7.2± 0.3
Net ocean-to-atmosphere flux	-1.8± 0.8	-2.2± 0.4	-2.2± 0.5
Net land-to-atmosphere flux	-0.3± 0.9	-1.0± 0.6	-0.9± 0.6
Partitioned as follows			
Land use change flux	1.4 (0.4 to 2.3)	1.6 (0.5 to 2.7)	NA
Residual land sink	-1.7 (-3.4 to 0.2)	-2.6 (-4.4 to -0.9)	NA

*Fossil CO₂ emissions include those from the production, distribution and consumption of fossil fuels and from cement production. Emission of 1 GtC corresponds to 3.67 GtCO₂.

Another cause of increasing concentration of CO₂ is said to be the rate of outgassing determined by tectonic activity [123]. As a universal measure of the rate of global tectonic activity one can use the rate of heat flux through the Earth's surface, because its level indicates the magnitude of total energy generated in the mantle. Main gasses generated in the mantle and on the ocean floor are: carbon dioxide, methane, and hydrogen. Carbon dioxide dissolves mostly in the oceanic water and transforms to abiogenic methane (CH₄) and carbonate (2MgCO₃). These transformation reactions are accompanied by a very large amount of heat release. This heat contributes considerably to the heat flux through the Earth's surface. Thus, the rate of abiogenic CH₄ generation on the ocean floor in the spreading zones can be used as a measure of global tectonic activity. In turn, the rate of the Earth's tectonic activity can be used as a measure of the Earth's outgassing rate. CH₄ gas enters the atmosphere, contributing to the greenhouse effect and depleting ozone concentration by reacting with ozone and solar radiation and converted to carbon dioxide water vapor and hydrogen. Due to a high level of current tectonic activity, there is a pronounced increase in the current methane gas generation at the oceanic floor

according to Yasamanov [124]. $5 \cdot 10^{15}$ g/year of CH_4 are currently released to oceanic water at the spreading zones of mid-ocean ridges only. It is believed that the increasing concentration of methane leads to significant increase in the atmospheric carbon dioxide content that considerably amplifies the atmospheric greenhouse effect [123].

However, Robinson et al. [102] stated that so great are the magnitudes of ocean (surface, intermediate and deep) and land (vegetation, soils and detritus) reservoirs, the rates of exchange between them, and the uncertainties with which these numbers are estimated that the source of the recent rise in the atmospheric carbon dioxide has not been determined with certainty [102].

2.3 Climate Models

Climate models are used to represent the many process that produce climate [42]. Moreover, models provide forecast the future behavior of a climate system as a consequence of actual or hypothesized disturbances to the present status of the system. However, the level of skill of forecasts is ultimately constrained by understanding of system functioning [85]. Climate system is described in terms of basic physical, chemical and biological principle and a numerical model can be used to solve a series of equations expressing these laws. Due to complexity of climate system and not understanding completely, climate models must be a simplification of the real world. The important components of climate model are radiation, dynamics, surface process, chemistry and resolution in both time and space. Different types of climate model have been developed with varying levels of complexity. There are main types of model; energy balance models, one-dimensional models and global circulation model [42].

Energy balance models (EBMs) consider the surface temperature (strictly sea-level) as a function of the energy balance of the Earth [42]. The simplest are zero-dimensional energy balance of the Earth. These models include only incoming and outgoing energy flows to the globe and compute the resultant globally average annual temperature at the surface. Energy balance models are generally one-dimensional models which consider the earth in terms of energy exchanged latitudinally from one zone to the next by diffusive horizontal heat transfer. Although

one-dimensional energy balance models are simple, they have provided valuable insight into the role of horizontal heat transport feedbacks as well as the fragility of the equilibrium climate [85].

One dimensional models such as radiative-convective models and single column models focus on process in the vertical. Radiative-convective models compute the (usually global average) temperature profile by explicit modeling of radiative processes and a convection adjustment which re-establishes a predetermined lapse rate. Single column are single columns extracted from a three-dimensional model and include all the processes that would be modeled in the three-dimensional version but without any of horizontal energy transfer [42].

General circulation models (GCMs) represent the three-dimensional climate system using four primary equations describing the movement of energy and momentum, along with the conservation of mass and water vapor [85]. The first step in obtaining a solution is to specify the atmospheric and oceanic conditions at a number of grid points, obtained by dividing the Earth's surface into a series of rectangles, so that a traditionally regular grid results. Conditions are specified at each grid point for the surface and several layers in the atmosphere and ocean. The resulting set of coupled non-linear equations is then solved at each grid point using numerical techniques. Various techniques are available, but all use a timestep approach. Although GCMs closely approach the real atmospheric and oceanic situation, there are a number of practical and theoretical limitations at present such as long computational time and large storage capacities. Since the accuracy of the model partly depends on the spatial resolution of the grid points and the length of the timestep, a compromise must be made between the resolution desired, the length of integration and the computational facilities available. At present, atmospheric grids are typically spaced between 2° and 5° of latitude and longitude apart and timesteps of approximately 20-30 minutes are used. Vertical resolution is obtained by dividing the atmosphere into between six and fifty levels, with about twenty levels being typical[42].

CHAPTER 3

RADIATIVE-CONVECTIVE MODEL, RADIATION MODEL AND THEIR NUMERICAL SOLUTION TECHNIQUE

In this thesis study, a simple climate model, radiative-convective model, was developed to determine the interactions between the two most important components of the climate system, i.e., the hydrosphere and the atmosphere, by following the approach of Ramanathan et al. [125]. Since the atmospheric radiation is the key component of the developed model, the radiative transfer equation (RTE) had to be solved in conjunction with the time-dependent governing equations of the model and the solution methods had to be compatible. For this purpose, a previously developed radiation code based on Method of Lines (MOL) solution of Discrete Ordinates Method (DOM) with Wide Band Correlated-k (WBCK) was adapted and coupled with the radiative-convective model. The model was applied to 1-D clear sky atmosphere containing absorbing, emitting, non-scattering radiatively non gray medium.

In this chapter, the radiative-convective model together with the radiation model is described. This is followed by the description of numerical solution technique.

3.1 Radiative-Convective Model

Radiative-convective model is one of the simplest climate models. The model was applied to a system consisting of the hydrosphere and the atmosphere. The system is shown schematically in Figure 3.1. There are two layers in the ocean, ocean mixed layer and deeper ocean. The thickness of the ocean mixed layer is taken

as 50 m and it is assumed that the interaction between the ocean mixed layer and the deeper ocean is negligible. The ocean mixed layer exchanges energy with the atmosphere through the boundary layer whose thickness is taken to be 40 m. The atmosphere is approximated as a 1-D clear sky atmosphere containing absorbing-emitting, non-scattering radiatively nongray medium. The ocean and its atmosphere absorb the shortwave ($< 4 \mu\text{m}$) radiation coming from the sun and emit thermal longwave ($> 4 \mu\text{m}$) radiation to space. In the model, only longwave radiation is taken into consideration. It is assumed that there is no longwave radiation but only shortwave radiation incident on the top of the atmosphere and that shortwave radiation reaches the bottom boundary, i.e. the ocean surface without any change.

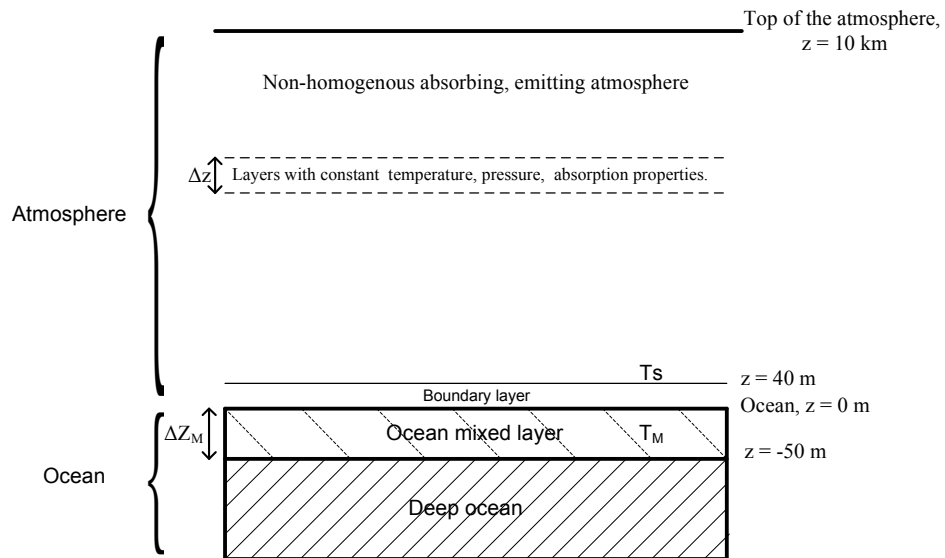


Figure 3.1 Schematic representation of the system under consideration

Since the water vapor concentration is nearly 0 ppm around 10 km above the ocean as shown in Figure 3.2, the atmosphere is defined as the region extending from the ocean to 10 km in altitude. Between 0 and 10 km, concentrations of participating gases are negligible compared to the concentrations of H₂O and CO₂. Therefore, it is assumed that the contribution to radiative transfer within this region arises only from H₂O and CO₂. As the water vapor concentration is influenced by condensation, its concentration varies with altitude as can be seen in Figure 3.3, where the concentration profile of water vapor for mid-latitude summer is illustrated. This profile is used as input data in the present study. The concentration of CO₂ is variable in the planetary boundary layer (around 100 m above the surface of the Earth), but at higher levels its mixing ratio is essentially constant. Therefore, in the model, CO₂ is assumed to be mixed uniformly within the atmosphere at a mixing ratio of 383 ppm which is reported to be the present average concentration according to NOAA (National Oceanic and Atmospheric Administration) Earth System Research Laboratory [93]. As temperature, pressure and concentration of water vapor changes in the atmosphere, the atmosphere is divided into several homogenous layers.

In the model, warming of the ocean mixed layer due to solar radiation is also taken into consideration. It is assumed that solar flux does not change throughout the atmosphere and the ocean absorbs all incoming solar energy. According to World Meteorological Organization [89], the Earth is bathed in an average solar influx of 1370 watts per square meter and only 51 % of the incoming solar energy is absorbed by the Earth's surface. Therefore, in the model, solar heat flux at the ocean mixed layer is taken as 698.7 W/m^2 during the day.

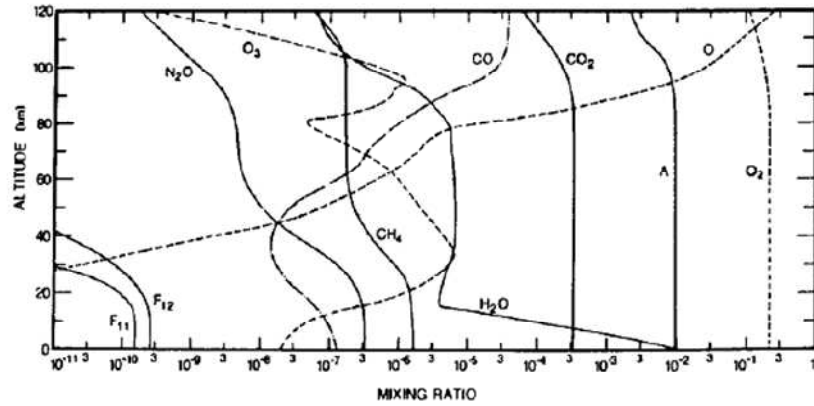


Figure 3.2 Vertical Profiles of mixing ratio of selected species at equinox [57]

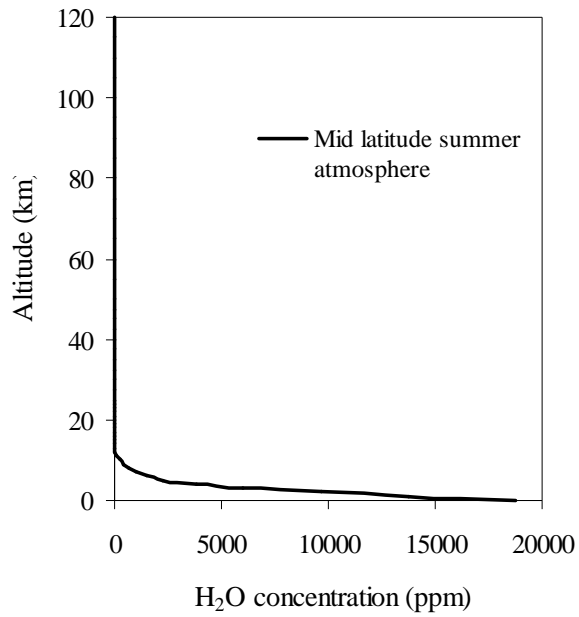


Figure 3.3 Concentration of H₂O profiles for midlatitude summer atmosphere [5]

In the model, the temperature of the ocean mixed layer, T_M , is evaluated by the following [125]

$$\rho_M C_{p,M} \Delta Z_M \frac{\partial T_M}{\partial t} = -LH - SH + S - IF \quad (3.1)$$

where ρ_M , $C_{p,M}$, ΔZ_M are the water density, 1000 kg/m³, water specific heat, 4.187 kJ/kgK, and thickness of the ocean mixed layer, 50m, respectively. S represents the solar heat flux at the boundary layer. IF is the longwave radiative heat flux at the boundary layer and is calculated by the radiation model. The details of the radiation model are given in section 3.2. The latent heat (LH) and sensible heat (SH) are calculated by

$$LH = \rho_s C_D V L (q_M^* - q_s) \quad (3.2)$$

$$SH = \rho_s C_D C_p V (T_M - T_s) \quad (3.3)$$

where ρ_s is the boundary air density obtained from the ideal gas law, C_D is the drag coefficient, 0.0014 [125], V is the surface wind, 5 m/s [125], L is the latent heat of evaporation 2500 kJ/kg. C_p is the air specific heat, 1.005 kJ/kgK. q_M^* is the saturation humidity evaluated at T_M , q_s is the boundary layer air humidity, T_s is the boundary layer air temperature. The saturation humidity at T_M is calculated in terms of mass average mixing ratio as

$$q_M^* = \frac{MW_{H_2O}}{MW_{air}} \cdot \frac{P^{sat}(T_M)}{P} \quad (3.4)$$

where P is the total pressure and MW_{H_2O} and MW_{air} are the molecular weight of the water and air, respectively. P^{sat} represents the saturation pressure of water vapor which is calculated by using the Clausius-Clapeyron relation as

$$P^{sat}(T) = P^{sat}(273) \cdot \exp \left[\frac{L}{R} \left(\frac{1}{273} - \frac{1}{T} \right) \right] \quad (3.5)$$

where $P^{sat}(273)$ is the saturation pressure of water vapor at $T = 273$ K, R is the gas constant. The boundary layer humidity, q_s , is calculated by using saturation humidity at T_M , q_M^* [125]

$$q_s = \frac{q_M^*}{1 + \frac{\kappa}{C_D V H_w}} \quad (3.6)$$

where κ denotes the eddy diffusion coefficient, $4.5 \times 10^4 \text{ cm}^2/\text{s}$, H_w is the H_2O scale height above the boundary layer which is equal to the thickness of the atmosphere.

Once q_s is calculated, the atmospheric relative humidity, RH, is calculated by [125]

$$RH(z) = RH_s \cdot (P/P_s) \quad q \geq 3 \text{ ppm} \quad (3.7)$$

The pressure of the water vapor, $P_{\text{H}_2\text{O}}$, and atmospheric humidity profile, $q(z)$, are determined by using

$$P_{\text{H}_2\text{O}}(z) = RH(z) \cdot P^{\text{sat}}(z) \quad (3.8)$$

$$q(z) = \frac{MW_{\text{H}_2\text{O}}}{MW_{\text{air}}} \cdot \frac{P_{\text{H}_2\text{O}}(z)}{P(z)} \quad (3.9)$$

After calculating the ocean mixed layer temperature, T_M , and humidity profile of the atmosphere, the temperature profile of the atmosphere is evaluated by

$$\frac{\partial(\rho C_p T)}{\partial t} = -\frac{d}{dz}(Q_c + S + IF) - LH \quad @ \ z = 0 \quad T = T_M \quad (3.10)$$

where latent heat release, LH, in the atmosphere is obtained from the precipitation of water vapor when the pressure of water vapor exceeds its saturation pressure. Q_c is the convective flux. An exact treatment for convective flux would require the solution of the equations of motion and continuity in addition to the solution of the energy equation. This ambitious task was generally not attempted by the radiative-convective models. Instead, Q_c is accounted for by semiempirical or empirical techniques. The semiempirical techniques employ the mixing length hypothesis to treat the heat flux due to convective elements. The mixing length theory assumes that the dominant mode of heat transport is by turbulent eddies that have length scales which are much smaller than the characteristic length scales of the problem [126]. With this assumption, Q_c can be expressed as

$$\begin{aligned}
Q_c &= -\rho C_p K_H \left(\frac{dT}{dz} + \Gamma \right) & \frac{dT}{dz} + \Gamma &\leq \mathbf{0} \\
Q_c &= 0 & \frac{dT}{dz} + \Gamma &\geq \mathbf{0}
\end{aligned} \tag{3.11}$$

where $\Gamma = g/C_p$ is the adiabatic temperature gradient and g is the acceleration due to gravity. K_H is the thermal diffusivity and is given by

$$K_H = 1.32z^2 \left(\frac{|(dT/dz) + \Gamma| g}{T} \right)^{1/2} \tag{3.12}$$

3.2 Radiation Model

In this section, radiation model based on method of lines (MOL) solution of discrete ordinate method (DOM) is described. Equations representing MOL solution of DOM are derived starting from RTE for one-dimensional system. This is followed by the numerical solution procedure utilized for MOL solution of DOM.

3.2.1 Radiative Transfer Equation (RTE)

The basis of all methods for the solution of radiation problems is the radiative transfer equation (RTE), which is derived by writing a balance equation for radiant energy passing in a specified direction through a small volume element in an absorbing-emitting, nongray medium and can be written in the form

$$\frac{dI_\eta}{ds} = (\mathbf{\Omega} \cdot \nabla) I_\eta(\mathbf{r}, \mathbf{\Omega}) = -\kappa_\eta I_\eta(\mathbf{r}, \mathbf{\Omega}) + \kappa_\eta I_{b\eta}(\mathbf{r}) \tag{3.13}$$

where $I_\eta(\mathbf{r}, \mathbf{\Omega})$ is the spectral radiation intensity at position \mathbf{r} in the direction $\mathbf{\Omega}$. κ_η is the spectral absorption coefficient of the medium and $I_{b\eta}$ is the spectral blackbody radiation intensity at the temperature of the medium. The expression on the left-hand side represents the change of intensity in the specified direction $\mathbf{\Omega}$. The first term on the right-hand side is attenuation through absorption and the second term represents augmentation due to emission.

In a one-dimensional system, the directional derivative of radiation intensity can be expressed as

$$\frac{dI_\eta}{ds} = \mu \frac{dI_\eta}{dz} = -\kappa_\eta I_\eta(\mathbf{r}, \boldsymbol{\Omega}) + \kappa_\eta I_{b\eta}(\mathbf{r}) \quad (3.14)$$

where the direction cosine, μ , can be expressed in terms of polar angle θ as $\mu = \cos \theta$ (Figure 3.4).

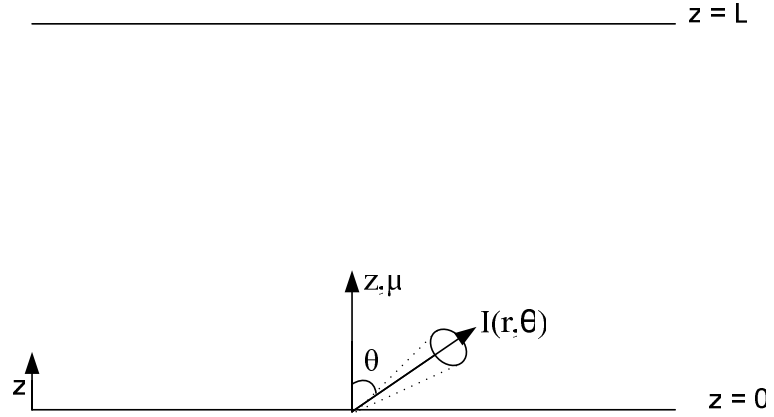


Figure 3.4 Coordinate system for one-dimensional plane parallel system

If the bottom surface which is the Earth's surface is assumed to be black at a specified temperature, and the downward radiation is zero at the upper surface which represents the top of the atmosphere ($z = L$), Eq. (3.13) is subject to the following boundary conditions:

$$I_\eta(0, \mu) = I_{b\eta}(T_{w1}) = \frac{\sigma T_{w1}^4}{\pi} \quad \text{for } \mu > 0 \quad (3.15)$$

$$I_\eta(L, \mu) = 0 \quad \text{for } \mu < 0 \quad (3.16)$$

where $I_\eta(0, \mu)$ is the spectral radiative intensities leaving the surface of the Earth ($z = 0$) and the top of the atmosphere ($z = L$), respectively. $I_{b\eta}(T_{w1})$ is the black body intensity at the bottom surface where T_{w1} is the temperature of the bottom surface.

In order to determine the radiative intensity distribution, the longwave region of spectrum is discretized into wave number intervals within which the radiative properties are assumed to be constant. All wave number intervals having an absorption coefficient within a certain range are combined to a gray gas so the RTE (Eq.(3.13)) is solved for each gray gas by modifying the Eq. (3.13) as follows:

$$\frac{dI_j}{ds} = \mu \frac{dI_j}{dz} = \kappa_j (a_j I_b - I_j) \quad (3.17)$$

where subscript j denotes the spectral division and a_j are the blackbody weights determined from the standard blackbody distribution function in the Wide Band Correlated- k (WBCK) model [76]. $I_b (\equiv \sigma T^4 / \pi)$ is the blackbody radiation intensity. This form of RTE in Eq. (3.17) is known as the Weighted Sum of Gray Gases (WSGG) RTE derived by Modest [127] from WSGG model which was first introduced by Hottel and Sarofim [128] for total emissivity calculation. Estimation of spectral properties will be discussed in detail in the following chapter.

Eq. (3.17) is solved for each gray gas with the following modified boundary conditions:

$$I_j(0, \mu) = a_j I_b(T_{w1}) \quad \text{for } \mu > 0 \quad (3.18)$$

$$I_j(L, \mu) = 0 \quad \text{for } \mu < 0 \quad (3.19)$$

Once the radiation intensities are determined by solving Eq. (3.17) together with its boundary conditions (Eqs. (3.18) and (3.19)), quantities of interest such as radiative heat flux and energy source term can be readily evaluated. The net radiative heat flux on a surface element is defined as:

$$q_{\text{net}} = q^+ - q^- \quad (3.20)$$

where q^+ and q^- are incident and leaving wall heat fluxes, respectively. For the boundaries of the system, q^+ and q^- are evaluated from:

$$q^+ = \pi I_{bw1} = \sigma T_{w1}^4 \quad (3.21)$$

$$q^- = 0 \quad (3.22)$$

The radiative energy source term for problems where temperature distributions are available is expressed as

$$\text{div } \mathbf{q} = \sum_j^{NG} \kappa_j \left(4\pi a_j I_b - \int_{4\pi} I_j(\mathbf{r}, \boldsymbol{\Omega}) d\boldsymbol{\Omega} \right) \quad (3.23)$$

3.2.2 Discrete Ordinates Method (DOM)

In the DOM, the RTE is replaced by a discrete set of equations for a finite number of ordinate directions. For the system under consideration, Eq. (3.17) takes the following form:

$$\mu_m \frac{d I_j^m}{d z} = \kappa_j (a_j I_b - I_j^m) \quad (3.24)$$

where $I_j^m [=I_j(z; \mu)]$ is the total spectral radiation intensity at position (z) in the discrete direction $\mu_m (= \cos \theta)$, m represents the discrete direction, $m= 1, 2, \dots, M$ and M is the total number of directions used in the approximation.

The resulting set of differential equations for I_j^m is solved together with the following boundary conditions

$$I_j^m(0, \mu_m) = a_j I_b(T_{w1}) \quad \text{for } \mu_m > 0 \quad (3.25)$$

$$I_j^m(L, \mu_m) = 0 \quad \text{for } \mu_m < 0 \quad (3.26)$$

The accuracy of discrete ordinates method is affected by the order of approximation and the angular quadrature scheme. In an investigation carried out by Selçuk and Kayakol [129] on the assessment of the effect of these parameters on the predictive accuracy of DOM by verification against exact solutions, it was concluded that the order of approximation plays a more significant role than angular quadrature scheme in the accuracy of predicted radiative heat fluxes and radiative energy source

terms.

The order of approximation of DOM determines the total number of discrete directions, M . A sketch of the directions used in one octant of a unit sphere for S_2 , S_4 , S_6 and S_8 order of approximations is shown in Figure 3.5. As can be seen from the figure, discrete directions are ordered in levels (constant θ) and number of directions is different at each level. Table 3.1 summarizes the total number of discrete directions, total number of levels for each order of approximation and number of discrete directions on each level in one octant of a unit sphere for one-dimensional problems. When a discrete number of directions is used to approximate a continuous angular variation, ray effect is unavoidable [130]. The increase in the number of discrete directions would alleviate the ray effect, however, at the expense of additional computational time and memory requirement.

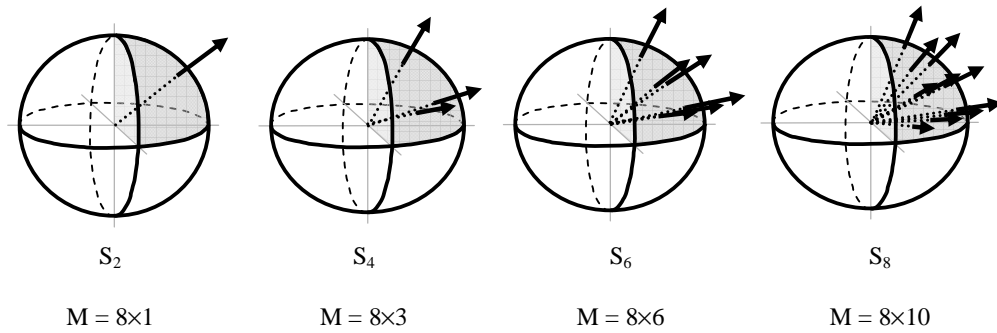


Figure 3.5 Orders of approximation

Table 3.1 Total number of discrete directions specified by order of approximation

Order of approximation	1-D M = N	Number of levels (= N/2)	Number of points at i th level (= N/2 - i + 1)
S ₂	2	1	2-I
S ₄	4	2	3-I
S ₆	6	3	4-I
S ₈	8	4	5-I

The angular quadrature scheme also affects the accuracy of DOM. Solution of RTE requires the specifications of ordinates $\Omega_m (\mu_m, \zeta_m, \xi_m)$ and corresponding weights w_m . The choice of quadrature scheme is arbitrary although restrictions on the directions and weights arise from the need to preserve symmetries and invariance properties of the physical system. Completely symmetric angular quadrature schemes, which mean symmetry of the point and surface about the center of the unit sphere, also about every coordinate axis as well as every plane containing two coordinate axes, are preferred because of their generality and to avoid directional biasing solutions. Therefore, the description of the points in one octant is sufficient to describe the points in all octants.

The most frequently used angular quadrature scheme is S_N, originally developed by Carlson and Lathrop [131] and extended to higher order of approximations by Fiveland [132] and El Wakil and Sacadura [133]. Therefore, in this study MOL solution of DOM calculations will be based on S_N angular quadrature scheme. The quadrature ordinates and weights for one-dimensional parallel plane of S_N approximations are tabulated in Table 3.2.

Table 3.2 Direction cosines and weights for one-dimensional systems

Order of Approximation	Ordinates μ_m	Weights w_m
S_2	0.5000000	1.0000000
	0.2958759	0.6666667
S_4	0.9082483	0.3333333
	0.1838670	0.4357983
S_6	0.6950514	0.4617364
	0.9656013	0.1024650
S_8	0.1422555	0.3443658
	0.5773503	0.4202803
	0.8040087	0.1263415
	0.9795543	0.1090122

Once the intensities at each ordinate are determined by solving Eq. (3.24) together with its boundary conditions, the net radiative flux and source term can be obtained from the following equations

$$q_{net} = q^+ - q^- = \varepsilon_w \left(\sum_j^{NG} \sum_m^M w_m \mu_m I_j^m - a_j \pi I_b \right) \quad (3.27)$$

$$div \mathbf{q} = \sum_j^{NG} \kappa_j (4\pi a_j I_b - \sum_m^M w_m I_j^m) \quad (3.28)$$

3.2.3 The Method of Lines (MOL) Solution of DOM

The solution of discrete ordinates equations with MOL is obtained by adaptation of the false-transients approach which involves incorporation of a pseudo-time derivative of intensity into the discrete ordinates equations [45]. The false-transient approach is adapted to Eq. (3.24) as:

$$k_t \frac{\partial I_j^m}{\partial t} = -\mu_m \frac{\partial I_j^m}{\partial z} + \kappa_j (a_j I_b - I_j^m) \quad (3.29)$$

where t is the pseudo-time variable and the effect of pseudo time derivative added to the equation vanishes at steady state. k_t is a time constant with dimension $[(m/s)^{-1}]$ which is introduced to maintain dimensional consistence in the equation and it is taken as unity.

The PDE for each direction with initial and boundary-value independent variables is then transformed into an ODE initial value problem by using MOL approach [134]. This transformation is carried out by illustration of the spatial derivatives with the algebraic finite-difference approximations.

Starting from an initial condition for radiation intensities in all directions, the resulting ODE system is integrated until steady state by using a powerful ODE solver. The ODE solver takes the burden of time discretization and chooses the time steps in a way that maintains the accuracy and stability of the evolving solution. In this thesis study, the same ODE solver, ROWMAP, used for the solution of the governing equations of the radiative-convective model was used in the radiation model. Any initial condition can be chosen to start the integration, as its effect on the

steady-state solution decays to insignificance. To stop the integration at steady state, a convergence criterion was introduced. If the intensities at all nodes and ordinates for all gray gases satisfy the condition given below, the solution at current time is considered to be the steady state solution and the integration is terminated. The condition for steady state is

$$\frac{|I_t - I_{t-1}|}{I_{t-1}} < \epsilon \quad (3.30)$$

where ϵ represents the error tolerance, the subscript t denotes the solution at current print time and subscript $t-1$ indicates solutions at previous print time. As a result, evolution of radiative intensity with time at each node and ordinate is obtained.

Once the steady state intensities at all grid points for all gray gases are available, the net radiative heat flux on enclosure boundaries and radiative source term at interior grid points can be evaluated by using Eqs. (3.27) and (3.28), respectively.

3.3 Numerical Solution Technique

In this study, for solution methods to be compatible with each other, the governing equations of both the radiative-convective model and the radiation model are solved by using the Method of Lines (MOL) technique. In the following sections, first the MOL is described. This is followed by the coupling procedure of the radiation model and the radiative-convective model and the algorithm of the coupled code.

3.3.1 The Method of Lines

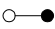
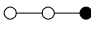
The method of lines consists of converting the system of partial differential equations (PDEs) into an ODE initial value problem by discretizing derivatives together with boundary conditions via Taylor series or weighted residual techniques and integrating the resulting ODEs using sophisticated ODE solver which takes the burden of time discretization and chooses the time steps in such a way that maintains the accuracy and stability of the evolving solution. The most important advantage of the MOL approach is that it has not only the simplicity of the explicit methods but also the superiority (stability advantage) of the implicit ones unless a poor numerical

method for the solution of ODEs is employed. The advantages of the MOL approach are two-fold. First, it is possible to achieve higher-order approximations of discretization of spatial derivatives without any significant increase in computational complexity, and without additional difficulties with boundary conditions. Second, the use of highly efficient and reliable initial value ODE solvers means that comparable orders of accuracy can also be achieved in the time integration without using extremely small time steps.

The most important feature of the MOL approach is that it has not only the simplicity of the explicit methods but also the superiority of the implicit ones as the higher-order implicit time integration methods are employed in the solution of the resulting stiff system of ODEs. The stiff ODE concept is well established and various efficient and reliable stiff ODE solvers, having the advantage of the use of variable time steps and order of the method, are available in the open literature[134-137]. However, it is very important to select a suitable one considering type and dimension of the physical system, desired level of accuracy and execution time. In the present study, a higher-order and stable schemes embedded in quality ODE solver; ROWMAP was used. ROWMAP is based on the ROW-methods of order 4 and uses Krylov techniques for the solution of linear systems. By a special multiple Arnoldi process the order of the basic method is preserved with small Krylov dimensions. Step size control is done by embedding with a method of order 6. Detailed description of ROWMAP can be found elsewhere [138] .

In this thesis study, two- and three-point upwind finite difference schemes are used as spatial discretization schemes [134, 139]. The reason behind the choice of upwind schemes is as follows: After the implementation of false-transients approach discrete ordinates equations take the form of first-order hyperbolic PDEs and for which it was demonstrated that upwind schemes eliminate the numerical oscillations caused by central differencing, as the direction of propagation of the dependent variables are taken into account in upwind schemes [134, 139]. The formulation and order of accuracy of the selected schemes are presented in Table 3.3.

Table 3.3 Spatial differencing schemes [134, 139]

Name of the scheme	Stencil	Formulation, $dI(\lambda I)/d\lambda \approx$	Order of accuracy
2-point upwind (DSS012)		$(I_i - I_{i-1}) / \Delta \lambda$	$O(\Delta \lambda)$
3-point upwind (DSS014)		$(3I_i - 4I_{i-1} + I_{i-2}) / 2\Delta \lambda$	$O(\Delta \lambda^2)$

3.3.2 Coupling Procedure for Radiative-Convective Model

Coupling strategy between the radiative-convective and the radiation model is mainly based on periodic transfer of temperature and concentration distributions calculated in the radiative-convective model to radiation model which in turn provides the radiative heat fluxes to be inserted in the energy conservation equation of the atmosphere and the surface . The schematic representation of the coupling procedure is illustrated in Figure 3.6.

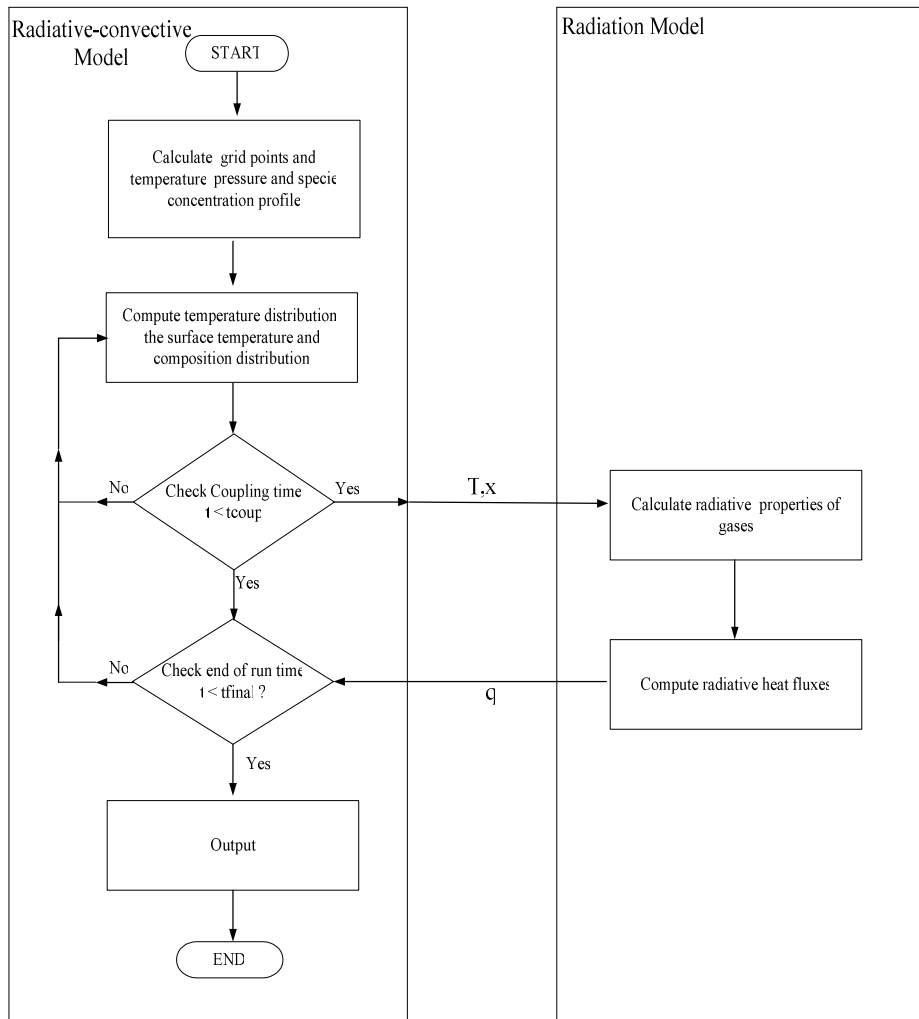


Figure 3.6 Coupling procedure

3.3.2.1 Algorithm of Coupled Code

The algorithm of the radiative-convective model is illustrated in Figure 3.7. The whole procedure of coupled code can be summarized as follows:

1. Define the subdivision of the system, order of approximation, spatial differencing scheme, number of gray gases and number of equations in the system of ODEs.
2. Read in input data specifying the physics of the problem which are the dimension of the plane parallel, grid boundary data, boundary temperatures and emissivities
3. Evaluate pressure and temperature at each grid point; and average temperature, pressure and specie density between consecutive grid points by using INPUT subroutine.
4. Read in input data related with the ODE integrator which are the initial time, time of coupling interval, final time, print interval and the error tolerance.
5. Set the initial conditions required for the ODE integrator.
6. Initialize the intensities at all ordinates at all grid points for all gray gases and temperature through the atmosphere.
7. Calculate radiation flux by using initial intensities at all ordinates at all grid points for all gray gases
8. Set boundary conditions for the intensities leaving the boundary surfaces by using Eqs. (3.25 and 3.26) and for temperature leaving the boundary surface Eq. (3.8).

Calculation of the Temperature Distribution

9. Specify a discrete location at the z direction.
10. Calculate spatial derivatives of convection and infrared fluxes in Eq (3.8)
11. Calculate the time derivative of temperature
12. Transform the 1-D arrays of temperature and time derivatives into 1-D arrays to be sent to the ODE solver.

13. Call the ODE solver subroutine to integrate the system of ODEs by using a time adaptive method. The ODE propagates in time by solving for the temperatures at a time step j , calculating the time derivatives by performing steps 8 to 11 and integrating again to solve for temperatures at the new time step $j+1$.
14. Return to the main program at prespecified time intervals.
15. Check if ODE integration has proceeded satisfactorily, print an error message if an error condition exists.
16. Transfer the solution at current print point from the 1-D array to a 1-D array.
17. Set the boundary conditions at current time step.
18. Check the lapse rate for each grid points. When lapse rate is greater than the stability conditions, repeat steps 9-16 until the lapse rate is smaller than the stability conditions.
19. Print solution

Calculation of the Surface Temperature

20. Set the time.
21. Specify a discrete location at the z direction.
22. Calculate the time derivative of surface temperature.
23. Transform the 1-D arrays of temperature and time derivatives into 1-D arrays to be sent to the ODE solver.
24. Call the ODE solver subroutine to integrate the system of ODEs by using a time adaptive method. The ODE propagates in time by solving for the surface temperature at a time step j , calculating the time derivatives by performing steps 20 to 23 and integrating again to solve for the surface temperature at the new time step $j+1$.
25. Return to the main program at prespecified time intervals.
26. Check if ODE integration has proceeded satisfactorily, print an error message if an error condition exists.
27. Transfer the solution at current print point from the 1-D array to a 1-D array.

28. Calculate atmospheric humidity and precipitation amount of water vapor.
29. Print solution

Calculation of the Temperature Distribution Again

30. Set the time
31. Calculate temperature profile according to new data by repeating steps 8-19
32. Check the lapse rate for each grid points. When lapse rate is greater than the stability conditions , go to step 30 until the lapse rate is smaller than the stability conditions.
33. Check the precipitation amount of water vapor for each grid points. When it is greater than condition , go to step 30 until it is smaller than condition.
34. Check the coupling interval. If time is smaller than the time of the coupling interval go to 9
35. Print solution

Calculation of Radiation Fluxes

36. Calculate absorption coefficients and associated weights at each grid point in the medium for each gray gas using PROPERTY subroutine.
37. Set boundary conditions for the intensities leaving the boundary surfaces by using Eqs. (3.25 and 3.26).
38. Specify a gray gas, an octant, and an ordinate.
39. Specify a discrete location at the z direction.
40. Store the values of the intensities (at this direction and location for this gray gas) which are 3-D arrays along z-axis in a 1-D array.
41. Call for spatial discretization subroutine which accepts the 1-D array of intensities as an input and computes the derivative with respect to z-axis as an output over the grid of the number of points.
42. Transfer the 1-D array of spatial derivatives into the 3-D array of z-derivatives.

43. Repeat steps 38-43 for all discrete locations at z direction, all ordinates and all octants for all gray gases.
44. Calculate the time derivative of intensity at each node for each ordinate of each octant for each gray gas using Eq. (3.29) to form a 3-D array of time derivatives.
45. Transform the 4-D arrays of intensities and time derivatives into 1-D arrays to be sent to the ODE solver.
46. Call the ODE solver subroutine to integrate the system of ODEs by using a time adaptive method. The ODE propagates in time by solving for the intensities at a time step j, calculating the time derivatives by performing steps 37 to 45 and integrating again to solve for intensities at the new time step j+1.
47. Return to the main program at prespecified time intervals.
48. Check if ODE integration has proceeded satisfactorily, print an error message if an error condition exists.
49. Transfer the solution at current print point from the 1-D array to a 3-D array.
50. Set the boundary conditions at current time step.
51. Print solution
52. Check for convergence by comparing the solutions at current time step with those at previous three time steps. If current solution is within the specified range of the previous solutions, convergence is established go to step 55.
53. If convergence is not established, save the solution for convergence check.
54. Check the end of run time if final time is not reached go back to step 38.
55. If convergence is established or final time is reached, calculate the parameters of interest such as radiative heat flux and go to main program.
56. Check the end of run time if final time is not reached go back to step 9.
57. Stop.

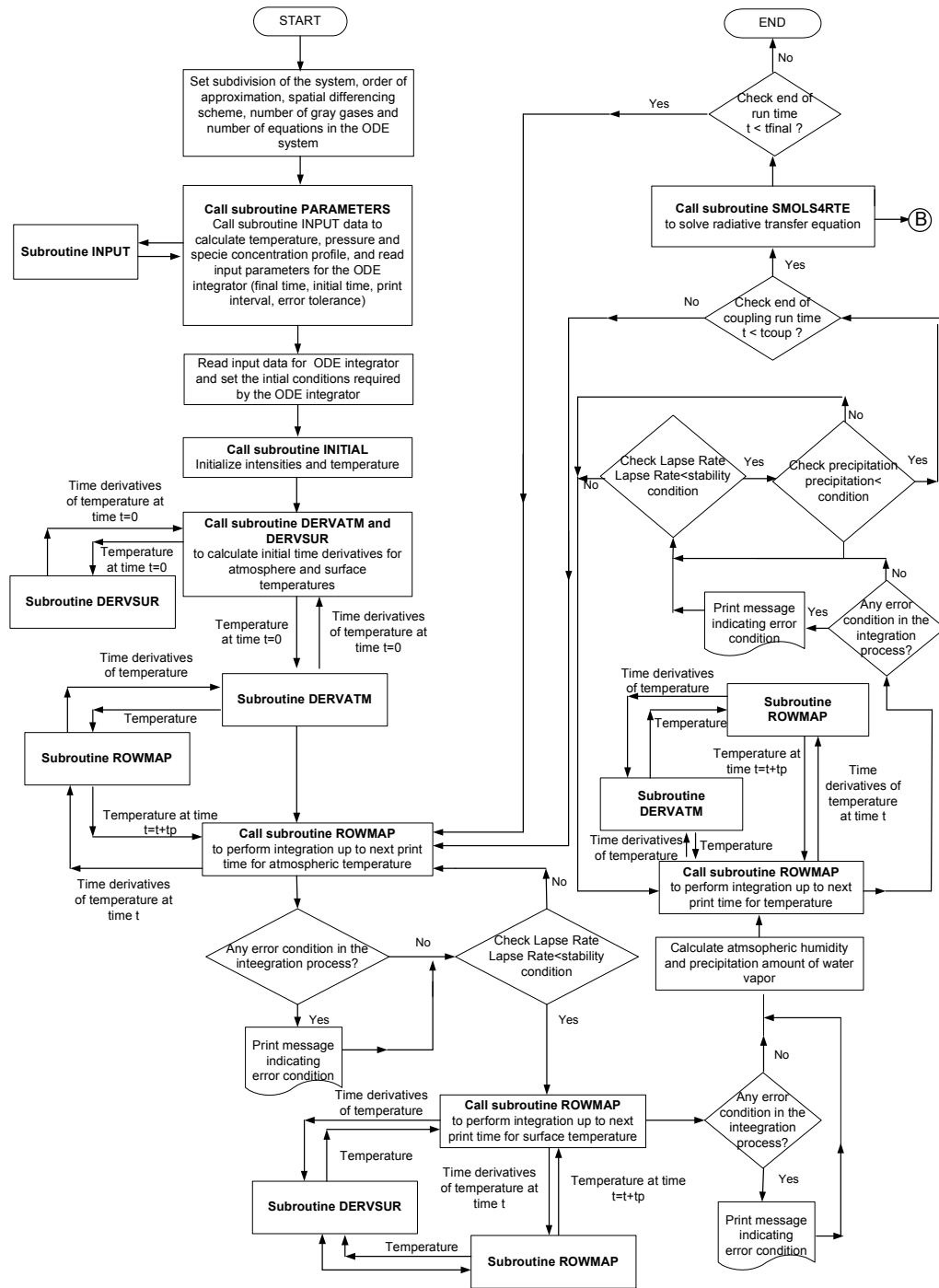


Figure 3.7 Algorithm of the radiative-convective model

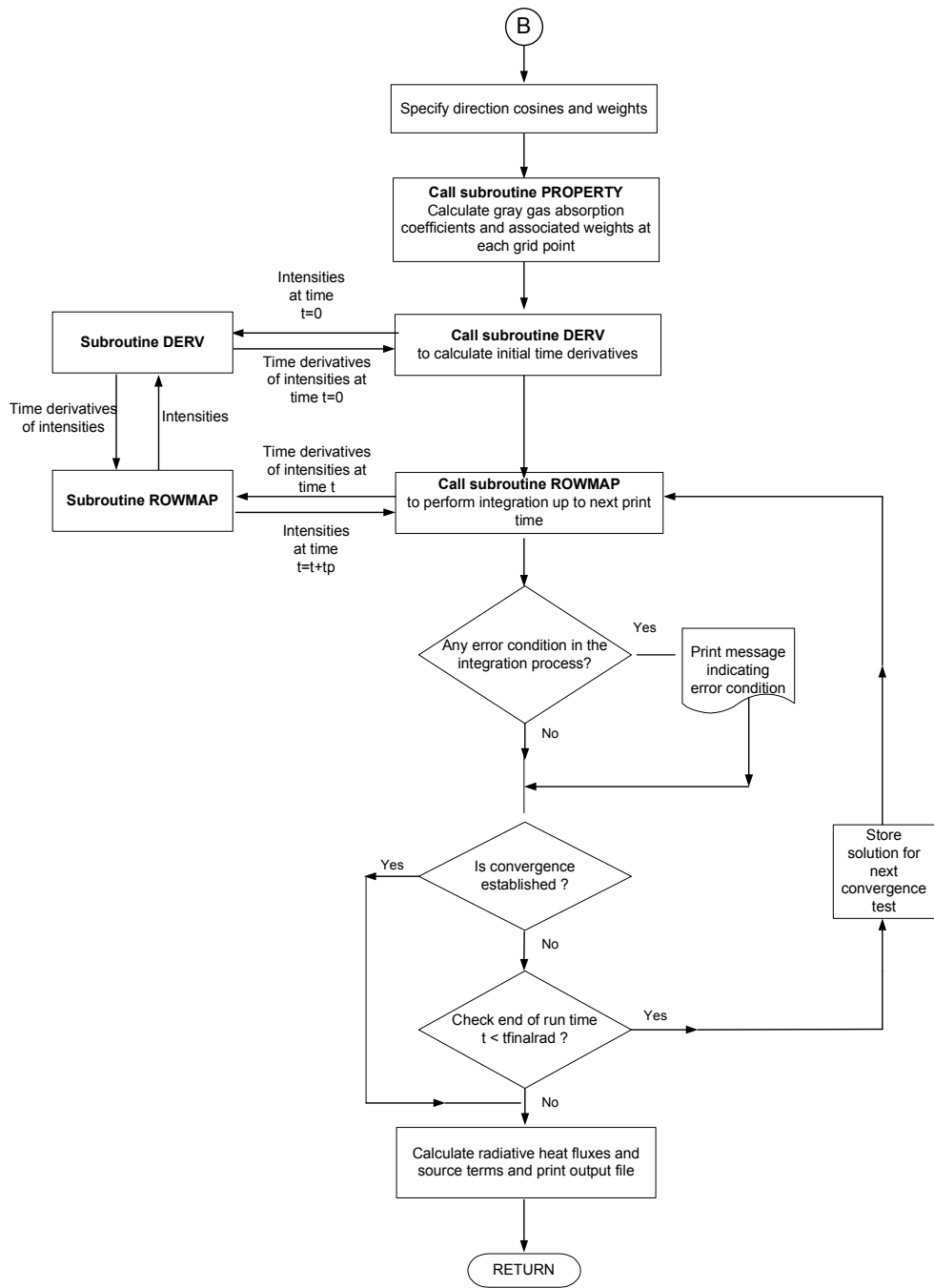


Figure 3.7 Algorithm of the radiative-convective model (continued)

CHAPTER 4

ESTIMATION OF RADIATIVE PROPERTIES

Accurate determination of radiative transfer necessitates both accurate solution of the RTE and reliable evaluation of the medium radiative properties. In the preceding chapter, MOL solution of DOM as an accurate and efficient technique for the solution of RTE was explained. In this chapter, the gas radiative property model utilized in the present study will be described.

4.1 Gas Radiative Property Models

The most fundamental radiative property of participating gases is the absorption coefficient or the absorption cross-section when the absorption coefficient is normalized by the molar density [140]. The variation of absorption coefficient or absorption cross-section of a gas with wave number is called a spectrum, and it consists of millions of spectral lines, which are produced by the vibrational-rotational transitions in molecular energy levels. Absorption coefficient has a strong dependence on wave number. Because of this fact, numerical simulation of radiative heat transfer is a formidable task. A number of models with varying degrees of complexity and accuracy has been developed so far for the estimation of the radiative properties. Line-by-line (LBL) model [141], which is the most accurate of all, requires calculation of radiative properties for millions of vibrational-rotational lines, and hence, its computational cost is extremely high for climate models as well as practical engineering applications. The significant computational burden required by LBL model has necessitated the use of band models which are designed to approximate the nongray gas behavior over wave number intervals within which the radiative properties are assumed to be constant. Depending on the width of wave

number intervals, band models are classified as narrow band and wide band models. Drawback of these models is that they provide gas transmissivities instead of absorption coefficients which are required for the solution of RTE. This problem can be alleviated by utilizing hybrid models such as statistical narrow-band correlated-k (SNB-CK) [142] and wide band correlated-k (WBCK) models [74-77]. K model was chosen due to its compatibility with MOL solution of DOM as it provides absorption coefficient as input to the RTE solver and its proven computational efficiency [53, 79, 80]. Another reason behind its selection is the suitability of its correlation parameters to atmospheric condition. The details of this model can be found elsewhere [53]. However, for the sake of integrity, a brief summary of the model will be provided in the following sections.

4.2 Wide Band Correlated-k (WBCK) Model

WBCK model is based on re-ordering the wave numbers within the wide bands to yield a smooth, monotonic decreasing function, which makes it possible to introduce a discretized set of absorption coefficients, each representing a gray gas that can easily be applied to the WSGG RTE (Eq. (3.17)) [53].

For determination of monotonic decreasing function, the wave numbers within a wide band, Denison and Fiveland [76] have proposed a simple correlation for the dimensionless wave number, ξ^* , as function of dimensionless absorption coefficient, κ^* , by a fit to the four-region expression for wide band absorptance developed by Edwards and his co-workers [143, 144], [79]

$$\xi^*(\kappa^*) = \sum_{i=1}^{n_p} C_{i,1} E_1(p_i \kappa^*) + C_{1,2} \frac{e^{-p_1 \kappa^*}}{p_1} \quad (4.1)$$

where ξ^* , κ^* and E_1 , exponential integral function of order 1, are defined in Equations (4.2), (4.3) and (4.4), respectively.

$$\xi^* = \frac{\xi}{\omega} \quad (4.2)$$

$$\kappa^* = \frac{\kappa}{\rho \alpha / \omega} = \frac{C_{abs}}{M_w \alpha / \omega} \quad (4.3)$$

$$E_1(p_i \kappa^*) = \int_1^{\infty} e^{-p_i \kappa^* t} \frac{dt}{t} \quad (4.4)$$

In Eq. (4.2), ρ and M_w are the density and molecular weight of the absorbing gas, respectively. The coefficients $C_{i,j}$, poles p_i and n_p appearing in Eq.(4.1) are given as functions of line-overlap parameter β and illustrated in Table 4.1. The exponential wide band model parameters, α , β and ω are evaluated for each wide band at the average temperature and mole fraction of layers in the medium. Moreover, the detailed descriptions of the exponential wide band model parameters are given in Appendix A.

Once the re-ordered wave numbers, ξ_j , are evaluated from Eq.(4.1), the wave numbers, η , are calculated from the following equation depending on whether the band head is situated in the center, lower limit or upper limit of the band (see Figure 4.1) [53]

$$\eta(\kappa) = \begin{cases} \eta_l + \xi_j(\kappa) & \text{(lower limit)} \\ \eta_c \pm \xi_j(\kappa)/2 & \text{(centre)} \\ \eta_u - \xi_j(\kappa) & \text{(upper limit)} \end{cases} \quad (4.5)$$

Table 4.1 Poles, p_i , and coefficients, C_{ij} [76]

	$0.001 < \beta \leq 0.0202256$	$0.0202256 < \beta < 0.2003$	$0.2003 \leq \beta \leq 1$
n_p	3	2	1
p_1	$6.78622E-4 + 3.61937 \beta$ $-30.2514 \beta^2 + 2181.40$ β^3	$7.27821E-2 - 1.39993 \beta$ $+104.659 \beta^2 - 996.743 \beta$ β^3 $+3117.65 \beta^4$	$1 + 2.864 \sqrt{1 - \frac{(1-\beta)^4}{0.408986}}$
p_2	$1/p_1$	$1/p_1$	-
p_3	1	-	-
$C_{1,1}$	$p_1 C_{2,1}$	$(p_1^2 - p_1) / (p_1^2 - 1)$	1
$C_{2,1}$	$0.952246 - 12.9573 \beta$ $+877.601 \beta^2 - 14851.1$ β^3	$(p_1 - 1) / (p_1^2 - 1)$	-
$C_{3,1}$	$1 - C_{1,1} - C_{2,1}$	-	-
$C_{1,2}$	0	0	$p_1^2 - p_1$

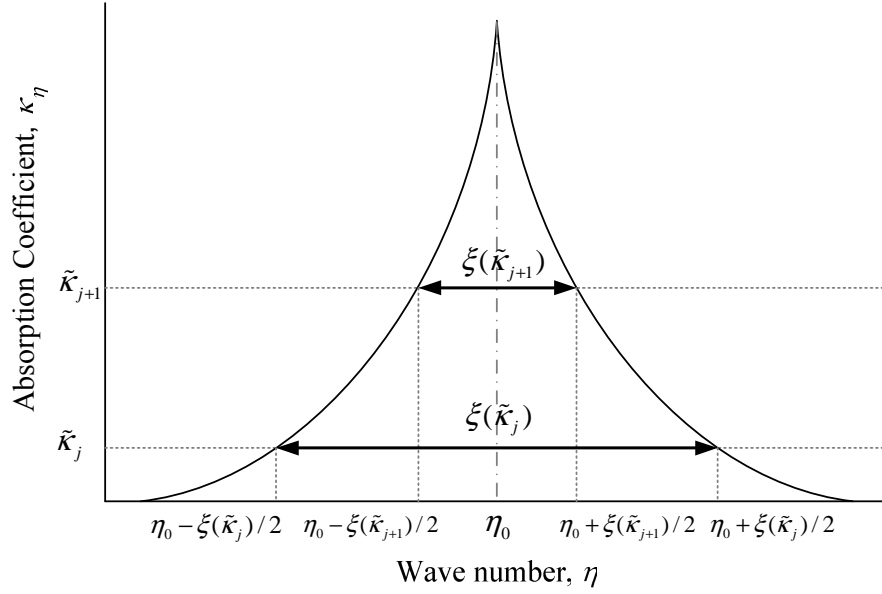


Figure 4.1 Discretization of representative re-ordered band [53]

C_{abs} appearing in Eq. (4.3) represents a constant absorption cross-section calculated and is calculated by [79]

$$C_{abs,j} = \exp \left[\frac{\ln(\tilde{C}_{abs,j}) + \ln(\tilde{C}_{abs,j+1})}{2} \right] \quad (4.6)$$

where $\tilde{C}_{abs,j}$ is the supplemental absorption cross-sections which is logarithmically spaced absorption cross-sections. In this study, 10 absorption cross-sections logarithmically spaced between 6×10^{-6} and $550 \text{ m}^2/\text{mol}$ which are obtained by using data of infrared cross-sections from Pacific Northwest National Laboratory (PNNL) [145] were utilized. Once the absorption cross-sections for each gray are obtained, local absorption coefficients of each gray gas are calculated from [80]

$$\kappa_j = N \cdot C_{abs,j} \quad (4.7)$$

where molar density, N , is evaluated from ideal gas equation of state in the present

study. One gray gas is associated with zero absorption coefficient and utilized to account for the transparent regions and it is called a “transparent gas” [53].

The gray gas weights, a_j , in Eq. (3.17) are calculated as blackbody fractions $F(\eta, T)$ for re-ordered wavenumber intervals where the absorption coefficient lies between $\kappa_{j-1/2}$ and $\kappa_{j+1/2}$ (Figure 4.1) . The re-ordered wave numbers in each wide band , ξ_k , and the band center wavenumber, $\eta_{0,k}$, provide the wavenumbers from which these black body functions are calculated. For a band with symmetric band head, gray weight is calculated as follows [79]

$$a_j = \sum_i \left\{ F \left[\eta_{0,k} - \xi_k (\kappa_{j+1/2}) / 2, T \right] - F \left[\eta_{0,k} - \xi_k (\kappa_{j-1/2}) / 2, T \right] \right. \\ \left. + F \left[\eta_{0,k} + \xi_k (\kappa_{j-1/2}) / 2, T \right] - F \left[\eta_{0,k} + \xi_k (\kappa_{j+1/2}) / 2, T \right] \right\} \quad (4.8)$$

Similar expression can be written for bands with upper-limit and lower-limit band heads [79].

$F(\eta, T)$ in each band have been provided by Chang and Rhee [146]

$$F(\eta, T) = \frac{15}{\pi^4} \sum_{n=1}^{\infty} \frac{e^{-n\nu}}{n} \left(\nu^3 + \frac{3\nu^2}{n} + \frac{6\nu}{n^2} + \frac{6}{n^3} \right) \quad (4.9)$$

where $\nu = C_2 \eta / T$ and $C_2 = 14388 \mu\text{m K}$. This series converges to exact result rapidly for $n=4$ [147] . All weights including the one for transparent gas sum to unity [53]

$$\sum_{j=1}^{NG} a_j = 1 \quad (4.10)$$

CHAPTER 5

RESULTS AND DISCUSSION

In this thesis study, first, Line-By-Line Radiative Transfer Model (LBLRTM) developed by Clough et al. [81] based on analytical solution of RTE was used to investigate the effects of carbon dioxide, water vapor and the temperature distribution of the atmosphere on global warming. Moreover, the predictive accuracy and computational efficiency of MOL solution of DOM with WBCK was assessed by applying it to the predictions of radiative heat fluxes for which benchmark solutions were obtained by using LBLRTM. Furthermore, the radiative-convective model in conjunction with radiation model based on MOL solution of DOM with WBCK was utilized to demonstrate the effect of the coupling interval on the accuracy of the radiative-convective model.

5.1 LBLRTM

LBLRTM developed by Clough et al. [81] was used and applied to the calculation of clear-sky longwave fluxes and cooling rates of atmosphere including CO₂ and water vapor. The model is based on analytical solution of RTE. Line-by-line method is used as radiative property estimation model. LBLRTM has three relevant features: (i) it has been and continuous to be extensively validated against atmospheric radiance spectra, (ii) it incorporates a full water vapor continuum model and, (iii) its computational efficiency mitigates the computational burden of the line-by-line cooling rate calculation [7].

Detailed description of the LBLRTM can be found elsewhere [7, 81]. The source code of LBLRTM can be obtained from the internet site: <http://rtweb.aer.com/lblrtm.html>.

5.1.1 Effect of Carbon Dioxide, Water Vapor and Temperature Changes on the Fluxes in the Atmosphere and the Earth's Surface

In an attempt to see the effect of carbon dioxide, water vapor and temperature on the fluxes, LBLRTM was applied to a 1-D longwave clear sky atmosphere which was approximated to be a nonhomogenous absorbing-emitting, non-scattering medium containing two main absorber gases: water vapor and carbon dioxide.

The atmosphere was divided into 60 homogenous layers. For each layer, constant logarithmic mean temperature, pressure and gas concentration were calculated and radiative property of gases were evaluated. The spectral line parameters were obtained from HITRAN 2004 [148]. The longwave spectral range considered was from 10 to 3000 cm^{-1} . The model was applied to midlatitude summer and tropical atmospheres which are the reference atmospheres of the Air Force Geophysical Laboratories (AFGL) [5]. The water vapor concentration profiles given in the reference atmospheres of AFGL were utilized in this study. However, instead of using their concentration of carbon dioxide, today's value of carbon dioxide which is 383 ppm [149] was used. The top of the atmosphere was assumed to be at nearly 100 km (0 mbar). The emissivity of Earth's surface was taken as 1. It was assumed that there was no incident longwave radiation at the top of the atmosphere.

Before investigating the effect of carbon dioxide and water vapor on fluxes, for verification of the code, the LBLRTM was executed by using the same input parameters used in Clough and Iacono [7]. As can be seen in Table 5.1, the predictions of the code were found to be in complete agreement with the findings of Clough and Iacono [7].

Table 5.1 Comparison between the predicted net fluxes by the code and the findings of Clough and Iacono [7]

	Clough and Iacono [7]	This study	Absolute % relative error*
At top of the atmosphere (~ 100 km)	76.6	76.7	0.13
At tropopause (13 km)	265.3	267.0	0.64
At surface	283.3	285.4	0.74

*Absolute % relative error = $(|\text{predicted-LBLRTM}| / \text{LBLRTM}) \times 100$

In this study, in an attempt to see the effect of doubling CO₂ concentration on net fluxes, temperature, pressure and water vapor concentration profiles of midlatitude summer atmosphere were kept constant and the CO₂ concentration was increased from 383 ppm to 766 ppm. The findings of this study were then compared with the findings of previous studies, details of which are tabulated in Table 1.1. The changes in the net fluxes in the atmosphere and the Earth's surface due to doubling CO₂ concentration in these studies are tabulated in Table 5.2. Although different models with different conditions were used in these studies, the findings were found to be close to each other. As can be seen in Table 5.2, when the concentration of CO₂ was doubled, changes in the net flux at the top of the atmosphere, at tropopause and at the surface were all calculated to be negative in all studies. This means that the atmosphere becomes warmer due to more absorption and emission of the medium. Therefore, it can be concluded that the atmosphere warms up when the concentration of the carbon dioxide is doubled.

Table 5.2 Changes in the net fluxes (W/m^2) in the atmosphere and the Earth's surface in midlatitude summer atmosphere due to doubling the CO_2

	This study	Mlawer et al. [6]	Clough and Iacono [7]	Feigelson et al. [8]	Morcrette [9]	Ridgway et al. [10]	
						LBL	Broad band
Change of conc. of CO_2 (ppm)	383→766	355→710	355→710	300→600	300→600	300→600	
At top of the atmosphere	-2.8	-3.1	-2.8	-3.3	-2.5	-3.0	-2.7
At tropopause (13 km)	-5.7	-5.8	-5.6	-6.0	-4.4	-5.7	-5.6
At surface	-1.9	-1.7	-1.8	-2.3	-1.2	-1.8	-0.7

As atmospheric radiation depends on concentrations of water vapor and atmospheric temperature profile in addition to concentration of carbon dioxide, the effects of change of these parameters on the net fluxes were also investigated in this study. Buehler et al. [4] investigated the effects of large scale changes of water vapor, carbon dioxide and temperature on the longwave atmospheric radiation in tropical reference atmosphere. Five different scenarios were applied: (i) water vapor concentration increased by 20 % throughout the atmosphere keeping concentration of carbon dioxide and temperature constant, (ii) water vapor concentration decreased by 20 % throughout the atmosphere keeping concentration of carbon dioxide and temperature constant, (iii) carbon dioxide concentration increased by 100 % throughout the atmosphere (doubling CO₂ concentration) keeping concentration of water vapor and temperature constant, (iv) temperature increased by 1 K throughout the atmosphere keeping absolute humidity and concentration of carbon dioxide fixed and, (v) temperature increased throughout the atmosphere keeping fixed relative humidity and concentration of carbon dioxide fixed.

In this study, same scenarios were applied by utilizing today's carbon dioxide concentration (383 ppm). Changes in the net fluxes in the atmosphere and the Earth's surface due to changes in the conditions imposed in each scenario are tabulated in Table 5.3. As can be seen from the table, when the water vapor was increased by 20 %, the changes in the net fluxes at three altitudes were all negative implying that the atmosphere became warmer. Water vapor is one of the absorbing emitting gases in the atmosphere. When its concentration is increased, more water vapor molecules absorb the energy emitted from the Earth's surface and therefore more energy in the atmosphere is trapped which leads to warming of the atmosphere. On the other hand, when the water vapor concentration was decreased by 20 %, the changes in the net fluxes throughout the atmosphere were positive as expected. Similar trend was observed when the concentration of carbon dioxide was increased. When comparing the effect of the increasing water vapor concentration with the effect of increasing the carbon dioxide concentration on the warming of the atmosphere, it can be shown that the absolute value of changes in the net flux throughout the atmosphere for increasing water vapor concentration was higher than for increasing carbon dioxide concentration. Therefore, it can be concluded that in tropical atmosphere, 20 %

relative humidity increase has a larger impact on warming of the atmosphere than doubling the carbon dioxide concentration.

When the absolute humidity was kept constant and the temperature was increased, the changes of the net fluxes throughout the atmosphere were all calculated to be positive values due to increased emission of the atmosphere with its increased temperature. However, if the temperature of the atmosphere was increased when keeping the relative humidity constant, the changes in net fluxes were lower than the ones obtained at constant absolute humidity. This is due to the fact that water vapor concentration also increases with increase in temperature in order to keep the relative humidity constant. Therefore, the increased concentration of water vapor in the atmosphere causes more energy to be trapped in the atmosphere leading to warming of the atmosphere. The value of change of net flux at the Earth's surface becomes negative as the concentration of water vapor is much higher closer to the surface. Similar conclusions were withdrawn by Buehler et al. [4].

Table 5.3 Changes in net fluxes (W/m^2) in five different scenarios

Cases	WV +20%	WV -20%	CO₂ x2	T +1K*	T +1K,RHc**
At top of the atmosphere (~ 100 km)	-5.2	6.3	-3.4	4.3	2.6
At tropopause (18 km)	-6.5	5.6	-6.0	3.9	2.1
At surface	-13.1	17.1	-1.4	1.7	-2.6

* keeping absolute humidity, and therefore water vapor concentration profile constant

** keeping fixed relative humidity constant

5.2 MOL Solution of DOM with WBCK

In this study, a previously developed radiation code based on MOL solution of DOM with WBCK model was adapted to a 1-D longwave clear sky atmosphere and its predictive accuracy and computational efficiency was assessed by comparing its predictions with the predictions of LBLRTM. Effect of basic parameters such as spatial discretization (number of grids), order of approximation and number of gray gases were also investigated.

In the MOL solution of DOM with WBCK method, the S_N scheme of Carlson and Lathrop [131] and ROWMAP integration subroutine [138] were utilized as angular quadrature scheme and ODE solver, respectively. The computational parameters related to the ODE solver subroutine are summarized in Appendix B. All simulations were carried out on a personal computer with Pentium M 1.50 GHz processor having 752 Mb of RAM.

Point values of all predicted quantities and the solutions of LBLRTM used for benchmarking purposes and their absolute percentage errors are tabulated and given in Appendix C.

5.2.1 Description of the Physical System

The model was applied to an atmosphere approximated as absorbing-emitting, non-scattering medium containing water vapor and carbon dioxide. The atmosphere was divided into several homogenous layers. For each layer, constant logarithmic mean temperature, pressure and gas concentration were calculated and radiative property of gases were evaluated by using WBCK. The longwave spectral range considered was from 10 to 3000 cm^{-1} which involves 2 wide bands of H_2O (140 and 1600 cm^{-1}) and 4 wide bands of CO_2 (667, 960, 1060 and 2410 cm^{-1}). The model was applied to midlatitude summer reference atmosphere of the AFGL [5]. Water vapor concentration profiles given in the reference atmospheres of AFGL were utilized in this study. Since the water vapor concentration is nearly 0 ppm around 10 km above the Earth's surface as shown in Figure 4.3 and Figure 5.1, the atmosphere is defined as the region extending from the Earth's surface to 10 km in altitude. As the water vapor concentration is influenced by condensation, its

concentration varies with altitude as can be seen in Figure 5.1. Moreover, in addition to water vapor concentration profiles, the profiles of atmospheric temperature and pressure given in the reference midlatitude summer atmosphere of AFGL in the range from 0 km to 10 km, which are illustrated in Figure 5.2, 5.3 respectively, were used. As can be seen from these figures, temperature linearly decreases throughout the atmosphere whereas pressure decreases exponentially. Instead of using reference concentration of carbon dioxide, its today's value which is 383 ppm [149] was used. The emissivity of Earth's surface was taken as unity. It was assumed that there was no incident longwave radiation at the top of the atmosphere.

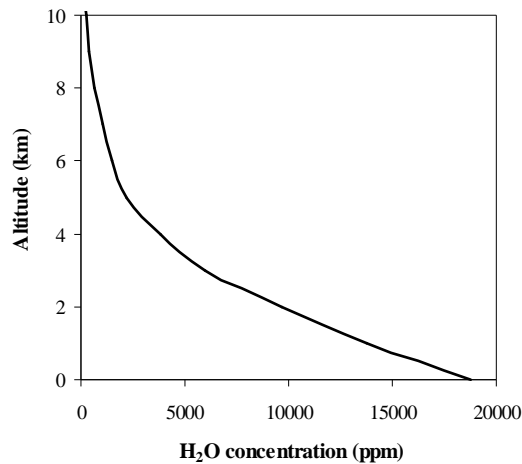


Figure 5.1 Water vapor concentration profile for midlatitude summer atmosphere [5]

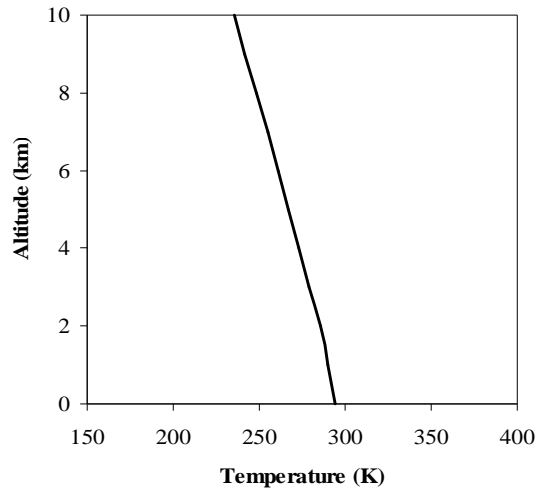


Figure 5.2 Temperature profile for midlatitude summer atmosphere [5]

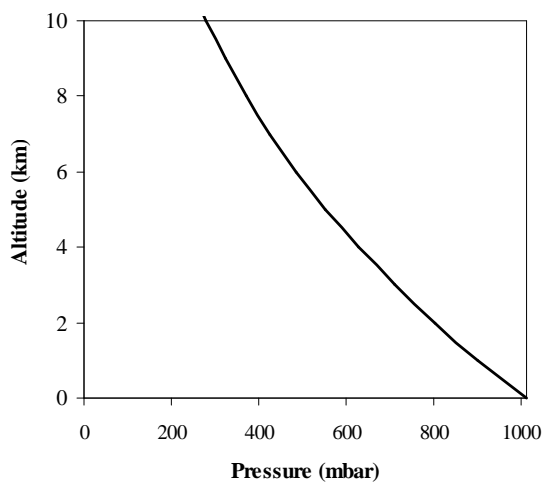


Figure 5.3 Pressure profile for midlatitude summer atmosphere [5]

5.2.2 Effect of Spatial Discretization

In this study, the effect of the number of grid points on the accuracy and the computational economy of the model was investigated. For this purpose, firstly, grids with uniform spacing were employed. During the calculation, S_4 for angular quadrature scheme and three-point upwind differencing scheme for spatial derivative were used.

Figure 5.4 shows the comparison between LBLRTM and MOL solution of DOM with WBCK model predictions of net fluxes in the atmosphere for varying numbers of grids. As can be seen from the figure, when the number of grids is greater than 11 grids, they result in underprediction of the net radiative fluxes in the atmosphere and at the Earth's surface. Moreover, the best results for the net fluxes up to 4 km is obtained when 11 grids are used and above 4 km, using 6 grids results in better agreement with LBLRTM predictions. When the net fluxes calculated towards the top of the atmosphere are compared with the ones obtained closer to the Earth's surface, poorer agreement between the predictions of the model with LBLRTM is observed. This is believed to be due to the fact that correlation parameters used in WBCK model was validated against experimental data for temperatures around 300 K and these parameters may need modifications for cases when temperature is much lower than 300 K.

Maximum and average percentage relative errors in the net flux predictions and corresponding CPU times are tabulated in Table 5.4. As can be seen from the table, as the number of grids increases, maximum and average percentage relative errors and CPU times increase.

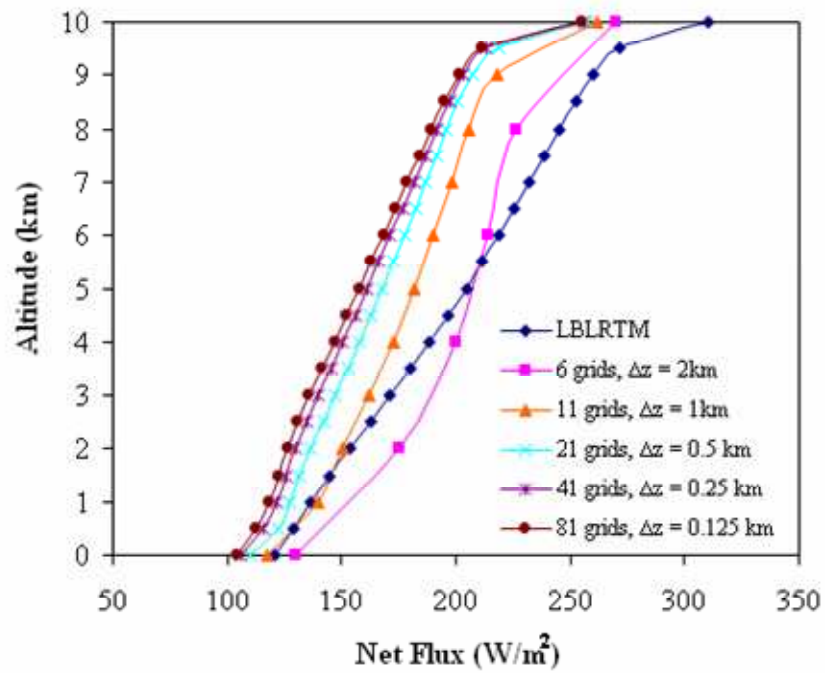


Figure 5.4 Comparison between the net flux predictions of the present study and LBLRTM result for different number of grids with uniform spacing

Table 5.4 Maximum and average percentage relative errors in the net flux predictions of the present study with CPU times for different uniform grids

Number of Grids	Grid spacing, Δz (km)	Max. Abs. % Rel. Error*	Avg. Abs. % Rel. Error	CPU time (sec)
6	2.000	14.0	8.5	6.7
11	1.000	16.4	9.8	9.9
21	0.500	20.5	15.5	22.9
41	0.250	22.0	18.7	48.9
81	0.125	23.1	20.2	131.1

*Absolute percentage relative error = $(|\text{predicted-LBLRTM}| / \text{LBLRTM}) \times 100$

Upon examination of Figure 5.4 and Table 5.4, it can be concluded that use of 11 grids at the lower parts of the atmosphere (below 4 km) and 6 grids at the top part of the atmosphere resulted in better agreement with LBLRTM. Therefore, variable grid spacing should be used in the model. For this purpose, finer grids were utilized for the section of the atmosphere between 0 and 4 km and coarser grids were utilized above 4 km. 3 different grid spacings, summarized in Table 5.5, were tested in the model. During the calculations, three-point upwind differencing scheme was used. However, at the point of transition from finer grid to coarser grid three-point central differencing scheme was applied for spatial discretization.

Table 5.5 Summary of the spacing between grid points

Number of Grids	0-4 km (Δz_1)	4-10 km (Δz_2)
12	0.5 km	2 km
8	1 km	2 km
7	1 km	3 km

The predictions of downwelling, upwelling and net fluxes for 3 cases together with the predictions of LBLRTM are illustrated in Figures 5.5, 5.6 and 5.7, respectively. As can be seen in Figures 5.5 and 5.6, in all three cases, the downwelling and upwelling flux predictions are in good agreement with the predictions of LBLRTM. On the other hand, comparison of net flux predictions with the ones of LBLRTM method shows that the best agreement is achieved when 7 grids are utilized. However, when the maximum percentage relative errors tabulated in Table 5.6 are examined, it is observed that when 7 grids are used, the highest maximum percentage relative error is obtained. Therefore, it can be concluded that the optimum results are obtained when 8 grids are utilized.

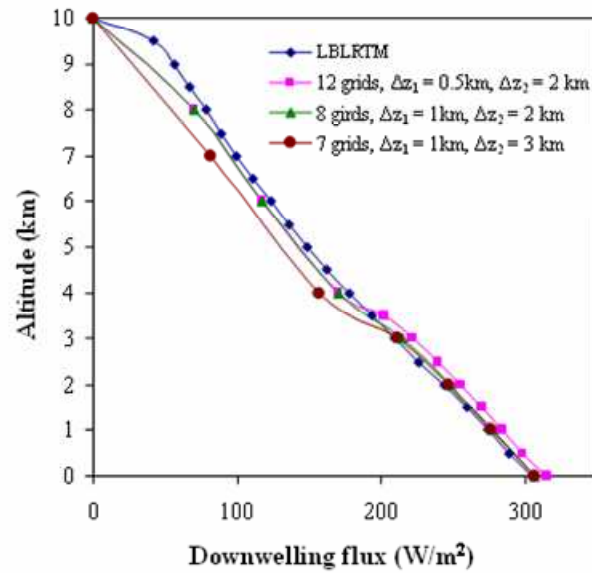


Figure 5.5 Comparison between the downwelling flux predictions of the present study and predictions of LBLRTM for different non-uniform grids

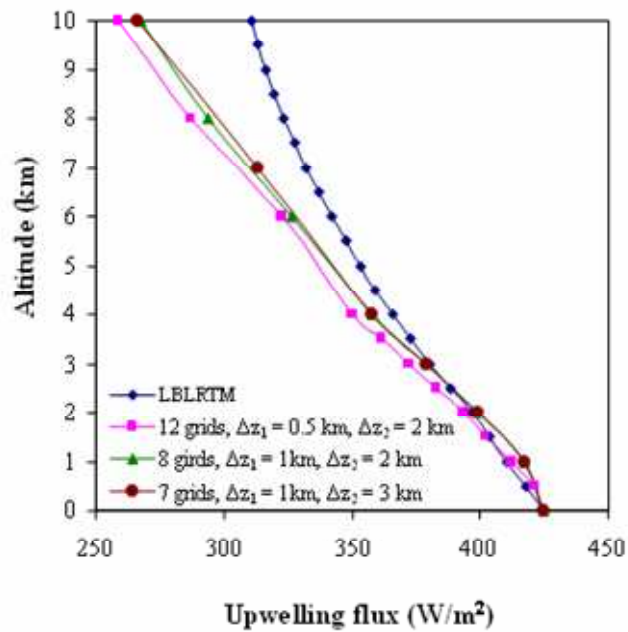


Figure 5.6 Comparison between the upwelling flux predictions of the present study and predictions of LBLRTM for different non-uniform grids

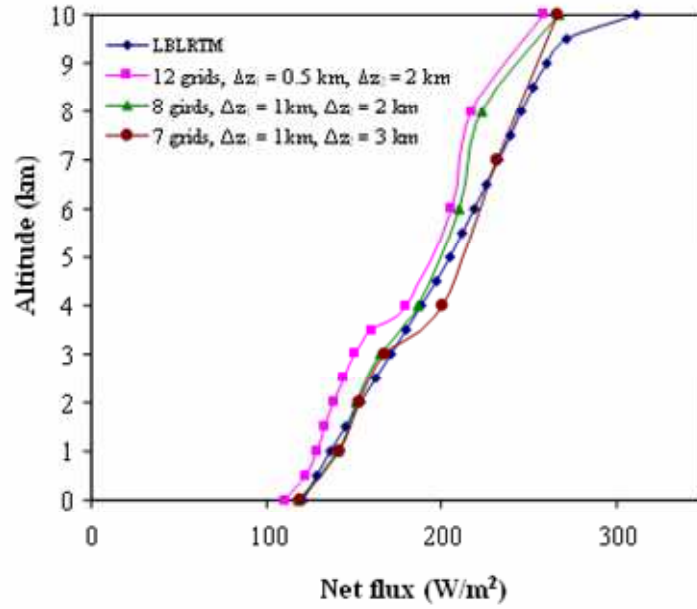


Figure 5.7 Comparison between the net flux predictions of the present study and predictions of LBLRTM for different non-uniform grids

Table 5.6 Maximum and average percentage relative errors in the down flux predictions of the present study with their CPU times for different non-uniform grids

Number of Grids	CPU time (sec)	Max. Abs. % Rel. Error* in Fluxes			Avg. Abs. % Rel. Error in Fluxes		
		Up	Down	Net	Up	Down	Net
12	19.7	16.7	9.7	16.7	3.9	5.0	9.3
8	12.3	13.9	9.7	13.9	4.1	3.6	4.8
7	7.8	14.3	17.9	14.3	3.6	5.5	4.1

*Absolute % relative error = $(|\text{predicted-LBLRTM}| / \text{LBLRTM}) \times 100$

Instead of manually changing the grid spacings, a grid generator was also utilized in this study. Detailed description of the grid generator can be found in Appendix D. Grid generation subroutine leads to variable grid size which is more clustered to the lower boundary of the system under consideration. In the calculations, S_4 for angular quadrature scheme and two-point upwind differencing scheme for spatial discretization were used. In an attempt to see the effect of grid spacing on flux predictions, 7 grid points with 4 different grid size weights, az , were utilized. The spacings of grids developed by grid generation are listed in Table 5.7. As can be seen from the table, as az decreases, grid spacing decreases at the bottom section of the atmosphere but increases towards the top. When $az = 0.5$, equally spaced grids are obtained.

Table 5.7 The spacing of non-uniform grids developed by grid generation

Grid Points	Altitude (km)			
	$az = 0.25$	$az = 0.4$	$az = 0.45$	$az = 0.5$
7	10.00	10.00	10.00	10.00
6	6.94	7.78	8.06	8.33
5	4.44	5.78	6.22	6.67
4	2.50	4.00	4.50	5.00
3	1.11	2.44	2.89	3.33
2	0.28	1.11	1.39	1.67
1	0.00	0.00	0.00	0.00

The downwelling, upwelling and net fluxes calculated when different az values were used in grid generator are compared with the predictions of LBLRTM in Figures 5.8, 5.9 and 5.10, respectively. As illustrated in these figures, the effect of az on the flux predictions is not significant. When maximum and average percentage relative errors in net fluxes tabulated in Table 5.8 are examined, it is seen that

accuracy increases as az decreases in the expense of CPU time. However, as az decreases the errors in downwelling fluxes increase, whereas errors in upwelling fluxes decrease. It is observed that maximum absolute percentage relative error in downwelling flux prediction for $az = 0.25$ is much higher than the others. Therefore, it can be concluded that the optimum results can be obtained with $az = 0.4$.

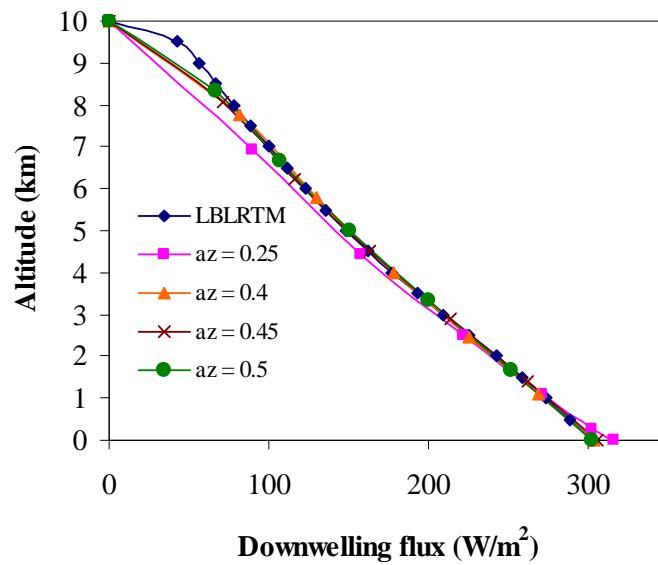


Figure 5.8 Comparison between the downwelling flux predictions of the present study and predictions of LBLRTM for different grid size weights (az)

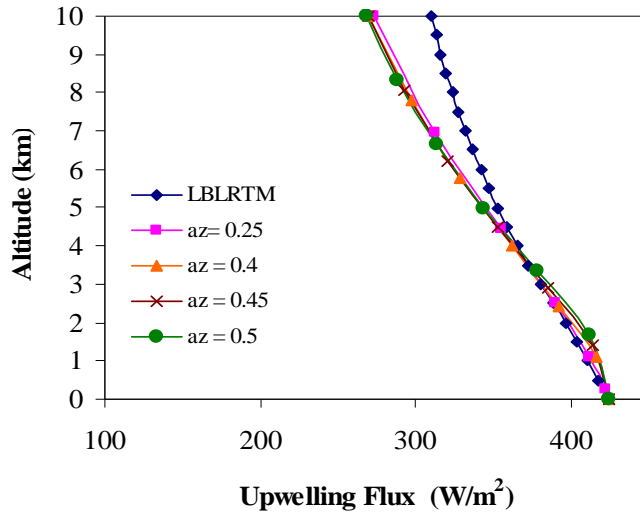


Figure 5.9 Comparison between the upwelling flux predictions of the present study and predictions of LBLRTM for different grid size weights (az)

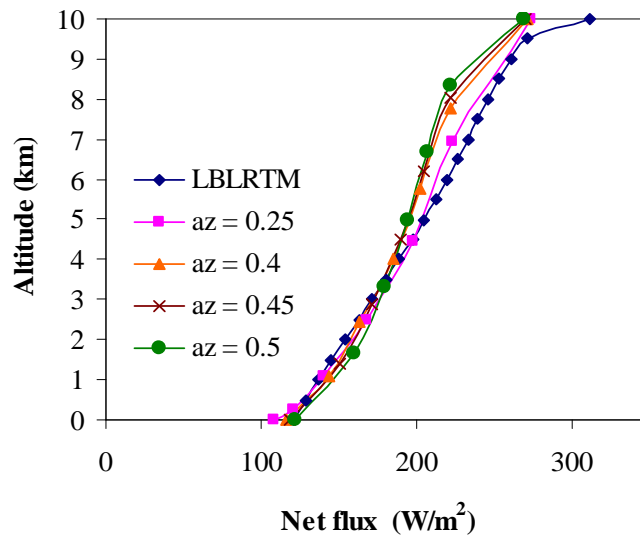


Figure 5.10 Comparison between the net flux predictions of the present study and predictions of LBLRTM for different grid size weights (az)

Table 5.8 Maximum and average percentage relative errors in the flux predictions of the present study with their CPU times for different grid size weights (az)

Grid Size Weights (az)	CPU time (sec)	Max. Abs. % Rel. Error* in Fluxes			Avg. Abs. % Rel. Error in Fluxes		
		Upwelling	Downwelling	Net	Upwelling	Downwelling	Net
		0.25	13.56	11.7	11.4	11.9	3.1
0.40	10.76	13.0	6.5	13.0	4.4	2.5	5.3
0.45	9.97	13.2	5.0	13.2	4.9	1.7	6.1
0.50	8.80	13.5	3.4	13.5	5.3	1.0	6.9

*Absolute % relative error = $(|\text{predicted-LBLRTM}| / \text{LBLRTM}) \times 100$

When the relative errors in fluxes tabulated in 5.5, 5.7 and 5.9 are compared, it can be concluded that variable grid size should be utilized instead of uniform grid size. Moreover, the maximum and average absolute percentage relative errors are in the same order of magnitude when 8 grids with two different grid spacings ($\Delta z_1 = 1$ km and $\Delta z_2 = 2$ km) and 7 grids obtained by using grid generator with $az = 0.4$ are used. On the other hand, lower maximum relative errors are obtained especially in downwelling fluxes when the grid generator is employed. Moreover, utilization of the grid generator also decreases CPU time. In conclusion, optimum results can be obtained when the grid generator with $az = 0.4$ is utilized. Therefore, this grid spacing was utilized in the rest of this thesis study.

5.2.3 Effect of Order of Approximation

Table 5.9 shows the maximum and average percentage relative errors in the flux predictions of the present study with their CPU times for 4 different order of approximations. As can be seen from the table, CPU time increases with order of approximation, as expected. The maximum absolute relative errors in upwelling and net flux predictions of this study decrease with increasing order of approximation whereas error in the downwelling flux predictions increases with increasing order of approximation. When the absolute percentage relative errors in the flux predictions are considered, they are nearly the same but the error in net flux prediction for S_2

approximation is slightly higher than the others. Therefore, S_4 was utilized in the rest of this thesis study.

Table 5.9 Maximum and average percentage relative errors in the flux predictions of the present study with their CPU times for different order of approximation

Order of Approximation	CPU time (sec)	Max. Abs. % Rel. Error* in Fluxes			Avg. Abs. % Rel. Error in Fluxes		
		Up	Down	Net	Up	Down	Net
S_2	2.90	13.8	3.4	13.8	4.7	2.3	6.6
S_4	10.76	13.0	6.5	13.0	4.4	2.5	5.3
S_6	25.42	12.9	7.1	12.9	4.3	2.6	5.2
S_8	45.02	12.9	7.3	12.9	4.3	2.6	5.2

*Absolute % relative error = $(|\text{predicted-LBLRTM}| / \text{LBLRTM}) \times 100$

5.2.4 Effect of Number of Gray Gases

The effect of number of gray gases on the accuracy of flux predictions are summarized in Table 5.10. As can be seen in the table, the use of higher number of gray gases does not improve the accuracy significantly. Therefore, 10 gray gases were used in the rest of this study.

Table 5.10 Maximum and average percentage relative errors in the flux predictions of the present study with their CPU times for several numbers of gray gases

Number of Gray Gases	CPU time (sec)	Max. Abs. % Rel. Error* in Fluxes			Avg. Abs. % Rel. Error in Fluxes		
		Up	Down	Net	Up	Down	Net
		10	10.76	13.0	6.5	13.0	4.4
15	14.70	12.8	6.3	12.8	4.5	2.6	5.8
20	21.43	11.8	6.5	11.8	4.2	2.4	5.4
30	36.12	11.5	6.4	11.5	4.2	2.5	5.5

*Absolute % relative error = $(|\text{predicted-LBLRTM}| / \text{LBLRTM}) \times 100$

5.3 Radiative-Convective Model

In this study, the radiative-convective model in conjunction with a radiation model based on MOL solution of DOM with WBCK was applied to 1-D clear sky atmosphere. In addition, the predictions when the governing equations of radiative-convective model and the radiative transfer equation are solved simultaneously were compared with the ones obtained when radiative-convective model and the radiation model are coupled at different coupling intervals. The detailed information of the system under consideration is given in Chapter 3. In addition to this information, in the model, considering the conclusions reached in section 5.2, 10 gray gases, S_4 as order of approximation and 7 grids with the grid size weight, $az = 0.4$ were used. The model was executed for a period of approximately 1.5 days (40 hours). The computational parameters related to the ODE solver subroutine, ROWMAP, are summarized in Appendix B.

Figures 5.11, 5.12 and 5.13 demonstrate changes in temperature predictions during 40 hours period at the surface, at 4 km above the surface and at the top of the atmosphere, respectively. Point values of temperature are tabulated and given in Appendix E. The effect of coupling intervals on temperature predictions is also illustrated.

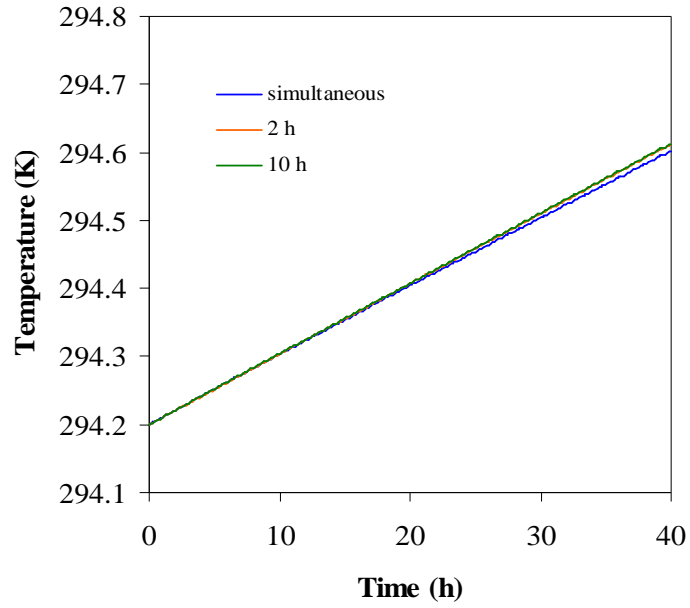


Figure 5.11 Comparison between the change in surface temperature for different coupling interval and simultaneous solution.

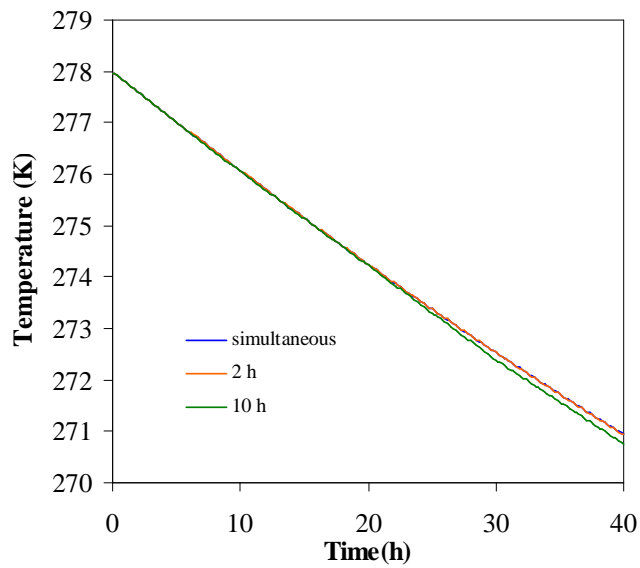


Figure 5.12 Comparison between the change in temperature at 4 km above the surface for different coupling interval and simultaneous solution.

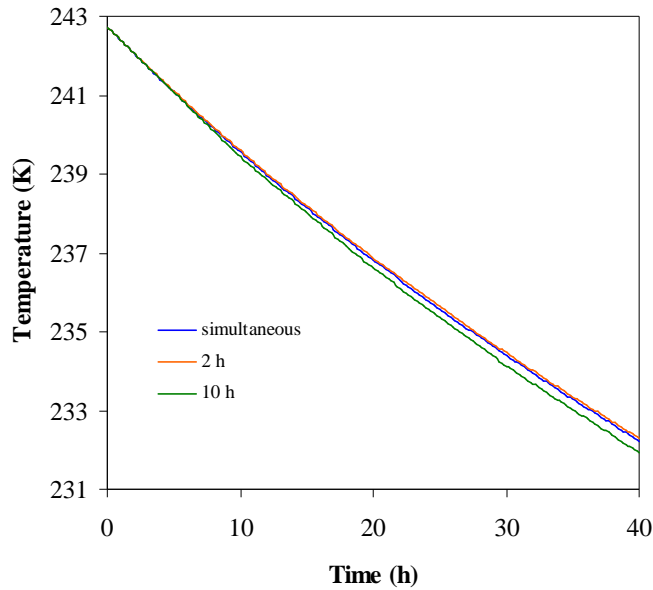


Figure 5.13 Comparison between the change in temperature at top of the atmosphere for different coupling interval and simultaneous solution

As can be seen in these figures, during the short time period of 40 hours, it is not possible to see a significant effect of coupling interval on temperature profiles. However, it can be observed that as time progress, the temperature profiles diverge from the one obtained from simultaneous solution. To further investigate the effect of coupling interval on temperature predictions, the absolute percentage relative errors were evaluated based on the result of the simultaneous solution and are tabulated in Table 5.11. As can be seen from the table, when time progresses, the absolute percentage relative error increases. Moreover, errors obtained with the coupling interval of 10 hours are higher than those obtained with coupling interval of 2 hours. It can be inferred from this observation that when climate model is run for longer periods of time, coupling instead of simultaneous solution will result in erroneous solutions. Generally, climate models are executed for periods in the order of years to be able to take into consideration the different response times of sub-systems such as

atmosphere, ocean, land etc. In this study, only a simple climate model was utilized and the execution period was considerably short, i.e. 40 hours. If the other sub-systems were to be included and the execution time was to be extended, it is believed that the effect of coupling interval on the accuracy of the temperature predictions would have been more significant.

Table 5.11 Average percentage relative errors in the temperature predictions of the present study for two different coupling intervals

Absolute % Rel. Error in temperature*	Coupling Interval	Time (h)				
		0	10	20	30	40
at the surface	2 hours	0.000	0.000	0.001	0.002	0.003
	10 hours	0.000	0.000	0.001	0.002	0.004
at 4 km above the surface	2 hours	0.000	0.002	0.001	0.004	0.004
	10 hours	0.000	0.008	0.007	0.053	0.067
at the top of atmosphere	2 hours	0.000	0.016	0.024	0.025	0.029
	10 hours	0.000	0.053	0.090	0.117	0.131

*Absolute percentage relative error = $(|\text{coupling-simultaneous}| / \text{simultaneous}) \times 100$

Furthermore, in the execution of the climate model, another important and restraining parameter is the computation time of the program. As can be seen in Table 5.12, the computation time increases as coupling interval decreases, as expected. However, one very important observation is that simultaneous solution of the governing equation of the radiative-convective model and the radiation model using the same solution method does not bring an extra burden to the computational economy of the model. On the contrary, the simultaneous solution results in more accurate results in a computationally efficient way.

Table 5.12 Computational times for different coupling interval

Coupling interval	CPU time (sec)
Simultaneous	29.6
2 h	38.4
10 h	12.6

CHAPTER 6

CONCLUSIONS

Climate models are the primary tools used for understanding past climate variations and for future projections. The atmospheric radiation is the key component of these models. Therefore, atmospheric radiation models were developed in isolation from the climate models. The simplest radiation models are based on the assumption of 1-D clear sky atmosphere for which radiative transfer equation (RTE) is solved analytically. In this study, a 1-D clear sky atmosphere model was used to determine the effects of carbon dioxide, water vapor and temperature on the fluxes in the atmosphere and the surface of the earth by using the most accurate line-by-line model for radiative property estimation and analytical solution of RTE. The effect of carbon dioxide concentration doubling was studied in both midlatitude summer and tropical scenarios and the effect of water vapor concentration through relative humidity increase and temperature increase in the atmosphere were investigated in tropical scenario to be able to benchmark the solutions against the literature data. Results show that in tropical scenario, 20 % relative humidity increase has a larger impact on warming of the atmosphere than doubling the carbon dioxide concentration. Furthermore, the effect of 1K temperature rise under fixed relative humidity condition results in higher impact on warming compared to the same temperature rise under fixed absolute humidity condition due to water vapor feedback. In addition, all the results were found to be in complete agreement with literature findings.

As accurate modeling of atmosphere necessitates reliable evaluation of the medium radiative properties and accurate solution of the radiative transfer equation in conjunction with the time-dependent multi-dimensional governing equations of atmospheric models, a radiative-convective model with a radiation model was

developed. For this purpose, a previously developed radiation model based on MOL solution of DOM with WCK model was adapted to 1-D longwave clear sky atmosphere and its predictive accuracy and computational efficiency was examined on the test problem by using benchmark solution obtained from LBLRTM. Reasonable agreement between the predictions of the model and the LBLRTM was observed. A parametric study was also carried out to find the optimum grid structure, order of approximation of the DOM and the number of gray gases which will provide accurate and at the same time computationally efficient solutions. For the problem under consideration, accurate and computationally efficient results were obtained when a non-uniform grid structure with 7 grids, S_4 approximation and 10 gray gases were utilized.

Having validated the predictions of the model and selecting the optimum parameters, the radiation model was then coupled with radiative-convective model and the predictive accuracy of this model was examined for several coupling intervals. These predictions were then compared with the ones obtained when equations of radiative-convective model and the radiation model are solved simultaneously. Comparisons reveal that as coupling interval increases, although the computation time of the model decreases, the accuracy of the predictions decreases. Moreover, percentage relative error in temperature increases an order of magnitude when coupling time between radiative-convective model and the radiation model increases from 2 to 10 hours. Therefore, it can be concluded that the equations of the radiation model have to be solved simultaneously with the equations of the climate model. Overall evaluation of the performance of the radiation model used in this study points out that it provides accurate and computationally efficient solutions and can be used with confidence in conjunction with the climate models for simultaneous solution of governing equations with radiation transfer equation.

6.1 Suggestions for Future Work

Based on the experience gained in this study, the following recommendations for future extension of the work are suggested:

- Modification of the code for the treatment of absorbing-emitting-scattering atmosphere containing clouds and aerosols is required.

- Radiation code based on MOL solution of DOM can be coupled with climate model based on the same approach.
- Correlation parameters used in WBCK model can be modified for cases when temperature is much lower than 300 K.

REFERENCES

1. Solomon, S., D. Qin, M. Manning, Z. Chen, M. Marquis, K.B. Averyt, M. Tignor and H.L. Miller (eds.), *IPCC, 2007: Climate Change 2007: The Physical Science Basis. Contribution of Working Group I to the Fourth Assessment Report of the Intergovernmental Panel on Climate Change*, Cambridge University Press, Cambridge, United Kingdom and New York, NY, USA, 2007.
2. Houghton, J.T., Y. Ding, D. J. Griggs, M. Noguer, P. J. van der Linden, and D. Xiaosu, *Climate Change 2001: The Scientific Basis Contribution of Working Group I to the Third Assessment Report of the Intergovernmental Panel on Climate Change (IPCC)*, Cambridge University Press, 2001.
3. Brindley, H.E., and J.E. Harries, "The impact of far i.r. absorption on clear sky greenhouse forcing: sensitivity studies at high spectral resolution", *Journal of Quantitative Spectroscopy & Radiative Transfer*, Vol **60**(2) pp. 151-180,1998.
4. Buehler, S.A., A. V. Engeln, E. Brocard, V.O. John, T Kuhn, and P. Eriksson, "Recent developments in the line-by-line modeling of outgoing longwave radiation", *Journal of Quantitative Spectroscopy & Radiative Transfer*, Vol **98** pp. 446-457,2006.
5. McClatchey, R.A., R.W. Fenn, J.E.A. Selby, F.E. Volz, and J.S. Garing, *Optical properties of the atmosphere*, AFCRL-72-0497, Air Force Cambridge Res. Lab., Bedford,Mass., 1972.
6. Mlawer, E.J., S.J. Taubman, P.D. Brown, M.J. Iacono, and S.A. Clough, "Radiative transfer for inhomogeneous atmospheres: RRTM, a validated correlated-k model for the longwave ", *Journal of Geophysical Research-Atmospheres*, Vol **102**(D14) pp. 16663-16682,1997.
7. Clough, S.A., and M.J. Iacono, "Line-by-line calculation of atmospheric fluxes and cooling rates 2. Application to carbon dioxide, ozone, methane, nitrous oxide and halocarbons", *Journal of Geophysical Research-Atmospheres*, Vol **100**(D8) pp. 16,519-16,535,1995.
8. Feigelson, E.M., B.A. Fomin, I.A. Gorchakova, E.V. Rozanov, Y.M. Timofeyev, A.N. Trotsenko, and M.D. Schwarzkopf, "Calculation of longwave radiation fluxes in atmospheres", *Journal of Geophysical Research-Atmospheres*, Vol **96**(D5) pp. 8985-9001,1991.
9. Morcrette, J.J., "Radiation and cloud radiative properties in the European Centre for Medium Range Weather Forecasts Forecasting System", *Journal of Geophysical Research*, Vol **96** pp. 9121-9132,1991.

10. Ridgway, W.L., Harshvardhan, and A. Arking, "Computation of atmospheric cooling rates by exact and approximate methods", *Journal of Geophysical Research-Atmospheres*, Vol **96**(D5) pp. 8969-8984,1991.
11. Rothman, L.S., R.R. Gamache, R.H. Tipping, C.P. Rinsland, M.A.H. Smith, D.C. Benner, V.M. Devi, J.M. Flaud, C. Camypeyret, A. Perrin, A. Goldman, S.T. Massie, L.R. Brown, and R.A. Toth, "The HITRAN molecular database - editions of 1991 and 1992 ", *Journal of Quantitative Spectroscopy & Radiative Transfer*, Vol **48**(5-6) pp. 469-507,1992.
12. Rothman, L.S., "Atmospheric absorption line parameters compilation: 1980 version", *Applied Optics*, Vol **20** pp. 791-795,1981.
13. Dave, J.V., "A direct solution of the spherical harmonics approximation to the radiative transfer equation for an arbitrary solar elevation. Part I: Theory", *Journal of Atmospheric Science*, Vol **32** pp. 790-798,1975.
14. Evans, K.F., "Two-dimensional radiative transfer in cloudy atmospheres: The spherical harmonics spatial grid method", *Journal of Atmospheric Science*, Vol **50**(18) pp. 3111-3124,1993.
15. Evans, K.F., "The spherical harmonics discrete ordinate method for three-dimensional atmospheric radiative transfer", *Journal of Atmospheric Science*, Vol **55** pp. 429-446,1998.
16. Evans, K.F., "SHDOMPPDA: A radiative transfer model for cloudy sky data assimilation", *Journal of Atmospheric Science*, Vol **64** pp. 3854-3864,2006.
17. Marchuk, G., G. Mikhailov, M. Nazaraliev, R. Darbinjan, B. Kargin, and B. Elepov, *The Monte Carlo Methods in Atmospheric Optics*, Springer, Verlag, 1980.
18. Cahalan, R.F., W. Ridgway, W.J. Wiscombe, S. Gollmer, and Harshvardhan, "Independent pixel and Monte Carlo estimates of stratocumulus Albedo", *Journal of Atmospheric Science*, Vol **51**(24) pp. 3776-3790,1994.
19. O'Hirok, W., and C. Gautier, "A three-dimensional radiative transfer model to investigate the solar radiation within a cloudy atmosphere. Part I: Spatial effect", *Journal of Atmospheric Science*, Vol **55**(2162-2179) pp. 1997.
20. Maruyama, S., and T. Aihara, "Radiation heat transfer of arbitrary three-dimensional absorbing, emitting and scattering media and specular and diffuse surfaces", *Journal of Heat Transfer-Transactions of THE ASME*, Vol **119** pp. 129-136,1997.
21. Maruyama, S., "Radiative heat transfer in anisotropic scattering media with specular boundary subjected to collimated irradiation", *International Journal of Heat and Mass Transfer*, Vol **41** pp. 2847-2856,1998.
22. Maruyama S., K.M., and Z. Guo. "Effects of droplets parameters on thermal protection by water mist against intense irradiation", *Proceedings of NHTC'00*, NHTC2000-12265. 2000.
23. Maruyama, S., Y. Takeuchi, S. Sakai, and Z. Guo, "Improvement of computational time in radiative heat transfer of three-dimensional

- participating media using the radiation element method." *Journal of Quantitative Spectroscopy & Radiative Transfer*, Vol **73** pp. 239-248,2002.
24. Nishikawa, T., S. Maruyama, and S. Sakai, "Radiative heat transfer analysis within three-dimensional cloud subjected to solar and sky irradiation", *Journal of Atmospheric Science*, Vol **61** pp. 3125-3133,2004.
 25. Sakurai, A., S. Maruyama, S. Sakai, and T. Nishikawa, "The effect of three-dimensional radiative heat transfer in cloud fields using the radiation element method", *Journal of Quantitative Spectroscopy & Radiative Transfer*, Vol **93** pp. 79-87,2005.
 26. Selçuk, N., and N. Kayakol, "Evaluation of Discrete Ordinates Method for Radiative Transfer in Rectangular Furnaces", *International Journal of Heat and Mass Transfer*, Vol **40** pp. 213-222,1997.
 27. Piotrowski, S., "Asymptotic case of the diffusion of light through an optically thick scattering layer", *Acta Astronomica*, Vol **6** pp. 61-73,1956.
 28. Samuelson, R.E., "The thermal radiation field emitted by anisotropically scattering cloudy planetary atmospheres", *Icarus*, Vol **10** pp. 258-273,1969.
 29. Yamamoto, G., and S. Asano, "Radiative heat transfer in water clouds by infrared radiation ", *Journal of Quantitative Spectroscopy & Radiative Transfer*, Vol **11** pp. 697-708,1971.
 30. Liou, K.N., "A numerical experiment on Chandrasekhar's discrete ordinate method for radiative transfer: Applications to cloudy and hazy atmospheres", *Journal of Atmospheric Science*, Vol **30** pp. 1303-1326,1973.
 31. Liou, K.N., "Analytic two-stream and four-stream solutions for radiative transfer", *Journal of Atmospheric Science*, Vol **31** pp. 1473-1475,1974.
 32. Liou, K.N., "Applications of the discrete ordinate method for radiative transfer to inhomogeneous aerosol atmospheres ", *Journal of Geophysical Research*, Vol **80** pp. 3434-3440,1975.
 33. Liou, K.N., K.P. Freeman, and T. Sasamori, "Cloud and aerosol effects on the solar heating rate of the atmosphere ", *Tellus*, Vol **30** pp. 62-70,1978.
 34. Stamnes, K., and R.A. Swanson, "A new look at the discrete ordinate method for radiative transfer calculations in anisotropically scattering atmosphere", *Journal of Atmospheric Science*, Vol **38** pp. 387-399,1981.
 35. Stamnes, K., and H. Dale, "A new look at the discrete ordinate method for radiative transfer calculations in anisotropically scattering atmospheres. II: Intensity computations", *Journal of Atmospheric Science*, Vol **38** pp. 2696-2706,1981.
 36. Stamnes, K., and P. Conklin, "A new multi-layer discrete ordinate approach to radiative transfer in vertically in homogeneous atmosphere", *Journal of Quantitative Spectroscopy & Radiative Transfer*, Vol **31**(3) pp. 273-282,1984.
 37. Stamnes, K., S.C. Tsay, W. Wiscombe, and K. Jayaweera, "Numerically stable algorithm for discrete ordinate method radiative transfer in multiple

- scattering and emitting layered media", *Applied Optics*, Vol **27**(12) pp. 2502-2509,1988.
38. Zorzano M.P., A.M.M., and L. Vazquez, "Numerical integration of the discrete ordinate radiative transfer equation in strongly non-homogeneous media", *Applied Mathematics and Computation*, Vol **164** pp. 263-274,2005.
 39. Gerstl, S.A.W., and A. Zardecki, "Discrete ordinates finite element method for atmospheric radiative transfer and remote sensing", *Applied Optics*, Vol **24** pp. 81-93,1985.
 40. Sanchez, A., T.F. Smith, and W.F. Krajewski, "A three-dimensional atmospheric radiative transfer model based on the discrete ordinates method", *Atmospheric Research*, Vol **33** pp. 283-308,1994.
 41. Li, H.S., G. Flamant, and J.D. Lu, "A new discrete ordinate algorithm for computing radiative transfer in one-dimensional atmospheres", *Journal of Quantitative Spectroscopy & Radiative Transfer*, Vol **83** pp. 407-421,2004.
 42. McGuffie, K., *A climate modelling primer*, 3rd ed, J. Wiley, Chichester, West Sussex; Hoboken, N.J., 2005.
 43. Morcrette, J.J., "On the effects of the temporal and spatial sampling of radiation fields on the ECMWF forecasts and analyses", *Monthly Weather Review*, Vol **128** pp. 876-887,1999.
 44. Venema, V., A. Schomburg, F. Ament, and C. Simmer, "Two adaptive radiative transfer schemes for numerical weather prediction models", *Atmospheric Chemistry and Physics*, Vol **7** pp. 5659-5674,2007.
 45. Yucel, A. "Solution of the Discrete Ordinates Equations for a Radiatively Participating Medium by the Method of Lines", *Proc. of Advances in Computer Methods for Partial Differential Equations VII*, New Brunswick: IMACS, 1992.
 46. Selçuk, N., G. Kırbaş, and T. Tarhan. "Evaluation of Method of Lines Solution of Discrete Ordinates Method and Finite Volume Method in a Planar Medium", *Proc. of International Conference on Computational Heat and Mass Transfer*, Gazimağusa, Northern Cyprus, Eastern Mediterranean University Printing House, 1999.
 47. Selçuk, N., and G. Kırbaş, "The Method of Lines Solution of the Discrete Ordinates Method for Radiative Heat Transfer in Enclosures", *Numerical Heat Transfer Part B-Fundamentals*, Vol **37**(379-392) pp. 2000.
 48. Selçuk, N., A. Batu, and I. Ayrancı, "Performance of Method of Lines Solution of Discrete Ordinates Method in the Freeboard of a Bubbling Fluidized Bed Combustor", *Journal of Quantitative Spectroscopy and Radiative Transfer*, Vol **73** pp. 503-516,2002.
 49. Kırbaş, G., The Method of Lines Solution of Discrete Ordinates Method for Radiative Heat Transfer in Enclosure, M.Sc. Thesis, Middle East Technical University, Turkey, 1999.

50. Ayrancı, I., The Method of Lines Solution of Discrete Ordinates Method for Radiative Heat Transfer in 3-D Enclosures Containing Scattering Media, M. Sc. Thesis, Middle East Technical University, Turkey, 2001.
51. Ayrancı, I., and N. Selçuk, "MOL Solution of DOM for Radiative Transfer in 3-D Scattering Media", *Journal of Quantitative Spectroscopy and Radiative Transfer*, Vol **84** pp. 409-422,2004.
52. Harmandar, S., and N. Selçuk, "The Method of Lines Solution of the Discrete Ordinates Method for Radiative Heat Transfer in Cylindrical Enclosures", *Journal of Quantitative Spectroscopy and Radiative Transfer*, Vol **84**(4) pp. 395-407,2004.
53. Çayan, F.N., The method of lines solution of discrete ordinates method for nongray media, M.Sc. Thesis, Middle East Technical University, Turkey, 2006.
54. Edwards, D.P., *GENLN2: A general line-by-line atmospheric transmittance and radiance model*, NCAR /TN-367+STR, National Center for Atmospheric Research, Colorado, 1992.
55. Goody, R.M., "A statistical model for water vapor absorption", *Quarterly Journal of the Royal Meteorological Society*, Vol **78** pp. 165-169,1952.
56. Malkmus, W., "Random Lorentz band model with exponential-tailed S^{-1} line-intensity distribution function", *Journal of the Optical Society of America*, Vol **57** pp. 323-329,1967.
57. Goody, R.M. and Y.L., Yung, *Atmospheric Radiation*, Clarendon Press, Oxford, 1989.
58. Curtis, A.R. "The computation of radiative heating rates in the atmosphere", *Proceedings of the Royal Society of London Series A-Mathematical and Physical Sciences* 236, 1956.
59. Rodgers, C.D., *The radiative heat budget of the troposphere and lower stratosphere*, Rep. A2, Mass. Inst. of Technol., Cambridge, 1967.
60. Fels, S.B., and D. Schwarzkopf, "An efficient, accurate algorithm for calculating CO₂ 15- μ -m band cooling rates", *Journal of Geophysical Research*, Vol **86** pp. 1205-1232,1981.
61. Chou, M.D., and A. Arkin, "An efficient method for computing the absorption of solar radiation by water vapor", *Journal of Atmospheric Science*, Vol **38** pp. 708-807,1981.
62. Chou, M.D., and L. Peng, "A parameterization of the absorption in the 15- μ -m CO₂ spectral region with application to climate studies", *Journal of Atmospheric Science*, Vol **40** pp. 2183-2192,1983.
63. Arking, A., and K. Grossman, "Influence of line shape and band-structure on temperatures in planetary atmospheres", *Journal of Atmospheric Science*, Vol **29** pp. 937-949,1972.
64. Domoto, G.A., "Frequency integration for radiative-transfer problems involving homogeneous non-gray gases-inverse transmission function",

- Journal of Quantitative Spectroscopy & Radiative Transfer*, Vol **14** pp. 935-942,1974.
65. Wang, W.C., and G.Y. Shi, "Total band absorptance and k-distribution function for atmospheric gases", *Journal of Quantitative Spectroscopy & Radiative Transfer*, Vol **39** pp. 287-297,1988.
 66. Lacis, A.A., and J.E. Hansen, "Parameterization for absorption of solar radiation in Earth's atmosphere", *Journal of Atmospheric Science*, Vol **31** pp. 118-133,1974.
 67. Chou, M.D., and A. Arkin, "Computation of infrared cooling rates in the H₂O bands", *Journal of Atmospheric Science*, Vol **37** pp. 855-867,1980.
 68. Shi, G.Y., "The cooling rate due to 9.6- μ m ozone band- a new approximation", *Scientia Sinica Series B-Chemical Biological Agricultural Medical & Earth Sciences*, Vol **27** pp. 947-957,1984.
 69. Godsalve, C., "Distributions for the exponential band model", *Applied Optics*, Vol **40**(9) pp. 1559-1562,2001.
 70. Fu, Q., and K. Liou, "On the correlated k-distribution method for radiative transfer in nonhomogeneous atmosphere", *Journal of Atmospheric Science*, Vol **49** pp. 2139-2156,1992.
 71. Lacis, A., W.C. Wang, and J. Hansen. "Correlated k-distribution method for radiative transfer in climate modes: Application to effect of cirrus clouds on climate", NASA Conf. Publ. 2076, 1979.
 72. Goody, R., R. West, L. Chen, and D. Crisp, "The correlated-k method for radiation calculations in homogeneous atmospheres", *Journal of Quantitative Spectroscopy & Radiative Transfer*, Vol **42**(6) pp. 539-550,1989.
 73. Lacis, A.A., and V. Oinas, "A description of the correlated k distribution method for modeling nongray gaseous absorption, thermal emission, and multiple scattering vertically inhomogeneous atmospheres", *Journal of Geophysical Research*, Vol **96**(D5) pp. 9027-9063,1991.
 74. Marin, O., and R.O. Buckius, "Wideband Correlated-k Method Applied to Absorbing, Emitting and Scattering Media", *Journal of Thermophysics and Heat Transfer*, Vol **10** pp. 364-371,1996.
 75. Parthasarathy, G., J.C. Chai, and S.V. Patankar, "A Simple Approach to Non-Grey Gas Modelling", *Numerical Heat Transfer Part B-Fundamentals*, Vol **29** pp. 113-123,1996.
 76. Denison, M.K., and W.A. Fiveland, "A Correlation for the Reordered Wave Number of the Wide-Band Absorptance of Radiating Gases", *ASME Journal of Heat Transfer*, Vol **119** pp. 853-856,1997.
 77. Lee, P.Y.C., K.G.T. Hollands, and G.D. Raithby, "Reordering the Absorption Coefficient within the Wide Band for Predicting Gaseous Radiant Exchange", *ASME Journal of Heat Transfer*, Vol **118** pp. 394-400,1996.
 78. Ströhle, J., and P.J.Coelho, "On the Application of the Exponential Wide Band Model to the Calculation of Radiative Heat Transfer in One- and Two-

- Dimensional Enclosures", *International Journal of Heat and Mass Transfer*, Vol **45** pp. 2129-2139,2002.
79. Çayan F.N., and N. Selçuk, "A comparative study of modeling of radiative heat transfer using MOL solution of DOM with grey gas, wide band correlated-k and spectral line-based weighted sum of grey gases models", *Numerical Heat Transfer Part B-Fundamentals*, Vol **52**(3) pp. 281-296,2007.
 80. Çayan F.N., and N. Selçuk, "The method of lines solution of discrete ordinates method for non grey media", *Journal of Quantitative Spectroscopy and Radiative Transfer*, Vol **104** pp. 228-237,2007.
 81. Clough, S.A., M.J. Iacono, and J.L. Moncet, "Line-By-Line calculations of atmospheric fluxes and cooling rates - application to water-vapor", *Journal of Geophysical Research-Atmospheres*, Vol **97**(D14) pp. 15761-15785,1992.
 82. Encyclopædia Britannica, <http://www.britannica.com/eb/article-9110147>, last accessed date: 15/12/ 2007
 83. Encyclopædia Britannica, <http://www.britannica.com/eb/article-9117439>, last accessed date: 15/12/ 2007
 84. Tarbuck, E.J., and F.K. Lutgens, *Earth science*, 10th ed,Prentice Hall, Upper Saddle River, N.J., 2003.
 85. O'Hare, G., *Weather, climate and climate change: human perspectives*, 1st ed,Pearson Prentice Hall, New York, 2005.
 86. Van Andel, T.H., *New views on an old planet: continental drift and the history of earth*, 1st ed,Cambridge University Press, Cambridge, 1985.
 87. National Aeronautics and Space Administration, <http://nssdc.gsfc.nasa.gov/planetary/factsheet/earthfact.html>, last accessed date: 27/11/ 2007
 88. National Aeronautics and Space Administration, <http://eosps0.gsfc.nasa.gov/>, last accessed date: 27/11/ 2007
 89. Burroughs, W., *Climate into the 21st Century*, 1st ed,the United Kingdom at the University Press, Cambridge, 2003.
 90. National Oceanic and Atmospheric Administration, <http://www.srh.noaa.gov/srh/jetstream/atmos/layers.htm#ion>, last accessed date: 15/12/2007
 91. Bradley, R.S., *Paleoclimatology: reconstructing climates of the quaternary*, 2nd ed, Academic Press, San Diego, CA, 1999.
 92. National Aeronautics and Space Administration,<http://asd-www.larc.nasa.gov/erbe/components2.gif>, last accessed date: 15/12/2007
 93. Climatic Research Unit, <http://www.cru.uea.ac.uk/cru/info/causecc/>, last accessed date: 23/12/ 2007
 94. Petit, J.R., "Climate and atmospheric history of the past 420,000 years from the Vostok ice core, Antarctica", *Nature*, Vol **399** pp. 429-436,1999.

95. Bell, B., "The oldest records of the Nile floods", *Geographical journal*, Vol **136** pp. 569-573,1970.
96. Henfling, E., and H. Pflaubaum, "Neue Aspekte zur klimatischen Interpretation der hohen pharaonischen Nilflutmarken am 2. Katarakt aus ägyptologischer und geomorphologischer Sicht", *Würzburger Geographische Arbeiten*, Vol **80** pp. 87-109,1991.
97. Essex, C., R. McKittrick, and B. Andresen, "Does a global temperature exist?" *Journal of Non-Equilibrium Thermodynamics*, Vol pp. 1-24,in press, 2006.
98. Freitas, C.R.D., "Are observed change in the concentration of carbon dioxide in the atmosphere really dangerous?" *Bulletin of Canadian Petroleum Geology*, Vol **50**(2) pp. 297-327,2002.
99. Lindzen, R.S., "Some coolness concerning global warming", *Bulletin of The American Meteorological Society*, Vol **71**(3) pp. 288-299,1990.
100. Khandekar, M.L., T.S. Murty, and P. Chittibabu, "The global warming debate: a review of the state of science", *Pure and Applied Geophysics*, Vol **162** pp. 1557-1586,2005.
101. Oke, T.R., "City size and the urban heat island", *Atmospheric Environment*, Vol **7** pp. 769-779,1973.
102. Robinson, A.B., S. L. Baliunas, W. Soon, and Z. W. Robinson, "Environmental effects of increased atmospheric carbon dioxide." Vol pp. 1998.
103. Raisanen, J., "How reliable are climate models? " *Tellus Series A-Dynamic Meteorology and Oceanography*, Vol **59A** pp. 2-29,2007.
104. CCSP, U.C.C.S.P., *Temperature Trends in the Lower Atmosphere: Steps for Understanding and Reconciling Differences.*,United States Climate Science Program and the Subcommittee on Global Change Research,Washington DC, USA. 164, 2006.
105. McIntyre, S., and R. McKittrick, "Corrections to Mann et al. (1998) Proxy Database and Northern Hemispheric Average Temperature Series", *Energy and Environment*, Vol **14** pp. 751-771,2003.
106. Mann, M., R. Bradley, and M. Hughes, "Global-scale temperature patterns and climate forcing over the past six centuries", *Nature*, Vol **392** pp. 779-787,1998.
107. Wahl, E.R., and C.M. Ammann, "Robustness of the Mann, Bradley, Hughes reconstruction of Northern Hemisphere surface temperatures: Examination of criticisms based on the nature and processing of proxy climate evidence", *Climate Change*, Vol pp. in press, 2007.
108. FriisChristensen, E., and H. Svensmark, "What do we really know about the sun - Climate connection? " *Advances in Space Research*, Vol **20**(4/5) pp. 913-921,1997.
109. Marsh, N., and H. Svensmark, "Solar influence on Earth's climate", *Space Science Reviews*, Vol **107** pp. 317-325,2003.

110. Soon, W., Baliunas, S., Posmentier, E.S., and Okeke, P., "Variations of solar coronal hole area and terrestrial lower tropospheric air temperature from 1979 to mid-1998: astronomical forcings of change in earth's climate?" *New Astronomy*, Vol **4** pp. 563-579,2000.
111. Stott, P.A., G.S. Jones, and J.F.B. Mitchell, "Do models underestimate the solar contribution to recent climate change?" *Journal of Climate*, Vol **16** pp. 4079-4093,2003.
112. Marsh, N., and H. Svensmark, "Cosmic rays, clouds, and climate", *Space Science Reviews*, Vol **94** pp. 215-230,2000.
113. Courtillot, V., Y. Gallet, J.-L. Le Mouél, F. Fluteau, and A. Genevey, "Are there connections between the Earth's magnetic field and climate?" *Earth and Planetary Science Letters*, Vol **253** pp. 328-339,2007.
114. Friis-Christensen, E., and H. Lassen, "Length of the solar cycle: an indicator of solar activity closely associated with climate", *Science*, Vol **254** pp. 698-700,1991.
115. Khilyuk, L.F., and G.V. Chilingar, "Global warming: are we confusing cause and effect?" *Energy Sources*, Vol **25** pp. 357-370,2003.
116. Laut, P., "Solar activity and terrestrial climate: an analysis some purported correlations", *Journal of Atmospheric and Solar-Terrestrial Physics*, Vol **65** pp. 801-812,2003.
117. De Jager, C., and I. Usoskin, "On possible drivers of sun-induced climate changes", *Journal of Atmospheric and Solar-terrestrial Physics*, Vol **68** pp. 2053-2060,2006.
118. Thejll, P., and K. Lassen, "Solar forcing of the Northern hemisphere land air temperature: new data ", *Journal of Atmospheric and Solar-Terrestrial Physics*, Vol **62** pp. 1207-1213,2000.
119. Mazzarella, A., "The 60-year solar modulation of global air temperature: the Earth's rotation and atmospheric circulation connection", *Theoretical and Applied Climatology*, Vol **88** pp. 193-199,2007.
120. Svensmark, H., and E. Friis-Christensen, "Variation of cosmic ray flux and global cloud coverage-a missing link in solar-climate relationships", *Journal of Atmospheric and Solar-Terrestrial Physics*, Vol **59**(11) pp. 1225-1232,1997.
121. Svensmark, H., "Influence of cosmic rays on Earth's climate", *Physical Review Letters*, Vol **81**(22) pp. 5027-5030,1998.
122. Kristjánsson, J.E., and J. Kristiansen, "Is there a cosmic ray signal in recent variations in global cloudiness and cloud radiative forcing?" *Journal of Geophysical Research*, Vol **105**(D9) pp. 11851-11863,2000.
123. Khilyuk, L.F., and G.V. Chilingar, "On global forces of nature driving the Earth's climate. Are Humans involved?" *Environmental Geology*, Vol **50** pp. 899-910,2006.

124. Yasamanov, N.A., "Modern global warming: causes and ecological consequences (in Russian)", *Bull Dubna Int Univ Nat Soc Man*, Vol **1**(8) pp. 12-21,2003.
125. Ramanathan, V., "The role of ocean-atmosphere interactions in the CO₂ climate problem ", *Journal of Atmospheric Science*, Vol **38** pp. 918-930,1981.
126. Ramanathan, V., and J.A. Coakley, "Climate modelling through radiative-convective models", *Reviews of Geophysics and Space Physics*, Vol **16**(4) pp. 465-489,1978.
127. Modest, M.F., "The Weighted-Sum-of-Gray-Gases Model for Arbitrary Solution Methods in Radiative Transfer", *ASME Journal of Heat Transfer*, Vol **113** pp. 650-656,1991.
128. Hottel, H.C., and A.F. Sarofim, *Radiative Transfer*, McGraw-Hill, New York, 1967.
129. Selçuk, N., and N. Kayakol. "Evaluation of Angular Quadrature and Spatial Differencing Schemes for Discrete Ordinates Method in Rectangular Furnaces", *Proc. of Proceedings of 31st National Heat Transfer Conference*, Houston, Texas, 325(3), ASME HDT, 1996.
130. Chai, J.C., H.S. Lee, and S.V. Patankar, "Ray Effect and False Scattering in the Discrete Ordinates Method", *Numerical Heat Transfer Part B-Fundamentals*, Vol **24** pp. 373-389,1993.
131. Carlson, B.G., and K.D. Lathrop, *Transport Theory-the Method of Discrete Ordinates*, *Computing Methods in Reactor Physics*, ed. H. Greenspan, C.N. Kelber, and D. Okrent, Gordon and Breach, New York, 1968.
132. Fiveland, W.A., "The Selection of Discrete Ordinate Quadrature Sets for Anisotropic Scattering", *Fundamentals of Radiation Heat Transfer*, Vol pp. 89-96,1991.
133. Wakil, N.E., and J.F. Sacadura, "Some Improvements of Discrete Ordinates Method for the Solution of the Radiative Transport Equation in Multi-Dimensional Anisotropically Scattering Media", *Developments in Radiative Heat Transfer*, Vol pp. 119-127,1992.
134. Schiesser, W.E., *The Numerical Method of Lines in Integration of Partial Differential Equations*, Academic Press Inc., San Diego, 1991.
135. Weiner, R., B.A. Schmitt, and H. Podhaisky, *Row-map-a row-code with krylov techniques for large stiff odes*, Tech. Rep. 39, FB Mathematik und Informatik, Universitaet Halle, 1996.
136. Radhakrishnan, K., and A.C. Hindmarsh, *Description and use of Isode, the livermore solver for ordinary differential equations*, Tech. Rep. UCRL-ID-113855, Lawrence Livermore National Laboratory, NASA, 1993.
137. Brown, P.N., G.D. Byrne, and A.C. Hindmarsh, "Vode: A variable coefficient ode solver", *SIAM J. Sci. Stat. Comput.*, Vol **10** pp. 1038-1051,1989.
138. Weiner, R., B.A. Schmitt, and H. Podhaisky, "Rowmap- a Row-Code with

- Krylov Techniques for Large Stiff Odes", *Applied Numerical Mathematics*, Vol **25**(2-3) pp. 303-319,1997.
139. Saucez, P., W.E. Schiesser, and A.V. Wouwer, "Upwinding in the Method of Lines", *Mathematics and Computers in Simulation*, Vol **56** pp. 171-185,2001.
 140. Denison, M.K., A Spectral Line-Based Weighted-Sum-of-Gray-Gases Model for Arbitrary RTE Solvers, Ph.D. Thesis, Brigham Young University, Provo, Utah, 1994.
 141. Taine, J., "A Line-by-Line Calculations of Low-Resolution Radiative Properties of CO₂-CO-Transparent Nonisothermal Gases Mixtures up to 3000 K", *Journal of Quantitative Spectroscopy and Radiative Transfer*, Vol **30** pp. 371-379,1983.
 142. Coelho, P.J., "Numerical Simulation of Radiative Heat Transfer from Non-Gray Gases in Three-Dimensional Enclosures", *Journal of Quantitative Spectroscopy and Radiative Transfer*, Vol **74** pp. 307-328,2001.
 143. Edwards, D.K., and A. Balakrishnan, "Thermal Radiation by Combustion Gases", *International Journal of Heat and Mass Transfer*, Vol **16** pp. 25-40,1973.
 144. Edwards, D.K., and W.A. Menard, "Comparison of models for correlation of total band absorption", *Applied Optics*, Vol **3**(621-626) pp. 1964.
 145. HITRAN, <http://cfa-www.harvard.edu/hitran/>, last accessed date: 15/07/2008
 146. Chang, S.L., and K.T. Rhee, "Blackbody Radiation Functions", *International Communications in Heat Mass Transfer*, Vol **11** pp. 451-455,1984.
 147. Mengüç, M.P., and R. Viskanta, "On the Radiative Properties of Polydispersions: A Simplified Approach", *Combustion Science and Technology*, Vol **44** pp. 143-159,1985.
 148. Rothman, L.S., D. Jacquemart, A. Barbe, D.C. Benner, M. Birk, L.R. Brown, M.R. Carleer, C. Chackerian, K. Chance, L.H. Coudert V., Dana, V.M. Devi, J.M. Flaud, R.R. Gamache, A. Goldman, J.M. Hartmann, K.W. Jucks, A.G. Maki, J.Y. Mandin, S.T. Massie, J. Orphal, A. Perrin, C.P. Rinsland, M.A.H. Smith, J. Tennyson, R.N. Tolchenov, R.A. Toth, J. Vander Auwera, P.Varanasi, G. Wagner, "The HITRAN 2004 molecular spectroscopic database ", *journal of Quantitative Spectroscopy & Radiative Transfer*, Vol **96** pp. 139-204,2005.
 149. National Oceanic and Atmospheric Administration, <http://www.esrl.noaa.gov/gmd/ccgg/trends/index.html#mlo>, last accessed date: 12/05/2008
 150. Edwards, D.K., "Molecular Gas Band Radiation", *Advances in Heat Transfer*, Vol **12** pp. 115-193,1976.
 151. Modest, M.F., *Radiative Heat Transfer*, Academic Press Inc, San Diego, 2003.
 152. Tarhan, T., Numerical Simulation of Laminar reacting flows, Ph.D. Thesis, Middle East Technical University, Turkey, 2004.

APPENDIX A

EXPONENTIAL WIDE BAND MODEL PARAMETERS

A.1 Calculation of Band Strength Parameter, α

The empirical correlation form which the band strength parameter, α , is calculated is given by Edwards [150] as follows:

$$\alpha(T) = \alpha_0 \frac{\psi^*(T)}{\psi^*(T_0)} = \alpha_0 \frac{\left\{ 1 - \exp\left(-\sum_{k=1}^m u_k \delta_k\right) \right\} \psi(T)}{\left\{ 1 - \exp\left(-\sum_{k=1}^m u_{0,k} \delta_k\right) \right\} \psi(T_0)} \quad (\text{A.1})$$

where

$$\psi(T) = \frac{\prod_{k=1}^m \sum_{v_k=v_{0,k}}^{\infty} \frac{(v_k + g_k + |\delta_k| - 1)!}{(g_k - 1)! v_k!} e^{-u_k v_k}}{\prod_{k=1}^m \sum_{v_k=0}^{\infty} \frac{(v_k + g_k - 1)!}{(g_k - 1)! v_k!} e^{-u_{0,k} v_k}} \quad (\text{A.2})$$

and

$$u_k = \frac{hc\eta_k}{kT}, \quad u_{0,k} = \frac{hc\eta_k}{kT_0} \quad (\text{A.3})$$

$$v_{0,k} = \begin{cases} 0 & \text{for } \delta_k \geq 0 \\ |\delta_k| & \text{for } \delta_k \leq 0 \end{cases} \quad (\text{A.4})$$

T_0 is the reference temperature and is taken as 100 K, h ($=6.6261 \times 10^{-34}$ J.s) is the Planck's constant, c ($=2.998 \times 10^8$ m/s) is the speed of light and k ($=1.3807 \times 10^{-23}$ J/K) is Boltzmann's constant. The summation over v_k were carried until 10 and 20

for H₂O and CO₂, respectively. Beyond these numbers the results remain unchanged. Values of EWBM correlation parameters m , band strength parameter at the reference condition, $\alpha_0 (= \alpha(T_0))$, the lowest possible initial state, $v_{0,k}$, change in vibrational quantum number, δ_k , vibrational quantum numbers, η_k , statistical weights (unity for non-degenerate vibrations, greater for degenerate ones), g_k are tabulated for longwave region of spectrum (10-3000 cm⁻¹) in Tables A.1 [151] for H₂O and CO₂. For calculation of $\psi(T_0)$, temperature T is simply set T_0 in Eq. (A.2).

Table A.1 Exponential wide band model correlation parameters for H₂O and CO₂

Band Location		Pressure Parameters		Correlation Parameters		
η_0 [cm ⁻¹]	δ_k	n	b	α_0 [cm ⁻¹ /(g/m ²)]	γ_0	ω_0 [cm ⁻¹]
H₂O						
$m=3, \eta_1=3652 \text{ cm}^{-1}, \eta_2=1595 \text{ cm}^{-1}, \eta_3=3756 \text{ cm}^{-1}, g_k = (1,1,1)$						
140 ^a	(0,0,0)	1	$8.6\sqrt{(T_0/T)} + 0.5$	5.455	0.143	69.3
1600	(0,1,0)	1	$8.6\sqrt{(T_0/T)} + 0.5$	41.2	0.094	56.4
CO₂						
$m=3, \eta_1=1351 \text{ cm}^{-1}, \eta_2=666 \text{ cm}^{-1}, \eta_3=2396 \text{ cm}^{-1}, g_k = (1,2,1)$						
667	(0,1,0)	0.7	1.3	19.0	0.062	12.7
960	(-1,0,1)	0.8	1.3	2.47×10^{-9}	0.040	13.4
1060	(-1,0,1)	0.8	1.3	2.47×10^{-9}	0.119	10.1
2410	(0,0,1)	0.8	1.3	110.0	0.247	11.2
^a For the rotational band $\alpha(T) = \alpha_0 \exp(-9\sqrt{T_0/T} - 1)$, $\gamma = \gamma_0 \sqrt{T_0/T}$						

A.2 Calculation of Line Overlap Parameter, β

The empirical correlation form which the line overlap parameter, β , is calculated is given by Edwards [150] as follows:

$$\beta(T) = \gamma P_e = \gamma_0 \sqrt{\frac{T_0}{T}} \frac{\Phi(T)}{\Phi(T_0)} P_e \quad (\text{A.5})$$

where

$$\Phi(T) = \frac{\left\{ \prod_{k=1}^m \sum_{v_k=v_{0,k}}^{\infty} \sqrt{\frac{(v_k + g_k + |\delta_k| - 1)!}{(g_k - 1)! v_k!}} e^{-u_k v_k} \right\}^2}{\prod_{k=1}^m \sum_{v_k=v_{0,k}}^{\infty} \frac{(v_k + g_k + |\delta_k| - 1)!}{(g_k - 1)! v_k!} e^{-u_k v_k}} \quad (\text{A.6})$$

and

$$P_e = \left[\frac{P}{P_0} \left(1 + (b-1) \frac{P_a}{P} \right) \right]^n \quad (\text{A.7})$$

P_e is the effective pressure. P_0 is the reference pressure and is taken as 1 atm and P_a is the partial pressure of the absorbing gas. The summation over v_k were carried until 10 and 20 for H₂O and CO₂, respectively. Beyond these numbers the results remain unchanged. Values of EWBM correlation parameters, pressure parameters n and b , line overlap parameter at the reference condition, $\gamma_0 (= \gamma(T_0))$, the lowest possible initial state, $v_{0,k}$, change in vibrational quantum number, δ_k , vibrational quantum numbers, η_k , statistical weights (unity for non-degenerate vibrations, greater for degenerate ones), g_k values are tabulated for longwave region of spectrum in Tables A.1 [151] for CO₂ and H₂O. For calculation of $\Phi(T_0)$, temperature T is simply set T_0 in Eq. (A.6)

A.3 Calculation of Band Width Parameter, ω :

The empirical correlation form which band width parameter, ω , is calculated is given by Edwards [150] as follows:

$$\omega(T) = \omega_0 \sqrt{\frac{T}{T_0}} \quad (\text{A.8})$$

where ω_0 is band width parameter at the reference condition listed in Tables A.1 [151] for CO₂ and H₂O.

APPENDIX B

INITIAL PARAMETERS FOR THE ODE SOLVER (ROWMAP) SUBROUTINE

The radiation and radiative-convective codes used in this study require specifications of certain input parameters for the ODE solver subroutine in addition to the input data relevant with the physical system and subdivisions of angular and spatial domains which are presented in the text. Initial parameters for the ODE solver are the absolute and relative error tolerances (ABSERR and RELERR), time interval for printing (TP) and convergence criteria for terminating the integration. Execution of the radiative-convective code is sensitive to TP value. Unless it is correctly selected, the program does not run. Therefore, its value should be found by trial-and-error according to the selected final time. Different print intervals were examined to obtain the required final times. Table B.1 summarized the results of this examination. In this study, the code was run up to ~ 144000 sec (40 hours). Tables B.2 presents the input parameters utilized to obtain solutions for the radiation and radiative convective codes.

Table B.1 Final time values for different print intervals

Print interval (sec)	Final time(sec)
300	16500
600	148800
720	5040
1200	56400

Table B.2 Initial parameters utilized for ROWMAP subroutine for radiation and radiative-convective codes

Code	ABSERR	RELERR	TP	€
Radiation	0.001	0.001	10	0.001
Radiative-convective	0.001	0.001	600	0.001

APPENDIX C

POINT VALUES OF ALL PREDICTED QUANTITIES BY MOL OF SOLUTION DOM AND LBLRTM

Flux predictions of the MOL solution of DOM with WBCK and LBLRTM for all spatial subdivision and their absolute percentage errors are given in Tables C.1-C.8

Table C.1 Flux predictions (in W/m²) of the present study and LBLRTM for different number of grids with uniform spacing

Altitude (km)	LBLRTM			6 grids			11 grids			21 grids			41 grids			81 grids		
	Up	Down	Net	Up	Down	Net	Up	Down	Net	Up	Down	Net	Up	Down	Net	Up	Down	Net
10.0	310.7	0.0	310.7	270.3	0.0	270.3	262.2	0.0	262.2	258.1	0.0	258.1	256.0	0.0	256.0	255.0	0.0	255.0
9.5	313.5	42.2	271.3							263.1	43.7	219.4	260.9	47.8	213.1	259.9	48.7	211.2
9.0	316.5	56.0	260.5				273.2	55.2	218.0	268.6	61.3	207.2	266.3	62.8	203.5	265.2	63.5	201.7
8.5	319.9	67.2	252.7							274.5	73.4	201.1	272.2	75.0	197.2	271.0	76.0	195.0
8.0	323.6	77.9	245.7	296.6	70.4	226.2	286.2	80.7	205.5	280.9	84.7	196.2	278.4	86.7	191.7	277.2	87.9	189.3
7.5	327.7	88.6	239.1							287.9	96.3	191.6	285.3	98.7	186.6	284.0	100.0	184.0
7.0	332.2	99.7	232.5				301.3	103.2	198.1	295.4	108.3	187.1	292.6	111.0	181.6	291.3	112.5	178.8
6.5	337.0	111.2	225.8							303.4	121.0	182.5	300.6	123.9	176.6	299.2	125.5	173.7
6.0	342.2	123.2	219.0	330.3	116.6	213.8	318.2	127.9	190.2	311.8	134.2	177.6	308.8	137.3	171.5	307.4	139.0	168.4
5.5	347.5	135.6	211.9							320.6	147.8	172.7	317.5	151.1	166.3	316.0	152.8	163.1
5.0	353.2	148.5	204.7				336.8	155.0	181.8	329.9	161.9	168.1	326.6	165.3	161.3	325.0	167.1	157.9
4.5	359.3	162.3	197.0							339.9	176.7	163.3	336.5	180.4	156.1	334.8	182.3	152.5
4.0	365.9	177.3	188.6	370.7	170.8	200.0	357.6	184.6	173.0	350.6	192.3	158.3	347.0	196.2	150.8	345.3	198.2	147.0
3.5	373.0	193.0	180.0							361.6	208.5	153.0	358.1	212.7	145.5	356.4	214.7	141.7
3.0	380.6	209.2	171.4				379.1	216.8	162.3	372.4	225.1	147.3	368.9	229.2	139.7	367.2	231.3	135.9
2.5	388.6	226.0	162.6							383.2	241.2	142.0	379.7	245.1	134.6	378.0	247.0	131.0
2.0	396.8	243.3	153.5	409.6	234.6	175.0	399.0	248.8	150.3	393.3	256.5	136.8	390.3	260.1	130.2	388.8	261.9	126.8
1.5	403.7	258.9	144.8							402.7	270.7	131.9	399.7	273.9	125.8	398.2	275.5	122.7
1.0	410.7	273.9	136.8				417.5	278.0	139.6	412.1	284.3	127.8	409.2	287.6	121.6	407.7	289.3	118.4
0.5	417.8	288.8	129.0							421.3	298.8	122.5	418.6	302.4	116.2	417.2	304.3	112.9
0.0	424.7	303.8	120.9	424.7	294.6	130.1	424.7	307.2	117.5	424.7	314.5	110.3	424.7	318.4	106.3	424.7	320.5	104.3

Table C.2 Absolute % relative errors of the present study for different number of grids with uniform spacing

Absolute relative % error															
Altitude (km)	6 grids			11 grids			21 grids			41 grids			81 grids		
	Up	Down	Net	Up	Down	Net	Up	Down	Net	Up	Down	Net	Up	Down	Net
10.0	13.0	0.0	13.0	15.6	0.0	15.6	16.9	0.0	16.9	17.6	0.0	17.6	17.9	0.0	17.9
9.5							16.1	3.5	19.1	16.8	13.3	21.5	17.1	15.3	22.1
9.0				13.7	1.4	16.3	15.2	9.6	20.5	15.9	12.1	21.9	16.2	13.4	22.6
8.5							14.2	9.3	20.4	14.9	11.5	22.0	15.3	13.1	22.8
8.0	8.3	9.7	7.9	11.6	3.6	16.4	13.2	8.7	20.1	14.0	11.3	22.0	14.3	12.9	22.9
7.5							12.1	8.7	19.9	12.9	11.4	22.0	13.3	12.9	23.1
7.0				9.3	3.5	14.8	11.1	8.7	19.5	11.9	11.4	21.9	12.3	12.8	23.1
6.5							10.0	8.8	19.2	10.8	11.4	21.8	11.2	12.8	23.1
6.0	3.5	5.4	2.4	7.0	3.8	13.1	8.9	8.9	18.9	9.8	11.5	21.7	10.2	12.8	23.1
5.5							7.8	9.0	18.5	8.6	11.5	21.5	9.1	12.7	23.0
5.0				4.6	4.4	11.2	6.6	9.0	17.9	7.5	11.3	21.2	8.0	12.5	22.9
4.5							5.4	8.9	17.1	6.4	11.1	20.8	6.8	12.3	22.6
4.0	1.3	3.7	6.0	2.3	4.1	8.3	4.2	8.5	16.1	5.2	10.7	20.0	5.6	11.8	22.0
3.5							3.1	8.1	15.0	4.0	10.2	19.2	4.4	11.3	21.3
3.0				0.4	3.6	5.3	2.2	7.6	14.1	3.1	9.6	18.5	3.5	10.6	20.7
2.5							1.4	6.7	12.7	2.3	8.5	17.2	2.7	9.3	19.5
2.0	3.2	3.6	14.0	0.6	2.3	2.1	0.9	5.4	10.9	1.6	6.9	15.2	2.0	7.7	17.4
1.5							0.3	4.6	8.9	1.0	5.8	13.1	1.4	6.4	15.3
1.0				1.7	1.5	2.0	0.3	3.8	6.6	0.4	5.0	11.1	0.7	5.6	13.5
0.5							0.8	3.5	5.0	0.2	4.7	9.9	0.1	5.4	12.5
0.0	0.0	3.0	7.6	0.0	1.1	2.8	0.0	3.5	8.8	0.0	4.8	12.1	0.0	5.5	13.8

$$\text{Absolute \% relative error} = (|\text{predicted-LBLRTM}| / \text{LBLRTM}) \times 100$$

Table C.3 Flux predictions (in W/m^2) of the present study and LBLRTM for different number of non-uniform grids

Altitude (km)	LBLRTM			12 grids			8 grids			7 grids		
	Up	Down	Net	Up	Down	Net	Up	Down	Net	Up	Down	Net
10.0	310.7	0.0	310.7	258.8	0.0	258.8	267.4	0.0	267.4	266.3	0.0	266.3
8.0	323.6	77.9	245.7	287.0	70.4	216.6	293.6	70.4	223.3			
7.0	332.2	99.7	232.5							313.2	81.9	231.3
6.0	342.2	123.2	219.0	322.5	116.6	205.9	326.3	116.6	209.8			
4.0	365.9	177.3	188.6	350.6	170.8	179.8	357.6	170.8	186.8	357.6	156.9	200.7
3.5	373.0	193.0	180.0	361.6	202.1	159.5						
3.0	380.6	209.2	171.4	372.4	221.9	150.5	379.1	214.4	164.7	379.1	211.1	168.0
2.5	388.6	226.0	162.6	383.2	239.2	144.0						
2.0	396.8	243.3	153.5	393.3	255.2	138.1	399.0	247.6	151.4	399.0	246.3	152.8
1.5	403.7	258.9	144.8	402.7	269.8	132.9						
1.0	410.7	273.9	136.8	412.1	283.6	128.5	417.5	276.9	140.6	417.5	276.1	141.4
0.5	417.8	288.8	129.0	421.3	298.2	123.1						
0.0	424.7	303.8	120.9	424.7	314.0	110.8	424.7	306.3	118.5	424.7	305.7	119.0

Table C.4 Absolute % relative errors of the present study for different number of non-uniform grids

Absolute % relative error									
Altitude (km)	12 grids			8 grids			7 grids		
	Up	Down	Net	Up	Down	Net	Up	Down	Net
10.0	16.7	0.0	16.7	13.9	0.0	13.9	14.3	0.0	14.3
8.0	11.3	9.7	11.8	9.3	9.7	9.1			
7.0							5.7	17.9	0.5
6.0	5.8	5.4	6.0	4.6	5.4	4.2			
4.0	4.2	3.7	4.6	2.3	3.7	1.0	2.3	11.5	6.4
3.5	3.1	4.7	11.4						
3.0	2.2	6.0	12.2	0.4	2.5	3.9	0.4	0.9	2.0
2.5	1.4	5.8	11.4						
2.0	0.9	4.9	10.0	0.6	1.8	1.4	0.6	1.2	0.5
1.5	0.3	4.2	8.2						
1.0	0.3	3.5	6.1	1.7	1.1	2.8	1.7	0.8	3.4
0.5	0.8	3.3	4.6						
0.0	0.0	3.4	8.4	0.0	0.8	2.0	0.0	0.6	1.5

$$\text{Absolute \% relative error} = (|\text{predicted-LBLRTM}| / \text{LBLRTM}) \times 100$$

Table C.5 Flux predictions of the present study and LBLRTM with absolute percentage error for az = 0.25

Altitude (km)	LBLRTM			7 grids with az = 0.25					
	Fluxes			Fluxes			Absolute % relative error		
	Up	Down	Net	Up	Down	Net	Up	Down	Net
10.00	310.7	0.0	310.7	273.6	0.0	273.6	11.9	0.0	11.9
7.78	333.3	101.2	232.1	312.4	89.6	222.8	6.3	11.4	4.0
5.78	360.6	166.5	194.1	354.8	157.4	197.4	1.6	5.4	1.7
4.00	387.0	224.3	162.6	390.0	222.5	167.4	0.8	0.8	2.9
2.44	408.5	269.4	139.0	411.9	272.1	139.7	0.8	1.0	0.5
1.11	422.5	298.0	124.5	422.8	302.8	120.1	0.1	1.6	3.5
0.00	424.7	303.8	120.9	424.7	316.9	107.8	0.0	4.3	10.8

Table C.6 Flux predictions of the present study and LBLRTM with absolute percentage error for $az = 0.4$

Altitude (km)	LBLRTM			7 grids with $az = 0.4$					
	Fluxes			Fluxes			Absolute % relative error		
	Up	Down	Net	Up	Down	Net	Up	Down	Net
10.00	310.7	0.0	310.7	270.3	0.0	270.3	13.0	0.0	13.0
7.78	325.8	81.3	244.5	297.2	76.0	221.2	8.8	6.5	9.5
5.78	345.1	130.0	215.2	328.6	126.3	202.3	4.8	2.8	6.0
4.00	366.2	178.7	187.5	362.5	177.8	184.8	1.0	0.5	1.5
2.44	387.8	225.6	162.1	392.6	229.5	163.1	1.2	1.7	0.6
1.11	408.5	269.0	139.5	416.1	273.1	143.0	1.9	1.5	2.6
0.00	424.7	303.8	120.9	424.7	309.0	115.7	0.0	1.7	4.3

Table C.7 Flux predictions of the present study and LBLRTM with absolute percentage error for $az = 0.45$

Altitude (km)	LBLRTM			7 grids with $az = 0.45$					
	Fluxes			Fluxes			Absolute % relative error		
	Up	Down	Net	Up	Down	Net	Up	Down	Net
10.00	310.7	0.0	310.7	269.6	0.0	269.6	13.2	0.0	13.2
8.06	323.5	75.0	248.5	292.7	71.3	221.4	9.5	5.0	10.9
6.22	340.4	118.6	221.9	321.0	116.5	204.6	5.7	1.8	7.8
4.50	359.9	164.5	195.4	352.9	163.9	189.0	2.0	0.4	3.3
2.89	381.3	211.8	169.5	385.8	214.5	171.3	1.2	1.2	1.1
1.39	404.0	259.7	144.3	413.8	263.0	150.8	2.4	1.3	4.6
0.00	424.7	303.8	120.9	424.7	306.2	118.5	0.0	0.8	2.0

Table C.8 Flux predictions of the present study and LBLRTM with absolute percentage error for $az = 0.5$

Altitude (km)	LBLRTM			7 grids with $az = 0.5$					
	Fluxes			Fluxes			Absolute % relative error		
	Up	Down	Net	Up	Down	Net	Up	Down	Net
10.00	310.7	0.0	310.7	268.9	0.0	268.9	13.5	0.0	13.5
8.33	321.3	68.9	252.4	288.5	66.6	221.9	10.2	3.4	12.1
6.67	336.0	107.5	228.4	313.7	106.9	206.8	6.6	0.6	9.5
5.00	353.9	150.7	203.3	343.8	150.5	193.4	2.8	0.1	4.9
3.33	375.1	198.3	176.8	378.9	199.9	179.1	1.0	0.8	1.3
1.67	399.6	250.6	149.0	411.6	252.7	159.0	3.0	0.8	6.7
0.00	424.7	303.8	120.9	424.7	303.3	121.5	0.0	0.2	0.5

APPENDIX D

GRID GENERATION

The following formula is used to generate the grids in two-dimensional geometry (r- and z- direction) [152]

$$\begin{aligned} r(\xi, \eta) &= \sum_{i=1}^8 N_i(\xi, \eta) r_i \\ z(\xi, \eta) &= \sum_{j=1}^8 N_j(\xi, \eta) z_j \end{aligned} \quad (\text{D.1})$$

where

$$\begin{aligned} r_1 &= R & r_5 &= R \cdot ar \\ r_2 &= R & r_6 &= 0 \\ r_3 &= R & r_7 &= 0 \\ r_4 &= R \cdot ar & r_8 &= 0 \end{aligned} \quad (\text{D.2})$$

R is the thickness of the system in r-direction and ar which ranges from 0 to 1 is the grid size weight in r-direction. The schematic representation of 8 points can be seen in Figure D.1. And z_j in z-direction is represented as

$$\begin{aligned} z_1 &= 0 & z_5 &= L \\ z_2 &= L \cdot az & z_6 &= 0 \\ z_3 &= L & z_7 &= L \cdot az \\ z_4 &= 0 & z_8 &= L \end{aligned} \quad (\text{D.3})$$

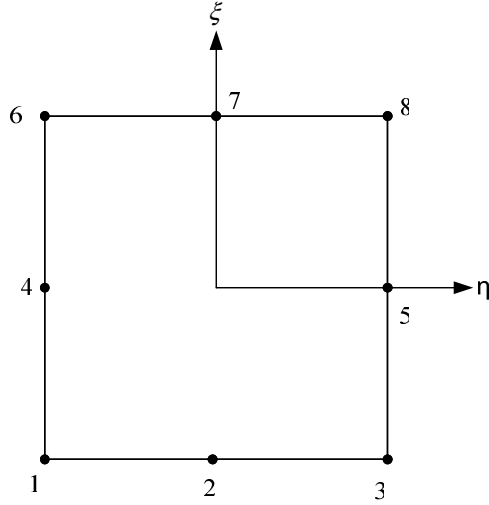


Figure D.1 Schematic representation of 8 points

L is the length of the system and az , range from 0 to 1, is the grid weights in z -direction. The different grid size was obtained by using different az for the same length of the system. N_i ($i=1,\dots,8$) is defined as

$$\begin{aligned}
 N_1 &= -\frac{1}{4}(\xi-1)(\eta-1)(\xi+\eta-1) \\
 N_2 &= \frac{1}{2}(\xi-1)(\eta-1)(\eta+1) \\
 N_3 &= \frac{1}{4}(\xi-1)(\eta+1)(\xi-\eta+1) \\
 N_4 &= \frac{1}{2}(\xi-1)(\eta-1)(\xi+1) \\
 N_5 &= -\frac{1}{2}(\xi-1)(\eta+1)(\xi+1) \\
 N_6 &= -\frac{1}{4}(\xi+1)(\eta-1)(\xi-\eta-1) \\
 N_7 &= -\frac{1}{2}(\xi+1)(\eta-1)(\eta+1) \\
 N_8 &= \frac{1}{4}(\xi+1)(\eta+1)(\xi-\eta-1)
 \end{aligned} \tag{D.4}$$

Suppose that number of grid points in the ξ -direction is N_ξ that in the η -direction is N_η . To reduce two-dimensional grid generation to one-dimensional N_ξ is taken as 2 and then

$$\text{at } i=1 \quad \xi = -1 \quad \text{and} \quad \text{at } i=N_\xi \quad \xi = 1 \quad (\text{D.5})$$

where ξ should obey the flowing function

$$\xi = ai + b \quad (\text{D.4})$$

applying Eq. (D.5) on the Eq. (D.6) to evaluate ξ in Eq (D.4)

$$\xi = \left(\frac{2}{N_\xi - 1} \right) i + \left(1 - \frac{2}{N_\xi - 1} N_\xi \right) \quad (\text{D.7})$$

where i represents the grid points in ξ -direction, $i=1,2$. For $N_\xi = 2$, Eq. (D.7) takes following form

$$\xi = 2i - 1 \quad (\text{D.8})$$

Similarly for the η -direction,

$$\eta = \left(\frac{2}{N_\eta - 1} \right) j + \left(1 - \frac{2}{N_\eta - 1} N_\eta \right) \quad (\text{D.9})$$

where j represents the grid points in η -direction, $j=1, \dots, N_\eta$

APPENDIX E

POINT VALUES OF PREDICTED TEMPERATURE PROFILES

Temperature predictions during 40 hours period at the surface, at 4 km above the surface and at the top of the atmosphere are given in Tables E.1-E.3, respectively.

Table E.1 Temperature predictions during 40 hours period at the surface for different coupling interval and simultaneous solution

Time(h)	Simultaneous	2 h	10 h	Time(h)	Simultaneous	2 h	10 h
0.0	294.200	294.200	294.200	20.5	294.409	294.412	294.413
0.5	294.205	294.205	294.205	22.0	294.424	294.428	294.428
1.0	294.210	294.210	294.210	22.5	294.429	294.433	294.433
1.5	294.216	294.215	294.215	23.0	294.434	294.438	294.439
2.0	294.221	294.221	294.221	23.5	294.439	294.443	294.444
2.5	294.226	294.226	294.226	24.0	294.444	294.448	294.449
3.0	294.231	294.231	294.231	24.5	294.449	294.453	294.454
3.5	294.236	294.236	294.236	25.0	294.454	294.458	294.459
4.0	294.242	294.241	294.242	25.5	294.459	294.464	294.464
4.5	294.247	294.247	294.247	26.0	294.464	294.469	294.470
5.0	294.252	294.252	294.252	26.5	294.469	294.474	294.475
5.5	294.257	294.257	294.257	27.0	294.474	294.479	294.480
6.0	294.262	294.262	294.262	27.5	294.479	294.484	294.485
6.5	294.267	294.267	294.268	28.0	294.484	294.489	294.490
7.0	294.273	294.273	294.273	28.5	294.489	294.494	294.496
7.5	294.278	294.278	294.278	29.0	294.494	294.500	294.501
8.0	294.283	294.283	294.283	29.5	294.499	294.505	294.506
8.5	294.288	294.288	294.289	30.0	294.504	294.510	294.511
9.0	294.293	294.293	294.294	30.5	294.509	294.515	294.516
9.5	294.298	294.299	294.299	31.0	294.514	294.520	294.521
10.0	294.304	294.304	294.304	31.5	294.519	294.525	294.526
10.5	294.309	294.309	294.309	32.0	294.524	294.530	294.532
11.0	294.313	294.314	294.315	32.5	294.529	294.535	294.537
11.5	294.318	294.319	294.320	33.0	294.534	294.541	294.542
12.0	294.324	294.325	294.325	33.5	294.538	294.546	294.547
12.5	294.329	294.330	294.330	34.0	294.543	294.551	294.552
13.0	294.334	294.335	294.335	34.5	294.548	294.556	294.557
13.5	294.338	294.340	294.340	35.0	294.553	294.561	294.562
14.0	294.344	294.345	294.346	35.5	294.558	294.566	294.567
14.5	294.349	294.350	294.351	36.0	294.563	294.571	294.572
15.0	294.354	294.355	294.356	36.5	294.568	294.576	294.577
15.5	294.359	294.361	294.361	37.0	294.573	294.581	294.582
16.0	294.364	294.366	294.366	37.5	294.578	294.587	294.588
16.5	294.369	294.371	294.371	38.0	294.583	294.592	294.593
17.0	294.374	294.376	294.377	38.5	294.588	294.597	294.598
17.5	294.379	294.381	294.382	39.0	294.592	294.602	294.603
18.0	294.384	294.387	294.387	39.5	294.598	294.607	294.608
18.5	294.389	294.392	294.392	40.0	294.602	294.612	294.613
19.0	294.395	294.397	294.397				
19.5	294.399	294.402	294.402				
20.0	294.404	294.407	294.407				

Table E.2 Temperature predictions during 40 hours period at 4 km above the surface for different coupling interval and simultaneous solution

Time(h)	Simultaneous	2 h	10 h	Time(h)	Simultaneous	2 h	10 h
0.0	277.962	277.962	277.962	20.5	274.159	274.162	274.136
0.5	277.881	277.884	277.884	21.0	274.071	274.073	274.044
1.0	277.782	277.787	277.787	21.5	273.983	273.985	273.951
1.5	277.685	277.690	277.690	22.0	273.895	273.897	273.859
2.0	277.589	277.593	277.593	22.5	273.808	273.810	273.767
2.5	277.493	277.497	277.496	23.0	273.721	273.723	273.675
3.0	277.398	277.402	277.400	23.5	273.634	273.636	273.583
3.5	277.303	277.306	277.303	24.0	273.548	273.549	273.491
4.0	277.207	277.210	277.206	24.5	273.461	273.464	273.399
4.5	277.112	277.115	277.110	25.0	273.375	273.379	273.307
5.0	277.017	277.020	277.013	25.5	273.290	273.293	273.215
5.5	276.923	276.925	276.917	26.0	273.204	273.208	273.123
6.0	276.828	276.831	276.820	26.5	273.119	273.124	273.031
6.5	276.733	276.737	276.724	27.0	273.035	273.040	272.939
7.0	276.638	276.643	276.628	27.5	272.951	272.956	272.847
7.5	276.544	276.549	276.532	28.0	272.867	272.871	272.756
8.0	276.449	276.455	276.436	28.5	272.783	272.787	272.664
8.5	276.355	276.361	276.340	29.0	272.700	272.703	272.572
9.0	276.261	276.267	276.244	29.5	272.617	272.619	272.481
9.5	276.167	276.174	276.148	30.0	272.534	272.535	272.389
10.0	276.074	276.080	276.052	30.5	272.452	272.452	272.308
10.5	275.980	275.987	275.960	31.0	272.370	272.370	272.226
11.0	275.887	275.894	275.869	31.5	272.288	272.287	272.144
11.5	275.793	275.800	275.777	32.0	272.207	272.204	272.063
12.0	275.700	275.707	275.686	32.5	272.125	272.123	271.981
12.5	275.608	275.615	275.594	33.0	272.044	272.042	271.899
13.0	275.515	275.523	275.503	33.5	271.964	271.960	271.818
13.5	275.423	275.430	275.411	34.0	271.884	271.879	271.736
14.0	275.330	275.338	275.320	34.5	271.804	271.799	271.655
14.5	275.238	275.246	275.229	35.0	271.724	271.718	271.574
15.0	275.147	275.154	275.138	35.5	271.645	271.638	271.492
15.5	275.055	275.062	275.046	36.0	271.566	271.558	271.411
16.0	274.964	274.970	274.955	36.5	271.487	271.479	271.330
16.5	274.873	274.880	274.864	37.0	271.408	271.401	271.248
17.0	274.783	274.790	274.773	37.5	271.330	271.322	271.167
17.5	274.693	274.700	274.682	38.0	271.252	271.244	271.086
18.0	274.603	274.610	274.591	38.5	271.175	271.166	271.005
18.5	274.514	274.520	274.501	39.0	271.098	271.088	270.924
19.0	274.425	274.430	274.410	39.5	271.021	271.011	270.843
19.5	274.336	274.340	274.319	40.0	270.944	270.933	270.762
20.0	274.247	274.250	274.229				

Table E.3 Temperature predictions during 40 hours period at the top of the atmosphere for different coupling interval and simultaneous solution

Time(h)	Simultaneous	2 h	10 h	Time(h)	Simultaneous	2 h	10 h
0.0	242.704	242.704	242.704	20.5	236.690	236.749	236.481
0.5	242.565	242.566	242.566	21.0	236.564	236.622	236.357
1.0	242.396	242.400	242.400	21.5	236.437	236.496	236.232
1.5	242.228	242.234	242.234	22.0	236.312	236.370	236.108
2.0	242.061	242.068	242.068	22.5	236.187	236.247	235.984
2.5	241.894	241.906	241.902	23.0	236.064	236.123	235.860
3.0	241.729	241.744	241.736	23.5	235.941	236.000	235.736
3.5	241.566	241.583	241.571	24.0	235.819	235.876	235.612
4.0	241.403	241.421	241.405	24.5	235.697	235.755	235.488
4.5	241.242	241.264	241.240	25.0	235.576	235.634	235.364
5.0	241.082	241.107	241.075	25.5	235.456	235.513	235.240
5.5	240.924	240.951	240.909	26.0	235.337	235.392	235.116
6.0	240.767	240.794	240.744	26.5	235.217	235.273	234.993
6.5	240.611	240.641	240.579	27.0	235.099	235.155	234.869
7.0	240.457	240.489	240.415	27.5	234.982	235.037	234.746
7.5	240.304	240.336	240.250	28.0	234.865	234.919	234.622
8.0	240.152	240.184	240.085	28.5	234.749	234.804	234.499
8.5	240.001	240.036	239.921	29.0	234.633	234.690	234.375
9.0	239.851	239.889	239.756	29.5	234.518	234.575	234.252
9.5	239.703	239.741	239.592	30.0	234.403	234.461	234.129
10.0	239.555	239.594	239.428	30.5	234.289	234.348	234.018
10.5	239.409	239.450	239.286	31.0	234.175	234.236	233.908
11.0	239.264	239.306	239.144	31.5	234.062	234.124	233.797
11.5	239.120	239.163	239.003	32.0	233.951	234.011	233.687
12.0	238.977	239.020	238.861	32.5	233.839	233.901	233.576
12.5	238.835	238.880	238.719	33.0	233.728	233.791	233.466
13.0	238.694	238.740	238.578	33.5	233.617	233.680	233.356
13.5	238.555	238.600	238.436	34.0	233.508	233.570	233.245
14.0	238.416	238.461	238.295	34.5	233.398	233.462	233.135
14.5	238.278	238.326	238.154	35.0	233.290	233.355	233.025
15.0	238.142	238.190	238.013	35.5	233.182	233.247	232.915
15.5	238.006	238.055	237.872	36.0	233.075	233.139	232.805
16.0	237.871	237.920	237.731	36.5	232.967	233.033	232.695
16.5	237.736	237.787	237.590	37.0	232.861	232.926	232.585
17.0	237.603	237.654	237.449	37.5	232.755	232.820	232.475
17.5	237.470	237.521	237.308	38.0	232.649	232.714	232.365
18.0	237.338	237.388	237.167	38.5	232.543	232.610	232.255
18.5	237.206	237.259	237.027	39.0	232.438	232.506	232.146
19.0	237.076	237.131	236.886	39.5	232.334	232.402	232.036
19.5	236.947	237.003	236.746	40.0	232.230	232.298	231.926
20.0	236.818	236.875	236.606				